

ABSTRACT

NEWELL, ANDREW PHIFER. Microstructure Studies of Ti-6Al-4V Near-Net Shape Structural Components as Prepared by the Arcam Electron Beam Melting Process. (Under the direction of J. Michael Rigsbee).

The Arcam electron beam melting (EBM) process is used for rapid prototyping of fully functional metallic parts. Arcam uses electron beam scanning technology similar to a scanning electron microscope to form near-net shape components by selectively melting consecutive finite layers of alloy powder according a 3-D computer-aided design (CAD) file. The Arcam EBM process is being considered as a technology that can produce out-of-production Ti-6Al-4V alloy components for aging aircraft.

Two Arcam EBM machines are currently in use at NC state university; the Arcam S12 and the Arcam A2. The microstructures of three samples from preliminary production runs were characterized by optical, scanning electron (SEM), transmission electron (TEM), and scanning transmission electron microscopy (STEM). The microstructures of this limited sample set of as-built solid objects generally consisted of Widmanstätten morphologies of fine acicular alpha laths with retained beta between the alpha phase. Prior beta grain size and volume fraction of retained beta were determined by quantitative metallography. Porosity was found in all samples from both machines due to non-optimization of the processing parameters.

Microstructure Studies of Near-Net Shape Structural Components from Ti-6Al-4V as
Prepared by the Arcam Electron Beam Melting Process

by
Andrew Phifer Newell

A thesis submitted to the Graduate Faculty of
North Carolina State University
In partial fulfillment of the
Requirements for the degree of
Master of Science

Materials Science and Engineering

Raleigh, North Carolina

2009

APPROVED BY:

J. Michael Rigsbee
Committee Chair

Jerome J. Cuomo
Co-chair

John M. Mackenzie

DEDICATION

This thesis is dedicated to the inspiration and memory of Dr. Thomas Michael Hare and my grandfather, Otto Hehn.

BIOGRAPHY

Originally from Annapolis, Maryland, Andrew Phifer Newell proudly claims Charlotte, North Carolina as his home. He received his B.S. in Materials Science and Engineering at North Carolina State University in 2000 and returned to pursue his M.S. degree in Materials Science and Engineering under the direction of Dr. J.M. Rigsbee with a heavy concentration in electron microscopy. Andrew is an active member of the Society of Plastics Engineers (SPE) and the Materials Information Society (ASM International).

ACKNOWLEDGMENTS

I would like to graciously thank Dr. J. M. Rigsbee for his patience and guidance throughout the process of this research and for allowing me to serve in many active roles within the North Carolina State University Department of Materials Science and Engineering. I would also like to thank Dr. Jerome J. Cuomo and Dr. Roger C. Sanwald of the Institute for Maintenance Science and Technology at NC State and the Golden Leaf Foundation for funding this project. I am grateful to Dr. John M. Mackenzie for sharing his expertise in electron microscopy, digital imaging, and for serving on my committee. I would like to thank Dr. Denis R. Cormier of the Department of Industrial Engineering at NC State University and Brian Boyette of NAVAIR for supplying research materials.

Additionally I would like to thank all of those at North Carolina State University who have assisted me with sample preparation and electron microscope operation, which includes Dr. Tom Rawdanowicz and Maria L. Fiedler of the Department of Materials Science and Engineering, Chuck Mooney, Roberto Garcia, Ka C. “Wingo” Wong, and Dale Batchelor of the Analytical Instrumentation Facility, and Valerie Knowlton of the Center for Electron Microscopy in the Department of Microbiology. Other contributions that I am grateful for have come from Danny Brinkley of Progress Energy, John Mastovich, Roger Russell, and Edna Deas.

I am forever grateful to my mother for inspiring and encouraging me to seek higher education, my brother and my father for instilling a strong work ethic and providing guidance, and of course, Xandi, for her unyielding encouragement, love and support during this daunting task.

TABLE OF CONTENTS

LIST OF TABLES	vii
LIST OF FIGURES	viii
1. STATEMENT OF PROBLEM.....	1
2. INTRODUCTION	4
2.1. The Arcam Electron Beam Melting (EBM) Process	4
2.2. The Arcam EBM Process Apparatus	7
2.3. Precursor Material (Pre-Alloyed Powder)	9
2.4. Component Fabrication Process	12
2.5. Electron Beam-Powder Bed Interaction	14
2.6. Physical Metallurgy of Ti-6Al-4V Alloy.....	17
2.7. Microstructure of Ti-6Al-4V Arcam-Fabricated Parts	18
2.8. Surface Morphology of Beam-Melted Metal.....	19
3. EXPERIMENTAL PROCEDURE	21
3.1. Sample Geometry and Growth Orientation	21
3.2. Sample Preparation for Microstructure Analyses	28
3.2.1. Optical Microscopy.....	28
3.2.2. Scanning Electron Microscopy	28
3.2.3. Transmission Electron Microscopy	29
3.2.3.1. Electropolishing	29
3.2.3.2. Focused Ion Beam.....	31
3.3. Optical Microscopy.....	32
3.4 Scanning Electron Microscopy	32
3.5. Scanning Transmission Electron Microscopy	33
3.6. Transmission Electron Microscopy	34
3.7. Energy Dispersive X-Ray Spectroscopy.....	35
3.8. Grain Size Determination	36
3.9. Volume Fraction Determination	36
4. RESULTS AND DISCUSSION	38
4.1. Exterior Morphology of Arcam - Produced Components.....	39
4.1.1. Arcam S12 XY Component.....	39
4.1.2. Arcam S12 XZ Component	41
4.1.3. Arcam A2 Horizontal Cylinder Component.....	44
4.2. Microstructure of a Forged Turbine Blade	47
4.2.1. Grain Size and Morphology.....	47
4.2.2. Description of $\alpha + \beta$ phase morphology	48
4.2.3. Volume fraction of β phase.....	49
4.3. Microstructure of Arcam S12 Components	51
4.3.1. Grain Size and Morphology.....	51
4.3.2. Description of $\alpha + \beta$ phase morphology	61
4.3.3. Volume fraction of β phase.....	67

4.3.4. Transmission Electron Microscopy of S12 - Produced Components	68
4.3.5. Scanning Transmission Electron Microscopy of S12 – Produced Component.....	75
4.4. Microstructure of Arcam A2 - Produced Component.....	81
4.4.1. Grain Size and Morphology.....	81
4.4.2. Description of $\alpha + \beta$ phase morphology.....	86
4.4.3. Volume fraction of β phase.....	88
4.4.4. Transmission Electron Microscopy of A2 - Produced Component...	89
4.5. Porosity	96
4.5.1. Porosity of Arcam S12 – Produced Components	96
4.5.2. Porosity of Arcam A2 – Produced Component	107
4.5.3. Porosity and Aggregation in PREP Powder.....	114
4.6. Transmission Electron Microscopy Sample Preparation.....	117
4.6.1. Electropolishing	117
4.6.2. Solution to the Porosity Problem	126
4.6.2. Focused Ion Beam.....	127
5. CONCLUSIONS.....	131
6. FUTURE WORK.....	134
6.1. Electron Backscatter Diffraction of Growth Plane Normal.....	134
6.2. Hot Isostatic Press (HIP) Arcam Components.....	134
6.3. Temperature Measurement of Build Plane	135
6.4. Initial Densification of Powder Bed	135
6.5. Resistivity Measurement of Powder Bed.....	135
6.6. Investigate Possible Presence of FCC Product at α/β Interfacial Phase.....	136
6.7. Implementation of Digital Image Processing for Volume Fraction of Phases .	136
REFERENCES	137

LIST OF TABLES

Table 2.1. Titanium alloy composition details used for electron trajectory simulation.....	15
Table 3.1. Electropolishing conditions for Ti-6Al-4V	32
Table 4.1. Volume fraction of beta phase for forged turbine blade sample.....	50
Table 4.2. Grain size measurements for Arcam S12 produced components.....	60
Table 4.3. Volume fraction of beta phase for Arcam S12 produced components	68
Table 4.4. Summary of all grain size measurements for all samples	60
Table 4.5. Summary table for volume fraction of beta phase for all samples.....	89

LIST OF FIGURES

Figure 2.1.	Arcam S12 and A2 EBM units [2].....	7
Figure 2.2.	Arcam S12 EBM hardware exterior (left) and schematic of solid object build chamber [8].....	8
Figure 2.3.	SEM secondary electron images of gas atomized 2024 Al powder.....	10
Figure 2.4.	SEM secondary electron images of Starmet PREP Ti-6Al-4V powder.....	11
Figure 2.5.	PREP Powder size distribution used in this study	12
Figure 2.6.	Schematic of electron beam–sample and powder geometry.....	14
Figure 2.7.	CASINO electron trajectory model for powder bed on solid titanium alloy	16
Figure 2.8.	Portion of titanium–vanadium binary phase diagram at 6 wt.% aluminum [1].....	17
Figure 2.9.	Widmanstätten structure formation [13].....	19
Figure 2.10.	Melt pool profiles for surface morphology as it relates to temperature and surface tension	21
Figure 3.1.	XY sample grown in the Arcam S12. A) Sample schematic. B) Actual specimen	23
Figure 3.2.	XZ sample grown in the Arcam S12. A) Sample schematic. B) Top view of actual specimen. C) Bottom / side view of actual sample	24
Figure 3.3.	Horizontal Cylinder (HC) sample grown in the Arcam A2. A) Sample schematic. B) Actual specimen. C) Sectioned specimen.....	26
Figure 3.4.	XY, XZ and HC sample geometries. Surface planes investigated in this study are designated by the shaded area and labeled with identification nomenclature	27
Figure 3.5.	Forged Ti-6Al-4V helicopter turbine blade (TB)	28

Figure 3.6.	Illustration of active regimes associated with electropolishing for current as a function of voltage.....	30
Figure 4.1.	SEM image of XY Face exterior surface. Growth direction and incident Arcam electron beam are normal to page	41
Figure 4.2.	SEM image of XY Side exterior surface	42
Figure 4.3.	SEM image of XZ Face exterior surface	43
Figure 4.4.	SEM image of XZ Face exterior surface featured in Figure 4.3.....	44
Figure 4.5.	Optical micrograph of XZ Face mounted, polished and etched	45
Figure 4.6.	SEM image of HC Face exterior surface, top dead center.....	46
Figure 4.7.	SEM image of HC Face exterior on a curved surface	47
Figure 4.8.	Optical micrograph of a Ti-6Al-4V forged turbine blade.....	48
Figure 4.9.	SEM micrograph of Ti-6Al-4V forged turbine blade	50
Figure 4.10.	Low magnification optical image of mounted XY Cross Section samples as used for optical and scanning electron microscopy.....	53
Figure 4.11.	Low magnification optical images of mounted XZ Side sample as used for optical and scanning electron microscopy	54
Figure 4.12.	Low magnification optical image of mounted XY Face sample as used for optical microscopy and SEM. Component growth is normal to XY Face orientation.....	55
Figure 4.13.	Low magnification optical image of mounted XZ Cross Section sample as used for optical microscopy and SEM. Component growth is normal to the Cross Section plane for XZ sample	56
Figure 4.14.	Optical micrograph of XY Face sample	57
Figure 4.15.	Optical micrograph of XZ Cross Section.....	58
Figure 4.16.	Optical micrograph of XZ Face	59
Figure 4.17.	Optical micrograph of XZ Side.....	60

Figure 4.18.	Optical micrograph of XY Side sample. Arrow identifies prior beta grain boundary	63
Figure 4.19.	Optical micrograph of XY Face sample	64
Figure 4.20.	SEM micrograph image of XY Face	65
Figure 4.21.	SEM micrograph image of XY Cross Section.....	66
Figure 4.22.	SEM micrograph image of XZ Side	67
Figure 4.23.	SEM micrograph image of XZ Cross Section	68
Figure 4.24.	a) Bright field TEM micrograph of XY Side sample and, b) diffraction pattern. Zone axis = [01-12]	70
Figure 4.25.	Bright field TEM micrograph of XY side sample	71
Figure 4.26.	Bright field TEM micrograph of XZ Face sample.....	73
Figure 4.27.	a) Bright field TEM micrograph of XZ Face sample and, b) diffraction pattern. Zone axis = [01-10]	74
Figure 4.28.	Bright field TEM image of XZ Face FIB sample.....	75
Figure 4.30.	STEM image of XZ face FIB sample at 30 KV. Green arrow identifies EDS dot map region.....	76
Figure 4.31.	STEM image of XZ Face FIB sample at 30 KV. Area used for EDS dot mapping	78
Figure 4.32.	EDS vanadium (in green) map image of XZ face FIB sample at 30 KV	78
Figure 4.33.	STEM image of XZ face FIB sample at 30 KV. Area used for EDS line scan	79
Figure 4.34.	EDS line scan across two-phase region from STEM image of XZ Face FIB sample at 30 KV. Chart shows relative amounts as a function of position	80
Figure 4.35.	EDS spectrum from line scan from STEM image of XZ face FIB sample at 30 KV.....	81

Figure 4.36.	Low magnification optical images of mounted horizontal cylinder (HC) sample as used for optical and scanning electron microscopy	82
Figure 4.37.	Low magnification optical images of horizontal cylinder (HC) sample used for optical and scanning electron microscopy. Component growth is normal to the face orientation for HC sample	83
Figure 4.38.	Optical micrograph of HC Face (normal to growth direction)	84
Figure 4.39.	Optical micrograph of HC Face (normal to growth direction)	85
Figure 4.40.	Optical micrograph of HC cross section (parallel to growth direction)	86
Figure 4.41.	SEM micrograph of HC Face	88
Figure 4.42.	SEM micrograph of HC Cross Section	89
Figure 4.43.	Bright field TEM micrograph of HC Face and diffraction pattern. Zone axis = [5-1-43]	91
Figure 4.44.	a) Bright field TEM micrograph of HC Face and diffraction pattern. b) Zone axis = [-12-13]	92
Figure 4.45.	a) Bright field TEM micrograph of HC Cross Section and diffraction b) pattern. Zone axis = [10-11]	94
Figure 4.46.	a) Bright field TEM micrograph of HC Cross Section and diffraction pattern. b) Zone axis = [01-10]	95
Figure 4.47.	TEM micrograph of HC Face, alpha/ beta phase interface region	96
Figure 4.48.	Optical micrograph of XY Cross Section sample near build plate	98
Figure 4.49.	Optical micrographs of XY Side sample at the build plate	98
Figure 4.50.	SEM micrograph image of XY Side plane near the build plate	100
Figure 4.51.	SEM micrograph image of XY Cross Section illustrating component fabrication defects	101

Figure 4.52.	Increased magnification SEM micrograph of XY Cross Section illustrating component fabrication defect from Figure 4.51	102
Figure 4.53.	SEM micrograph images of XY Face illustrating incomplete packing and sintering defect.....	103
Figure 4.54.	Increased magnification SEM micrograph of XY Face illustrating component fabrication defect from Figure 4.53. Arrows show alpha grain boundary	104
Figure 4.55.	SEM micrograph of XY Cross Section.....	105
Figure 4.56.	SEM micrograph of XZ Side	106
Figure 4.57.	SEM micrograph of HC Face	108
Figure 4.58.	SEM micrograph of defects in HC Face plane	109
Figure 4.59.	SEM micrograph of defect in HC Face plane.....	110
Figure 4.60.	SEM micrograph of HC Cross Section.....	111
Figure 4.61.	SEM micrograph of HC Cross Section.....	112
Figure 4.62.	SEM micrograph of HC Cross Section.....	113
Figure 4.63.	Semi-hollow Ti-6Al-4V PREP powder particle	114
Figure 4.64.	Ti-6Al-4V PREP powder showing porous particle	115
Figure 4.65.	Ti-6Al-4V PREP powder showing agglomerated particles	116
Figure 4.66.	3mm disc XY Cross Section Ti-6Al-4V TEM sample in Progress.....	118
Figure 4.67.	3mm disc XY Cross Section Ti-6Al-4V TEM sample in progress. (Same sample in Figure 4.66).....	119
Figure 4.68.	Electropolished XY Cross Section Ti-6Al-4V 3mm disc TEM Sample.....	120
Figure 4.69.	Electropolished XY Cross Section Ti-6Al-4V 3mm disc TEM Sample.....	120

Figure 4.70.	Electropolished XY Cross Section Ti-6Al-4V 3mm disc TEM Sample.....	121
Figure 4.71.	Electropolished XY Cross Section Ti-6Al-4V 3mm disc TEM Sample.....	122
Figure 4.72.	Secondary electron SEM image of perforation edge of an electropolished XY Cross Section Ti-6Al-4V 3mm disc TEM sample shown in Figure 4.71	123
Figure 4.73.	SEM micrograph of HC face Ti-6Al-4V TEM sample in progress.....	124
Figure 4.74.	SEM micrograph of the surface of an HC face Ti-6Al-4V TEM sample exhibiting porosity	125
Figure 4.75.	Low magnification optical image of XZ face FIB sample as affixed to TEM sample mount.....	127
Figure 4.76.	Image of XZ Face FIB sample (in progress)	128
Figure 4.77.	Image of XZ Face FIB sample after final thinning.....	129
Figure 4.78.	XZ face FIB sample as affixed to TEM sample mount. Bottom image shows sample after final thinning of left side which is approximately 50 nm in thickness	130

1. STATEMENT OF PROBLEM

The United States military operates aircraft that were initially placed into service as early as the 1960's. After an airplane or helicopter achieves or exceeds a predetermined number of service hours the unit undergoes a complete ground-up restoration at rebuild depot stations such as NAVAIR at Cherry Point. Many cast and forged components necessary for the remanufacture and repair of these aging aircraft are no longer available from the original manufacturers because the original tooling used for the manufacture of the components are also no longer available and would be extremely expensive to construct. The extensive costs associated with producing the required tooling for the vast number of different components and the limited quantity demanded of each have lead to the pursuit of other means by which to produce discontinued aircraft components.

Additive manufacturing processes using electron beam melting (EBM) are being studied for the production of replacement aircraft components because functional parts with complex geometries can be manufactured without the need of expensive tooling. Arcam AB[®] has developed an EBM process which can potentially manufacture, using an additive manufacturing process, fully functional, flight-worthy components using an additive manufacturing process.

The broad objective of this study is to microstructurally evaluate prototype components manufactured from Ti-6Al-4V alloy powders by the Arcam process. A limited amount of components (only three individual specimens) were available for evaluation and therefore this study does not purport to assess the potential of the Arcam EBM process. The

samples were delivered from early stages of implementation of Arcam processing at NC State University and are not representative of the current work that is being conducted on Arcam EBM process optimization. The Arcam A2 EBM at NC State University is one of the first A2 models installed in North America and the sample used in this study was one of the first pieces to be produced by it. At the time of the A2 installation, the existing Arcam S12 unit was being dedicated to producing components from other alloys, such as aluminum. Components produced by the Arcam S12 and Arcam A2 machines will be evaluated and compared. Because of the complex combination of processing parameters inherent to the Arcam process (e.g., electron beam diameter, powder density and scan rate; powder particle size, shape, and packing efficiency; and, component geometry and size) it is expected that production of components with predictable, consistent microstructures and physical properties will be challenging. The following are the key questions addressed by this research.

1. Are there any significant differences between the two Ti-6Al-4V components produced by the Arcam S12 EBM machine and the one component produced by the A2 EBM machine regarding microstructure?
2. Are the percentage and distribution of alpha and beta phases comparable between the two Ti-6Al-4V components produced by the Arcam S12 EBM machine, the one component produced by the A2 EBM machine, and that for a forged Ti-6Al-4V alloy component? Are these strongly influenced by some processing parameters.

3. Are there any defects within these samples from early builds such as inclusions or porosity within Arcam processed parts? If so, are these defects sufficient in size, shape and distribution to potentially affect physical properties?

2. INTRODUCTION

2.1 The Arcam Electron Beam Melting (EBM) Process

Rapid prototyping (RP) refers to various techniques that create three-dimensional shapes without dies or tooling. As reviewed by Dinda [1] RP includes processes such as selective laser sintering (SLS), stereolithography, direct laser fabrication (DLF), direct metal deposition (DMD), and electron beam melting (EBM). These additive processes transform computer aided design (CAD) files of an object into a solid three-dimensional object, which may be either purely geometrically accurate or fully functional.

In what is referred to by Arcam as *Adding Technology* and *CAD-to-Metal* [2], a functional part is built layer-by-layer as layers are sequentially fused and solidified in selected areas. The Arcam EBM process used for rapid component prototyping is operationally similar to the rastering of an electron beam in a scanning electron microscope. In the Arcam process a rastering high power electron beam forms near-net shape components by selectively melting sequential finite-thickness layers of alloy powder in selected area determined by the CAD file of the component geometry. The Arcam process has been successfully implemented by Adler Ortho [3] group of Italy in the fabrication of an acetabular cup from Ti-6Al-4V for surgical implants in humans where implants need to be specifically shaped for each patient. The implants have been specifically designed to contain 700 μ m pores on the surface to promote grafting of new bony tissue without the use of any fiber-tissue interposition [2].

A study on direct metal deposition (DMD) by Dinda, et. al [1], have shown the microstructures of as-grown laser-deposited Ti-6Al-4V to have fine Widmanstätten

morphology and columnar grains roughly parallel to the incident beam and component growth direction. The length of the columnar grains varied from 5 to 15 mm. The width of the grains were reported to be in the range of 0.15 to 0.8 mm with an average width of 0.3 mm. Tensile and yield strengths of as-deposited components were 1163 ± 22 and 1105 ± 19 MPa respectively where the tensile axis was perpendicular to the deposition direction. Elongation under tension was approximately 4 %.

Using direct laser fabrication with a gas-atomized Ti-48Al-2Mn-2Nb powder, Srivastava, et. al, have observed microstructures that range from coarse dendritic, to fine equiaxed, to fine dendritic with increasing laser power [4]. Fine microstructures are expected due to the high cooling rate in the DLF process. Higher laser power is correlated with coarse dendritic microstructure due to high superheating of a larger melt pool and longer solidification times. Finer and equiaxed microstructures observed from this study are proposed to be due to poor heat dissipation and low cooling rates at lower laser power.

Electron beam melting has been used for many years for welding, zone refinement, refinement of inclusions, and reclamation of scrap [5]. More recently EBM has been advancing as a viable means of manufacturing specialty parts and complex-shaped objects that have comparable properties to those of cast components. Traditionally, part fabrication using EBM has been restricted to rapid part prototyping and research and development environments. Because of its many advantages, especially cost savings, EBM is gaining acceptance as a standard technique for manufacturing complex-geometry functional replacement components that are unavailable from original manufacturers. Standing at 7 ft.

tall, the Arcam EBM units efficiently utilize floor space by residing in a 6 ft. wide by 4 ft. deep footprint.

Earlier studies of Ti-6Al-4V alloy parts produced with the Arcam system suggest that mechanical properties such as 0.2% yield strength (149 ksi), ultimate tensile strength (156 ksi), and percent elongation (10.7 %) exceed those for cast parts [6]. Tensile test bars produced via Arcam EBM [6] have been shown to have tensile strengths that exceed strength values of forged Ti-6Al-4V (0.2% yield strength 120 ksi [7]). Components produced by the Arcam EBM process must meet the minimum standards in Aerospace Material Specification (AMS) 4999 set forth by The Engineering Society For Advancing Mobility Land Sea Air and Space (SAE International) which states that in the beam velocity direction the tensile strength be 130 ksi, 0.2% yield strength be 116 ksi, and elongation be 4%, which is the claim made by Bass [6]. There have been no transmission electron microscopy data published on Ti-6Al-4V components that have been grown in the Arcam S12 or the Arcam A2 EBM machines.

Problems facing acceptance of components produced by the Arcam EBM process include porosity issues and the need for finishing the exterior surfaces. Surface morphology of as-built parts is non-uniform and uneven, inferior in quality in comparison to a sand cast part. Although finish machining is necessary for most applications, parts are built close to final shape, which minimizes scrap and is critical for components made from materials in relatively scarce supply or materials which originate from sources outside the U.S.

2.2 The Arcam EBM Process Apparatus

The machines used for this study at North Carolina State University are the Arcam EBM S12 and A2 models as shown in Figure 2.1. These systems consist of an electronics control panel and a processing chamber evacuated with a turbomolecular pump backed by a mechanical roughing pump. The processing chamber operating pressure is approximately 1×10^{-6} Torr. These systems incorporate an electron beam which is generated and scanned in a manner similar to the electron beam in a scanning electron microscope (SEM). The electron beam position is controlled by scan coils as the focused probe is rastered across the powder bed according to the finite cross-sectional area element of the solid object as specified by the CAD file. After each layer of alloy powder has been melted and fused in the specific areas for that specific layer, the build table is lowered approximately 100 microns. Additional powder is delivered from the powder dispensing hopper and spread/raked over the previously solidified layer.



Figure 2.1. Arcam S12 and A2 EBM units [2].

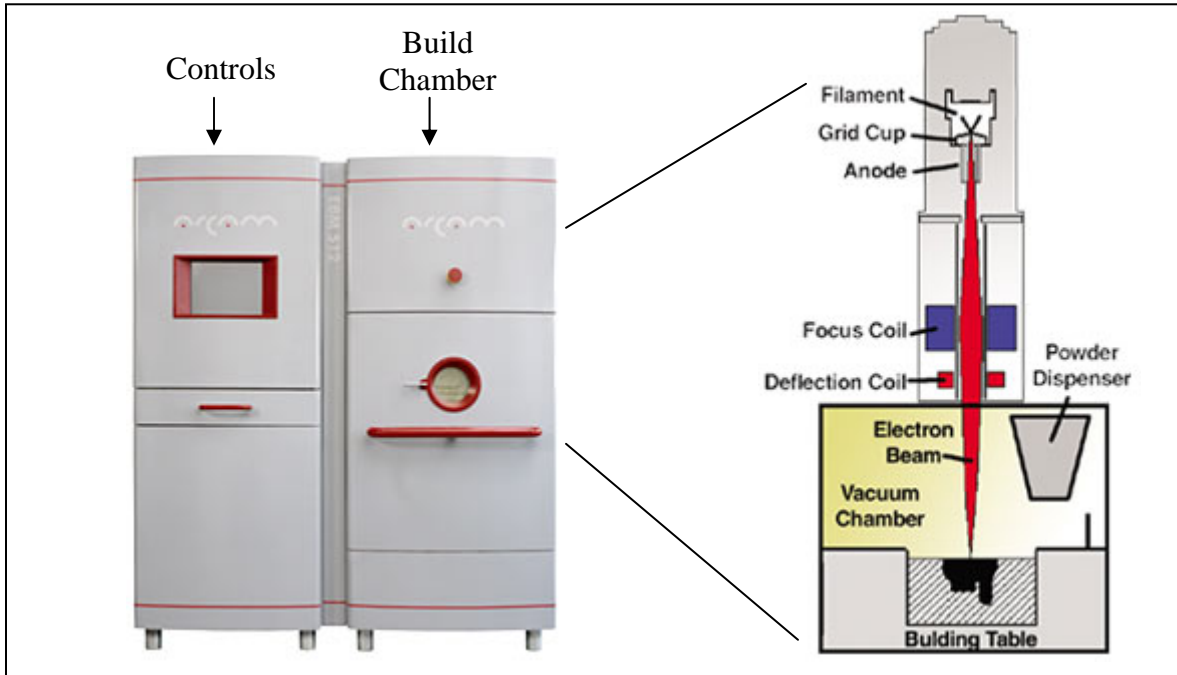


Figure 2.2. Arcam S12 EBM hardware exterior (left) and schematic of solid object build chamber [8].

The electron source is a tungsten filament thermionic emission electron gun and electromagnetic optics are used to focus the beam. Beam potential, E_B , is constant at 60 keV. Typical beam current, i_B , values present during the Arcam EBM process range from 3 to 5 mA for aluminum and up to 30 mA for titanium alloys and large areas to be melted. Beam power P_B is rated at 3500W [2]. Note that these currents are many orders of magnitude higher than those encountered in an ordinary SEM, which are typically on the order of nanoamps. Equation 2.1, the brightness equation, could be used in this instance to describe electron gun performance as it includes current density per solid angle α (in steradians) [9] and d is the beam diameter at the powder bed surface, also referred to as probe size or spot size.

$$\beta = \frac{4i_B}{\pi^2 d^2 \alpha^2} \quad (2.1)$$

During EBM processing the beam travels parallel to the powder bed at a velocity V_B and will be assumed for this study to be normal to the processed surface, which is stationary. Electron beam scan rates range from 0.1 m/s to 1000 m/s and will be used for V_B . Scan patterns of the focused beam can be varied also similar to integration image capture options on many SEMs. Variations on beam control include multiple simultaneous actions such as small circular patterns creating a swirling of the melt pool during total planar scan.

2.3 Precursor Material (Pre-Alloyed Powder)

Pre-alloyed powders currently used for EBM are prepared by a gas atomized (GA) process and a plasma rotating electrode process (PREP), a proprietary process for producing ultra-clean spherical powders with smooth surfaces as shown in Figure 2.3. In general, the plasma rotating electrode process takes place as an alloy bar acts as a consumable electrode opposite a plasma in an inert gaseous environment. The alloy bar electrode is rotated about its axis as it is consumed and kept at a constant distance from the plasma. Molten droplets freeze as they are thrown from the bar due to centrifugal force [10]. This process has a high yield at lower energy inputs than the gas-atomized process [11].

Metal powder produced from gas-atomization, wherein particles are prepared from the melt in a pressurized inert environment yielding clean, spherical particles. The uniformity of particle size and shape is not as regular compared to powder prepared by the PREP

method. Figure 2.3 illustrates the surface roughness and irregularity of shape associated with an aluminum alloy powder produced by gas atomization.

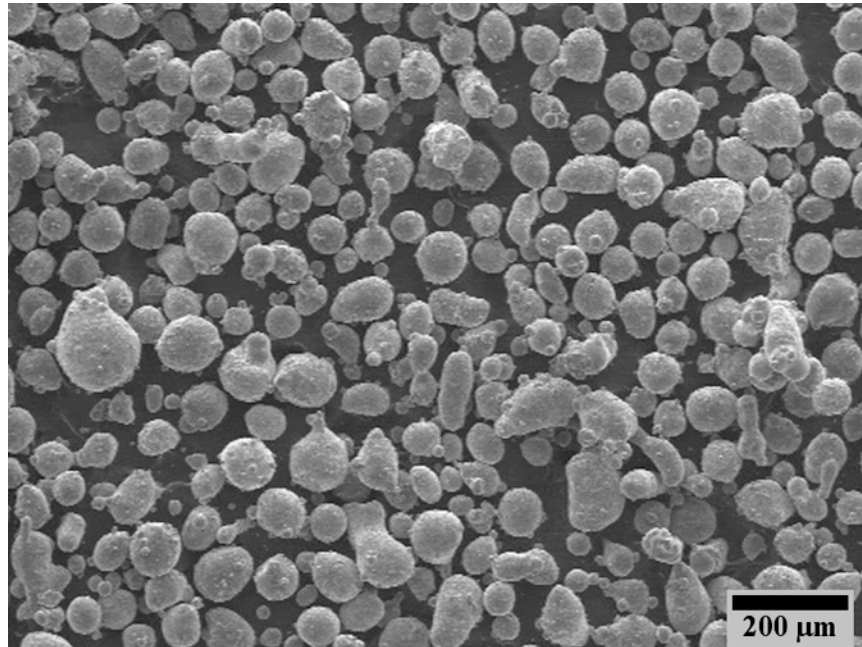


Figure 2.3. SEM secondary electron images of gas atomized 2024 Al powder.

This study used a Ti-6Al-4V alloy powder from Starmet which was prepared by the PREP method. From Figure 2.4 the size and shape distribution is well represented. The spheres range from 8 μm to 118 μm . The particle size and distribution obtained from several scanning electron micrographs is plotted in Figure 2.5. Two sets of orthogonal diameter measurements for a total of four diameters per particle were made and averaged to obtain the particle diameter from one hundred particles. The average particle size is 67 μm .

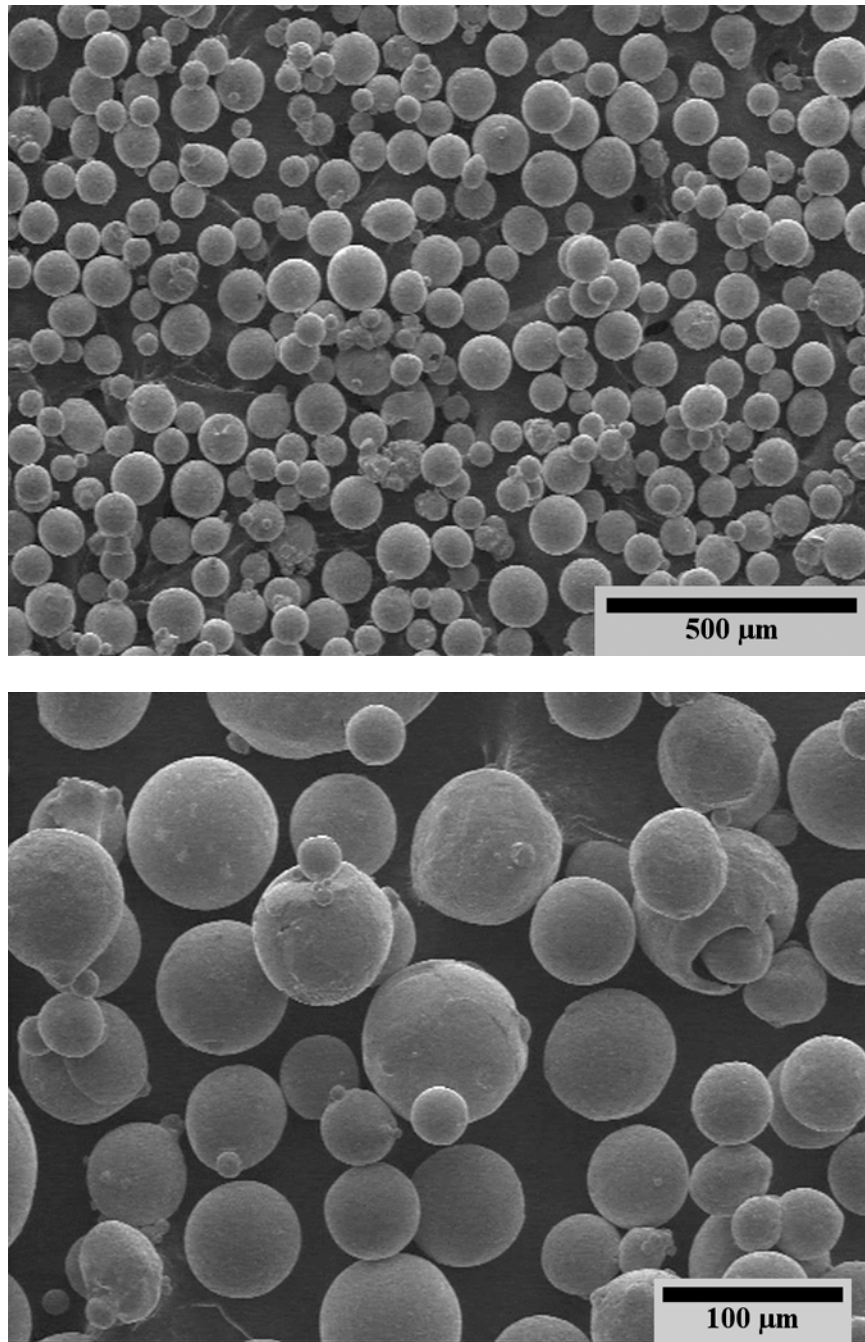


Figure 2.4. SEM secondary electron images of Starmet PREP Ti-6Al-4V powder.

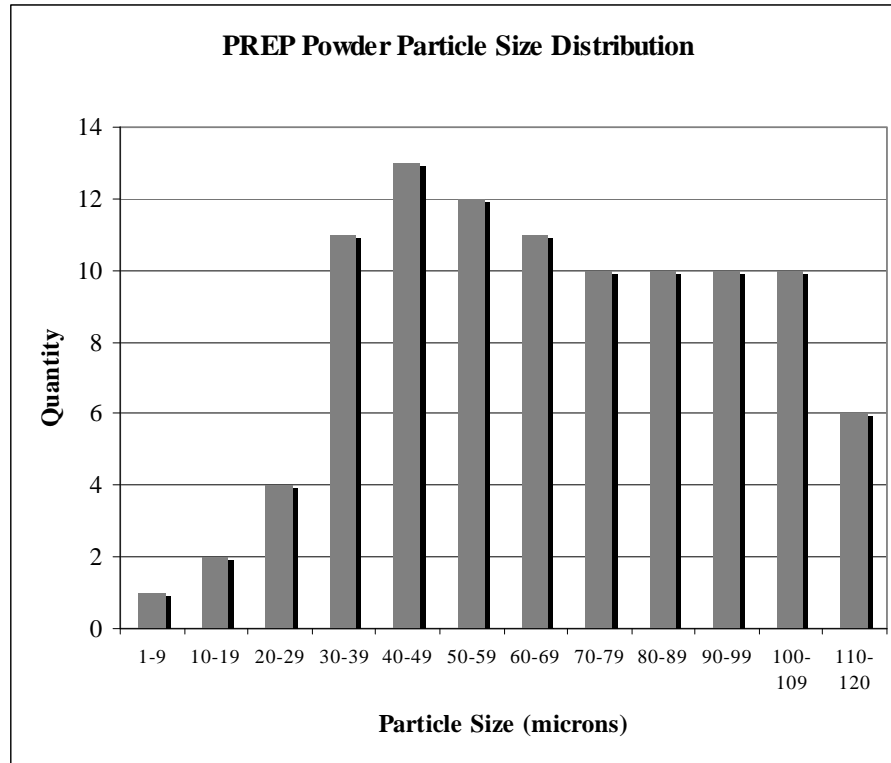


Figure 2.5. PREP Powder size distribution used in this study.

2.4. Component Fabrication Process

The following discussion describes the basic Arcam EBM process for fabrication of a part. The process begins with the 60 keV electron beam preheating (760°C for 30 minutes) a stainless steel build plate that serves as the foundation. Next a 4 inch thick layer of metal powder is uniformly distributed on to the build plate and then preheated, again with the electron beam to aid initial particle cohesion. A thermocouple in contact with the bottom of the build plate provides temperature data. The temperature at the bottom of the build plate decreases as a function of time during the growth process. The temperature decreases as the

distance between the build plate and the electron beam increases. The heat dissipates to the excess powder surrounding the component being solidified.

The electron beam that performs the melting of the alloy powder is swirled in a triangular pattern 200 to 300 microns in width as it is rastered across the powder bed according to the CAD file cross section.

Once the first layer has been melted, the build plate is lowered along the z direction by 100 μm . A hopper delivers additional alloy powder approximately 100 μm in height over the freshly melted top layer. The powder bed is not packed between successive electron beam processing steps. Two spreaders rake the powder layer in an effort to level the bed prior to the rastering of the electron beam which follows the next cross sectional pattern of the solid object CAD file. This is repeated until all layers that form the solid object are created. Figure 2.6 is a schematic of the build plane and EBM build process.

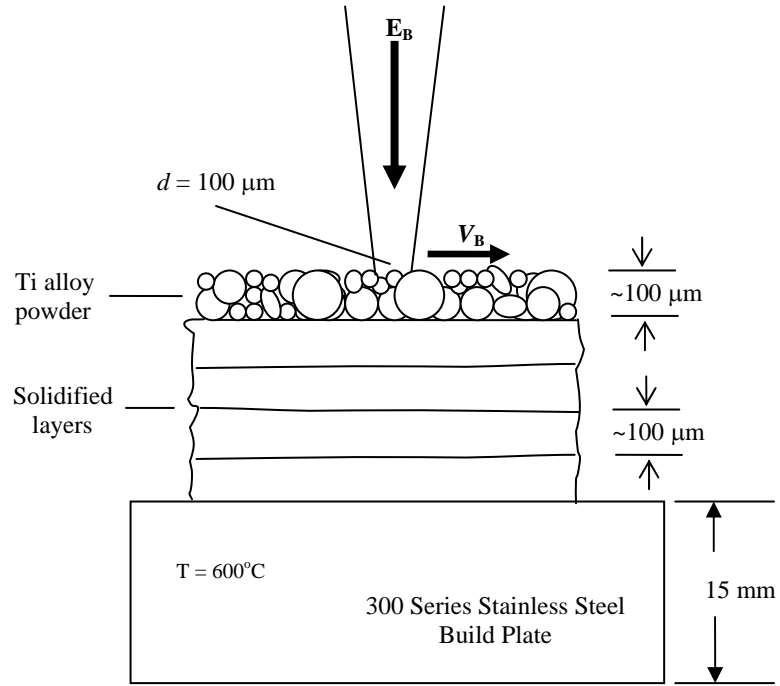


Figure 2.6. Schematic of electron beam–sample and powder geometry.

2.5. Electron Beam - Powder Bed Interaction

The maximum distance an electron can travel in a given material can be calculated using the Kanaya and Okayama equation (eqn 2.4) for electron range in microns, R_{KO} , which more specifically is the distance an electron travels until it has zero energy [9. Goldstein].

$$R_{KO} = \frac{0.0276A}{Z^{0.89}\rho} E_0^{1.67} (\mu m) \quad (2.4)$$

A is the atomic weight, Z is the atomic number and E_0 is the accelerating voltage in keV, which is 60 keV in this case. Electron range is inversely proportional to density, ρ , which is known for the alloy of interest to be 4.43 g/cm^3 .

Table 2.1. Titanium alloy composition details used for electron trajectory simulation.

Alloy Element	Ti	Al	V
wt. %	90	6	4
A (g/mol)	47.9	26.98	50.94
Z	22	13	23

Since we have an alloy, effective atomic weights and numbers must be calculated. Trace elements will be assumed to have negligible effects on electron range and elemental losses experienced during component fabrication.

$$A_{effective} = \sum_{i=1}^n A_i w_i (0.90)(47.9) + (0.06)(26.98) + (0.04)(50.94) \text{ (g/mol)} = 46.77 \text{ (g/mol)}$$

$$Z_{effective} = \sum_{i=1}^n Z_i w_i (0.90)(22) + (0.06)(13) + (0.04)(23) = 21.5$$

$$\text{With corrected values, } R_{KO} = \frac{0.0276(46.77 \text{ g/mol})}{(21.5)^{0.89} (4.43 \text{ g/cm}^3)} (60 \text{ keV})^{1.67} (\mu\text{m}) = 17.8 \mu\text{m}$$

To simulate the powder bed as it is used in the Arcam EBM process, the density of a loose powder bed was determined experimentally to be 2.4 g/cm³ by weighing a sampling of the Starmet Ti-6Al-4V powder sample in a small cylinder of volume equal to 8.75 cm³ without packing powder or tapping the side of the cylinder.

A Monte Carlo computer simulation was used to predict the electron beam-sample interaction volume. The layered sample geometry was simulated in CASINO [12] by setting the appropriate thickness for each layer and adjusting the density of the top 100 μm powder layer to simulate the density of the loose powder. The graphical output to this computational model shows electron trajectories in a solid. Electron paths in red color indicate electrons

that escape the material. Figure 2.7 shows the simulation results using 60keV electrons, a 100 μm stationary probe size, and a 100 μm thick layer of powder on a solid substrate.

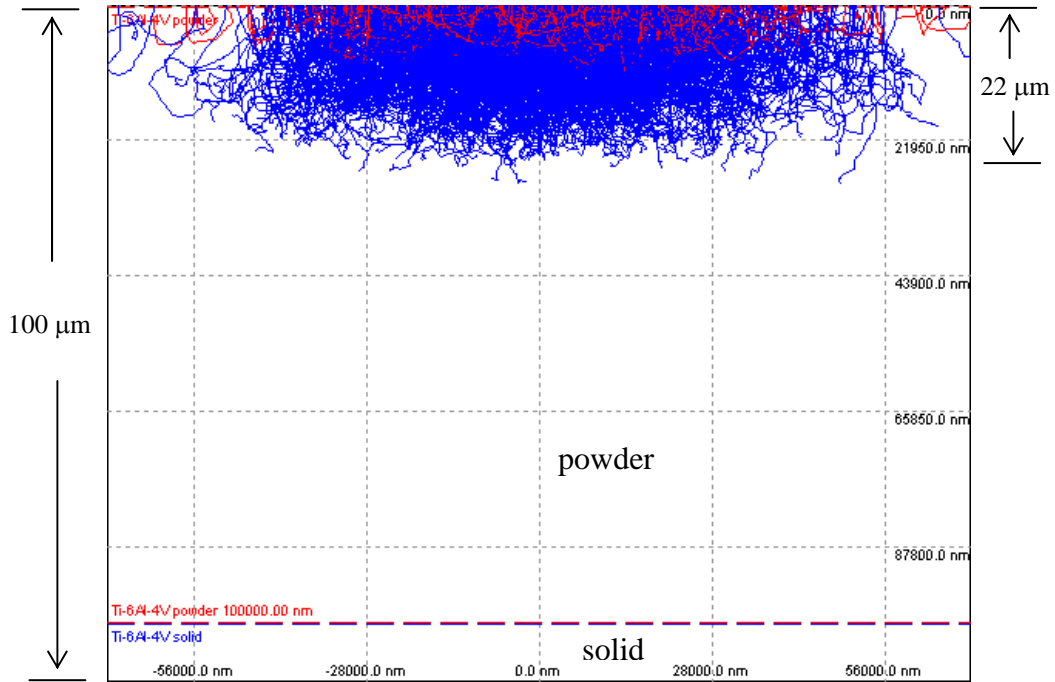


Figure 2.7. CASINO electron trajectory model for powder bed on solid titanium alloy.

From the simulation output it is evident that the incident 60 kV electrons do not penetrate past the powder level and into the previous melted layer. This simulation also does not account for the elevated temperature which could further decrease conductivity.

2.6. Physical Metallurgy of Ti – 6Al – 4V Alloy

Ti-6Al-4V is a duplex microstructure (α and β) alloy in equilibrium when heated above 980°C and cooled to room temperature. Alpha (α) refers to hexagonal close packed (HCP) crystal structure phase and beta (β) refers to body centered cubic (BCC) crystal structure phase. Figure 2.8 shows an area of the titanium – vanadium binary phase diagram at 6 wt.% aluminum. Elemental titanium is HCP at room temperature but transforms to BCC above 980 °C, the beta transus temperature. Addition of vanadium (V) stabilizes the BCC β phase to temperatures below 980 °C, with the lowest β to α phase as shown in Figure 2.8.

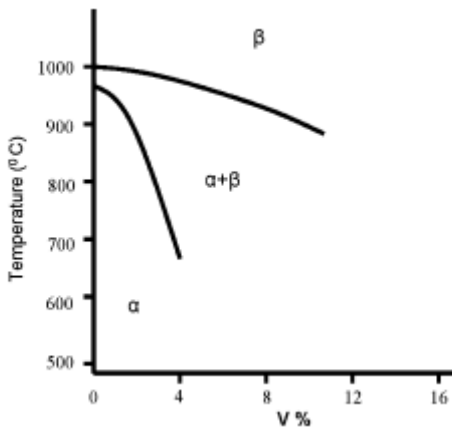


Figure 2.8. Portion of titanium–vanadium binary phase diagram at 6 wt.% aluminum [1].

Aluminum additions decrease the β phase stability and raises the transformation temperature for β to α . Thus titanium alloys such as Ti-6Al-4V with the additions of both V and Al often exhibit duplex $\alpha + \beta$ microstructures. Ti-6Al-4V alloys are technologically important because they have excellent strength and toughness in addition to exhibiting good

oxidation resistance at high service temperatures [13, 14]. In optical micrographs the alpha phase appears white and beta phase appears black.

A variety of microstructures and properties arise from various heat treatments and mechanical processing. In general there are two types of microstructures. Alpha/beta processed microstructures refer to thermo-mechanically processing the alloy below the beta transus and resulting in equiaxed α grains dispersed in a β matrix. Beta processed microstructures result in Widmanstätten α lath precipitates distributed in a matrix of β phase from the alloy being thermo-mechanically above the beta transus [24].

Figure 2.9 shows a schematic of Widmanstätten structure formation upon cooling from the beta region into the $\alpha + \beta$ region of the Ti-V phase diagram at 6%Al.

Widmanstätten microstructure develops when Ti-6Al-4V is slowly cooled from the beta region [13]. The alpha plates initially form at the (prior) beta grain boundaries below the beta transus with a crystallographic relationship to the beta phase from which it originates [13]. Acicular plates are formed as the alpha grows faster along the common plane than it does perpendicularly to the common plane. The beta phase can exist between the alpha plates.

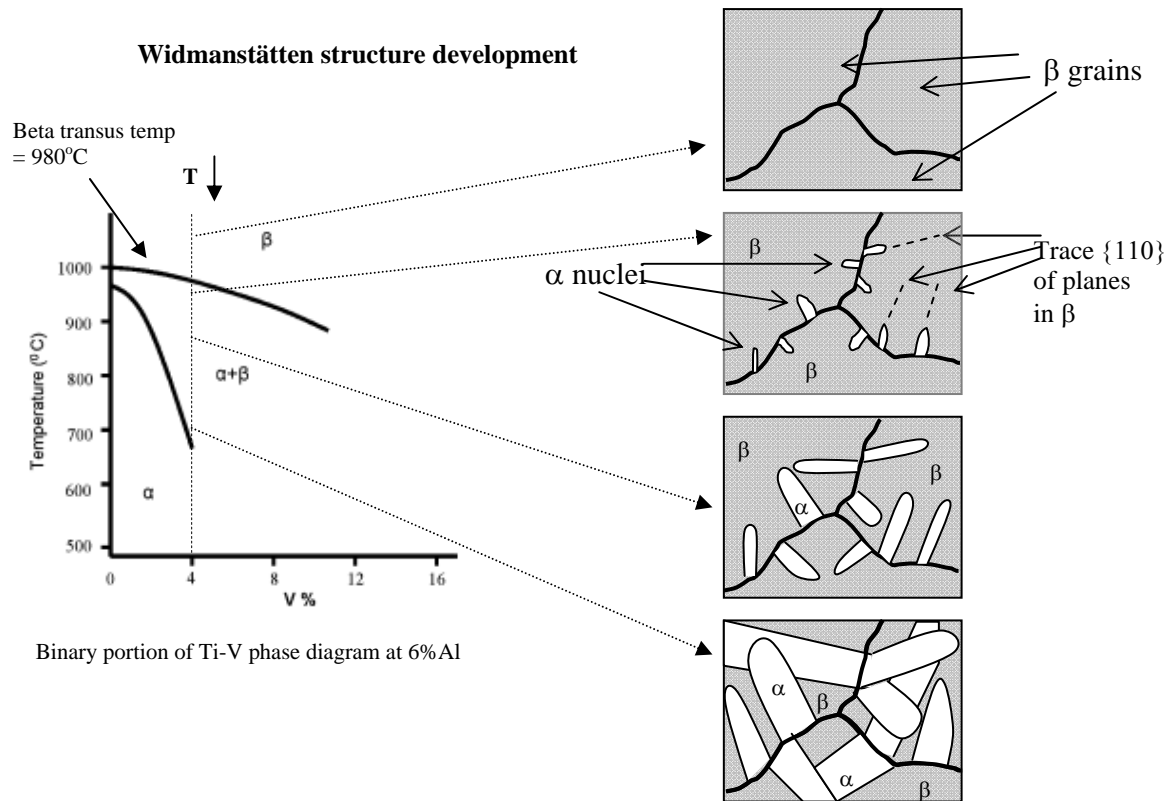


Figure 2.9. Widmanstätten structure formation [13].

2.7 Microstructure of Arcam - Fabricated Ti-6Al-4V Components

Concurrent studies of Arcam S12-produced components from Ti-6Al-4V have observed columnar grains aligned perpendicular to the growth plane and can extend the length of the sample, which are several millimeters. Columnar grain growth is along the direction of the incident beam direction. Grain structure was equiaxed at the cross sectional area of the columns and roughly 100 to 200 μm in diameter [6]. Microstructure morphology has been noted as fine acicular α (HCP) with β (BCC) phase located between the α phase along with intergranular β (BCC) along α (HCP) grain boundaries [6, 15]. Subsequent heat

treatments proved to disrupt columnar grains to some extent while creating coarse α laths and blocky α with discontinuous and coarse α at grain boundaries. The formation of colonies following heat treatments above the β transus were also reported [15].

Murr et al. [16] conducted a study on the microstructure and mechanical properties of Ti-6Al-4V as-deposited using an Arcam S400 EBM. The resultant microstructure was described as Widmännstätten-like, consisting primarily of acicular α -plate.

The claim was also made that as-built components are fully dense and homogeneous, although they state that the alpha plate thickness is wider at the bottom of a 6.8 cm tall vertically grown cylindrical coupon than it is near the top of the coupon [16]. Murr et al. made no mention of columnar grain structure.

2.8. Surface Morphology of Beam-Melted Metal

For laser and electron beam-melted metals, the morphology of the melted surface takes on that shown in Figure 2.10 as the incident beam forms a melt pool. The temperature profile is approximated as Gaussian and skewed along the electron beam motion. The surface tension energy γ varies as shown graphically in Figure 2.10 due to the temperature variation of the melt pool and the negative temperature coefficient of surface tension for liquids [17]. Material is pulled from the center of the beam spot by the combined actions of the surface temperature and the metal flow in the melt pool causing material to pile up towards the perimeter of the melt pool. The z-axis is consistent with the growth direction of objects in the Arcam EBM machines.

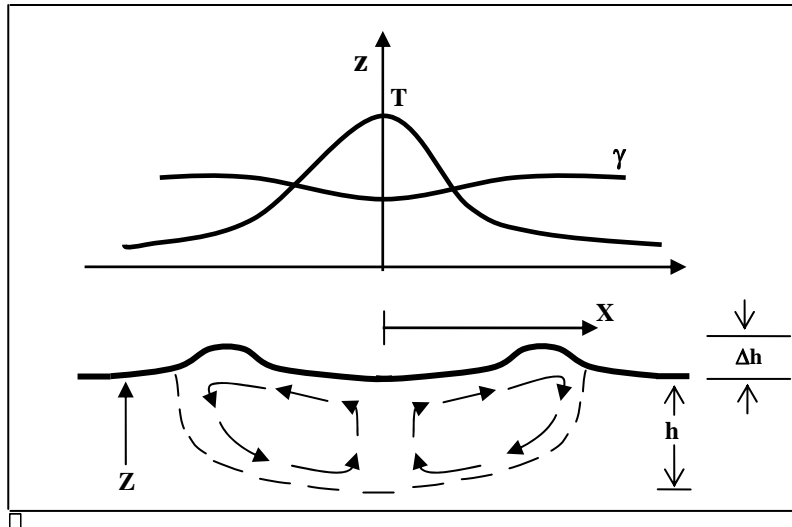


Figure 2.10. Melt pool profiles for surface morphology as it relates to temperature and surface tension.

3. EXPERIMENTAL PROCEDURE

In the Experimental Procedure chapter the samples used for this study are introduced and categorized by the orientation in which they were grown in the Arcam EBM machines and how samples from the bulk material were prepared for characterization. A total of three samples were available from the Arcam EBM machines; two from the Arcam[®] S12 and one from the Arcam[®] A2. Due to the limited number of samples used in this study, the findings reported herein may not be representative of current components being produced by the Arcam S12 and A2 machines at NC State University.

Specific microscopy techniques used are presented including the associated makes and models of equipment employed for this study. The last section of this chapter focuses on sample preparation techniques used for TEM and STEM imaging.

3.1. Sample Geometry and Growth Orientation

Tensile bars grown in the Arcam[®] EBM process and slated for mechanical property testing (per ASTM E-8 standard method) are categorized by the directionality of growth (along the z-axis, which is parallel to the electron beam). The tensile stress axis is along the sample length, which is the y-axis for XY samples and the z-axis for XZ samples. The two samples grown in the Arcam[®] S12 unit have orientations along the XY and XZ, see Figures 3.1 and 3.2.

“XY” Sample

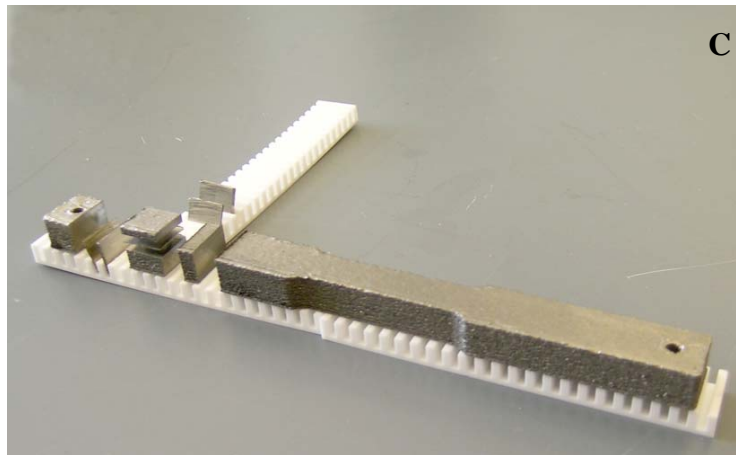
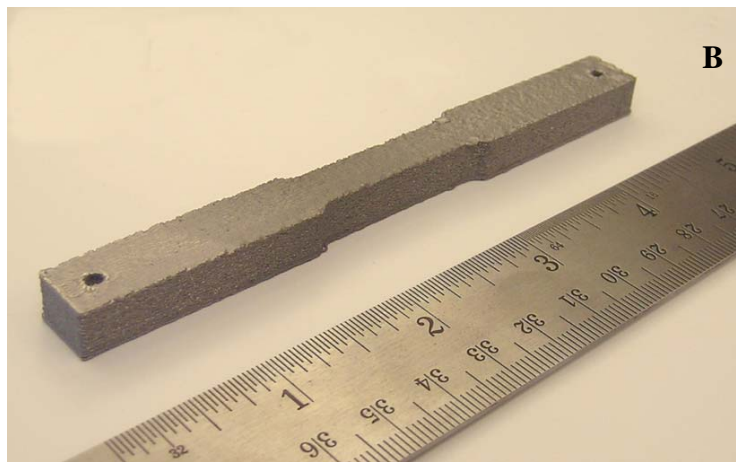
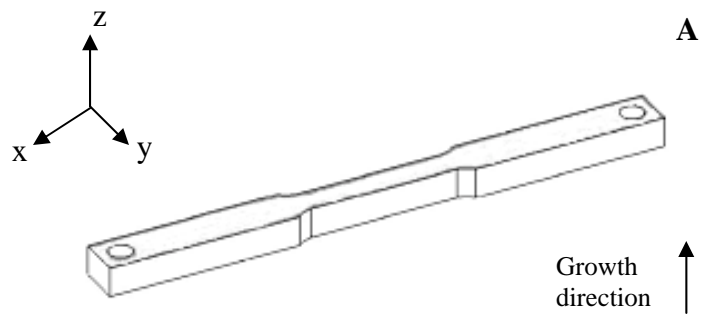


Figure 3.1. XY sample grown in the Arcam S12. A) Sample schematic. B) Actual specimen. C) Sectioned specimen.

“XZ” Sample

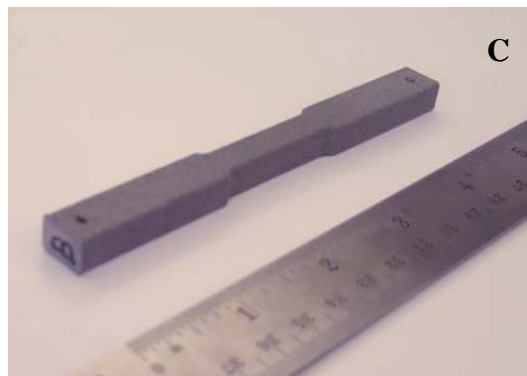
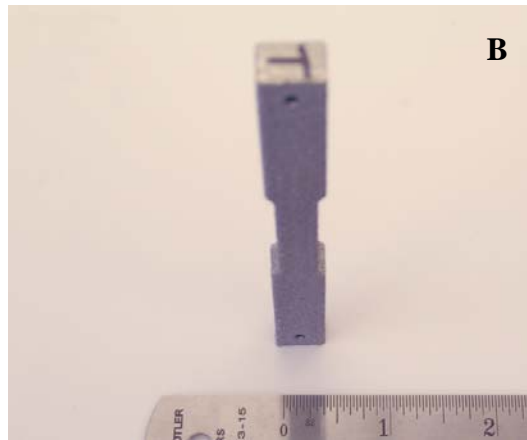
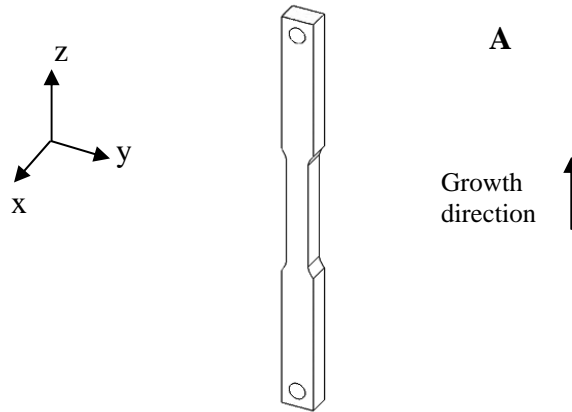


Figure 3.2. XZ sample grown in the Arcam S12. A) Sample schematic. B) Top view of actual specimen. C) Bottom / side view of actual sample.

The XY bar original length x width x height dimensions are 121.6 mm x 11.8 mm x 8.03 mm with a center gage section width of 8.55 mm. The XZ bar original dimensions are 121.2 mm x 12.2 mm x 8.22 mm with a center width of 8.70 mm.

The sample produced by the Arcam[®] A2 machine was a cylindrically-shaped tensile bar grown in horizontal fashion as shown in Figure 3.3. This sample will be referred to as HC to designate a horizontal cylinder. This orientation will be considered equivalent to that of the XY sample.

To provide thorough microstructural studies the various surface planes of the samples were examined as shown in Figure 3.4. The surface planes that are shaded are identified in the sample schematics of Figure 3.4. The z-axis is always referred to as the growth axis, which is not equivalent to the tensile stress axis for all sample geometries.

“HC” Sample

(Horizontal Cylinder)

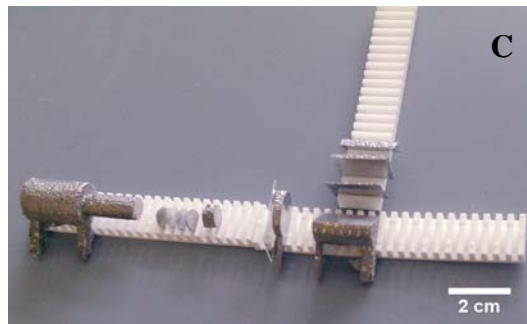
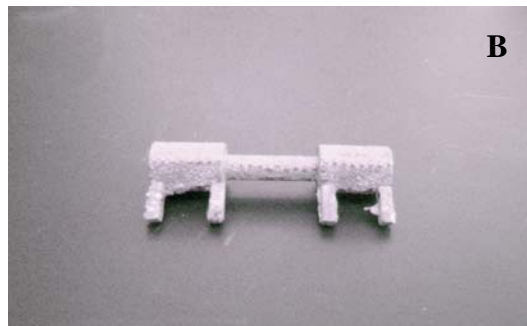
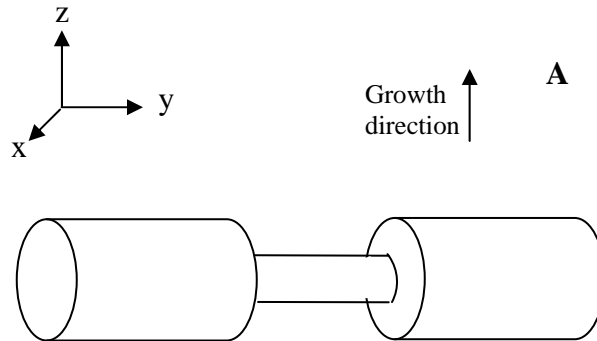


Figure 3.3. Horizontal Cylinder (HC) sample grown in the Arcam A2.

A) Sample schematic. B) Actual specimen. C) Sectioned specimen.

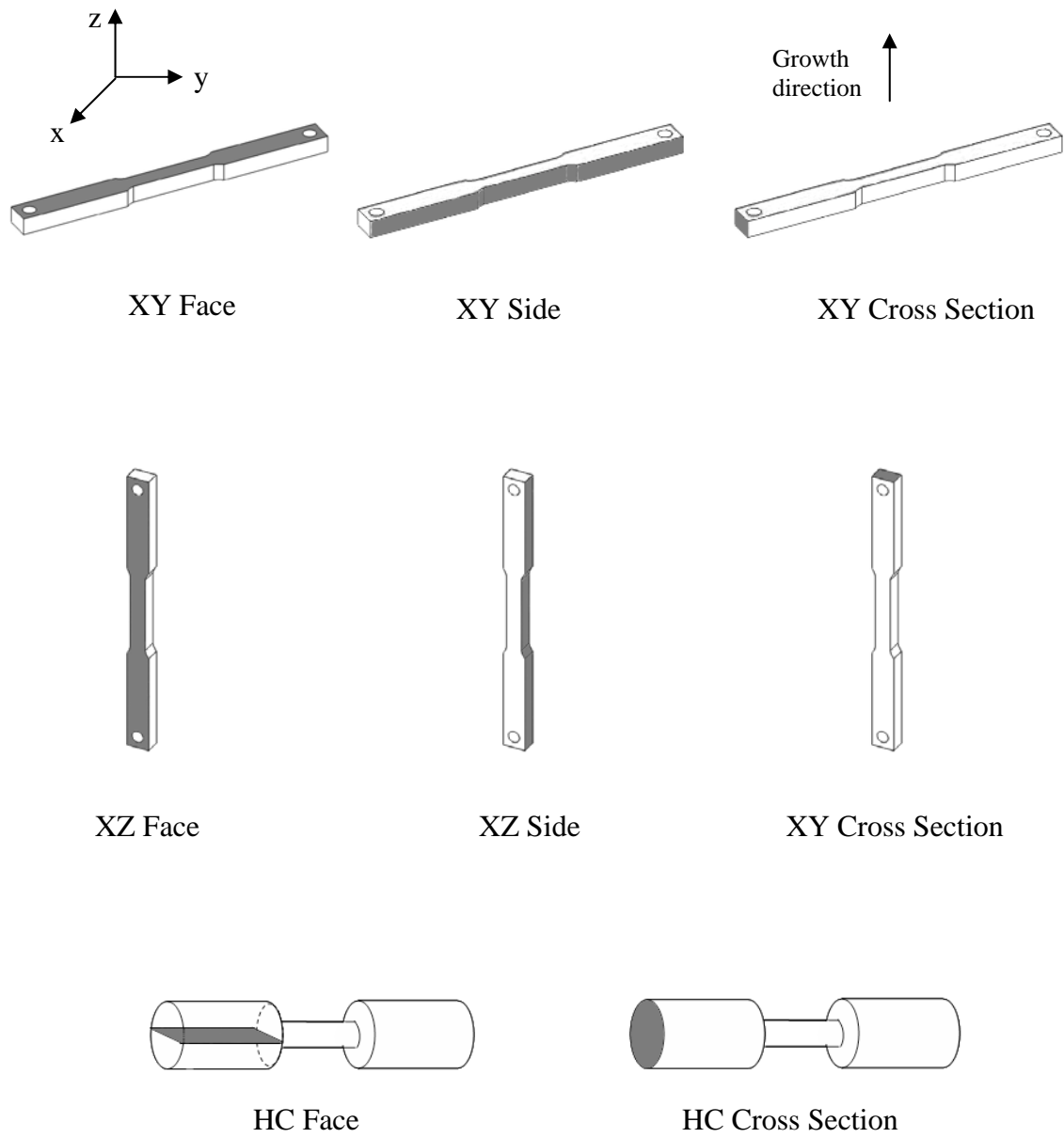


Figure 3.4. XY, XZ and HC sample geometries. Surface planes investigated in this study are designated by the shaded area and labeled with identification nomenclature.

The as-grown tensile specimens were sectioned for characterization using a Leco V-50 low-speed diamond blade saw and Leco cutting fluid. Samples were cut from the bulk both parallel and perpendicular to the growth direction. The nomenclature adopted for this study consists of face, side and cross section orientations as shown in Figures 3.3 and 3.4.

A Ti-6Al-4V forged helicopter engine turbine blade (Figure 3.5) that was retired from service was also investigated using optical and scanning electron microscopy for comparison of what is considered an ideal representative microstructure for aviation applications. A small section shown in Figure 3.5 was cut by hand using a hacksaw and prepared for optical microscopy and SEM by the same methods described for the Arcam[®] samples in the following section.

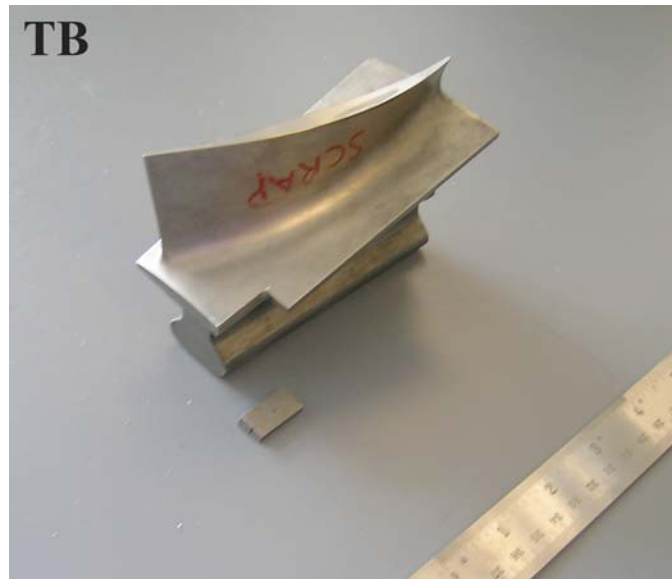


Figure 3.5. Forged Ti-6Al-4V helicopter turbine blade (TB).

3.2. Sample Preparation for Microstructure Analyses

3.2.1. Optical Microscopy Sample Preparation

For observation of microstructural features by optical microscopy each orientation sample was mounted in Buehler thermosetting bulk molding compound. Samples were metallographically polished through a series of closed-grit silicon carbide grinding/polishing paper and aluminum oxide water suspension slurry polishing media. The abrasive grit sequence used to polish the optical microscopy and SEM samples was 180, 240, 320, 400, 600, 800, 1000, and 1200 carried out on a South Bay Technologies Model 900 polishing wheel using water as the lubricant. Final polishing was achieved by using 1.0 μm aluminum oxide followed by 0.05 μm aluminum oxide polishing media. Samples were etched in Kroll's reagent (5% hydrofluoric acid, 10% nitric acid, 85% H_2O).

3.2.1. Scanning Electron Microscopy Sample Preparation

The samples that were prepared for optical microscopy were also used for the scanning electron microscopy portion of this study. To eliminate sample charging in the SEM silver paint was applied from the edge of the sample surface to the bottom of the sample where contact was made to the grounded SEM mounting stub.

The PREP powder was prepared for SEM imaging by applying the powder to a stub with carbon tape. Excess powder was removed by gently dusting with dry nitrogen.

Samples used for exterior morphology evaluation were cut from the original XY, XZ, and HC tensile bars using the Leco V-50 low speed saw with a diamond blade. These sections were cleaned in acetone and given a final methanol rinse.

3.2.3. Transmission Electron Microscopy Sample Preparation

3.2.3.1. Electropolishing

Electropolishing is a TEM specimen preparation technique that can uniformly remove material from a metal without introducing plastic deformation to the sample. Differential polishing rates (effectively etching) of one phase versus another phase or at grain boundaries is a common but undesirable result of electropolishing multiphase microstructures.

Conductive samples are immersed in an electrolytic solution, which is typically an acid or a mixture of an acid and an organic solvent. The premise of electropolishing lies in achieving equal resistance across the sample surface through the generation and flow of a viscous electrolytic fluid at the sample surface with an applied voltage such that the material is polished rather than etched or pitted [18, 19]. Successful sample preparation requires operation within the polishing regime of the voltage and current curve in Figure 3.6 below.

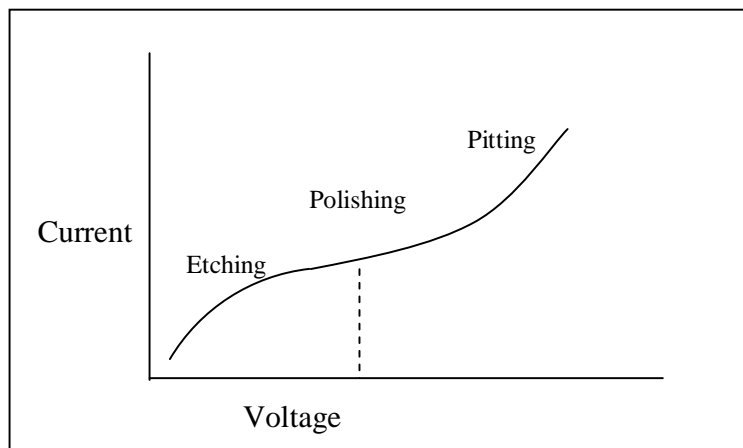


Figure 3.6. Illustration of active regimes associated with electropolishing for current as a function of voltage.

Published recommendations for TEM foil preparation of Ti-6Al-4V by electropolishing were found to be ineffective on the alloy used in this study when followed as prescribed. The parameters described by Kestel [18] which uses 13% HCl and methanol as the electrolytic solution produced undesirable titanium hydride platelets between phases. The parameters described by Blackburn and Williams [20] were successfully used after some modifications in the applied voltage and resultant current.

TEM samples were produced from sections adjacent to those surfaces used for optical and scanning electron microscopy. During the preparation of electron transparent electropolished samples, care was taken to ensure artifacts were not introduced from the preparation process. Sections ranging from 0.3 to 0.7 mm thick were taken from the bulk material using a slow speed diamond saw. Orientations of interest were either parallel or perpendicular to the growth direction. Three millimeter diameter discs were cut from the sections by either a South Bay Technologies Model 350 abrasive slurry drill or from an Eckert mechanical hole punch device.

The 3mm discs appropriate for TEM samples were mounted with South Bay technologies sample mounting wax to stainless stubs that are used with a Gatan Model 623 Disc Grinder. The samples were mechanically thinned to approximately 25 μm by the same abrasive sequence described for the optical and SEM samples and using a South Bay Technologies Model 910 polishing wheel. Each surface of the foil was polished with the 1 μm aluminum oxide slurry prior to electropolishing.

Electron transparency of the pre-thinned foils was achieved using a Struers Tenupol-2 electropolishing unit. The electrolytic solution used was 59% methanol, 35% butanol, and 6% perchloric acid. The conditions for successful polishing attempts are listed in Table 3.1

Table 3.1. Electropolishing conditions for Ti-6Al-4V.

Alloy	Electrolytic Solution	T (°C)	V (volts)	I (mA)	Jet Speed	time (s)
Ti-6Al-4V	59% methanol 35% butanol 6% perchloric acid	-50	11	10 - 17	max (10)	30 - 90

3.2.3.2. Focused Ion Beam

Focused ion beam (FIB) technology has greatly expanded the range of materials that can be examined by TEM or STEM because of its ability to produce electron transparent sections from a selected area of virtually any material or part. Similar in construction to an SEM, an electron beam allows the user to image and manipulate a sample while a gallium ion beam mills away material to electron transparency. The sample can then be lifted out of the part and attached to a TEM sample grid.

A Quanta 200 3D Focused Ion Beam was used to prepare a TEM sample from a Face orientation cross section of the XZ sample. The FIB was operated at 30 keV with a gallium ion beam. Various Ga ion beam currents are used during the successive steps for producing a TEM sample. Mass removal of the sample around the area of interest is performed at 20 nA beam current. A beam current of 3 nA is used for the initial polishing of the sample surface that will be exposed to the incident electron beam of a TEM, while the sample is still attached to the bulk material. The lift-out probe is attached to the sample at 100 pA beam

current. The sample is cut away from the bulk material at 1 nA beam current. Once the FIB sample is attached to the grid on which it will reside, final polishing of the sample is achieved using the sequence of 1nA, 300pA, and 100pA beam currents.

The FIB has a scanning electron beam in addition to the gallium ion beam. Both ion and electron imaging of a sample in progress is possible. Samples can also be imaged in the FIB by detecting the gallium ions or secondary electrons.

3.3. Optical Microscopy

Imaging of the microstructures in various polished and etched sample orientations were performed on Zeiss MAT 40 Axiovert and Zeiss stereo optical microscopes. Jenoptik ProgRes 10 cameras were used for digital image acquisition.

3.4. Scanning Electron Microscopy

In scanning electron microscopy (SEM) an image is constructed as the signals generated from a rastered focused incident electron beam interact with the sample to produce signals such as secondary electrons, backscattered electrons, and characteristic x-rays which are collected by various detectors and then processed. The scanning electron microscope provides topographical information from the surfaces of organic and inorganic materials. The electron beam emitted from a source at energies generally up to 30KV is directed downward through a vacuum column and focused into a probe that is scanned across a sample. Contrast from atomic number can also be observed. The interaction volume for beam accelerating

voltages in the neighborhood of 20 to 30 keV can be on the order of a few cubic microns, especially for materials of low atomic number and/or low density.

Several scanning electron microscopes were utilized in the characterization of the component exterior morphology, microstructure, and interior fabrication defects. A Hitachi 3200N SEM was used with an accelerating voltage of 20 KV to examine the polished and etched samples of orientations XY side, face and cross-section; XZ side, face, and cross section; and HC face and cross section. The Hitachi 3200N and an Amray 1810 were use at an accelerating voltage of 5 kV for imaging the PREP powder. A JEOL 5900LV operating at 20 KV was used to image the exterior surface morphology of the three types of tensile specimens. A Hitachi S-5500 ultra-high resolution SEM was used at 30KV to investigate the XZ face TEM sample that was prepared via FIB.

3.5. Transmission Electron Microscopy

Conventional transmission electron microscopy (TEM) produces a direct image of the interior microstructure of a thin sample. In this technique a parallel incident electron beam, typically between 120 keV and 300 keV, interacts with and transmits through the sample forming a 2D projected image of a 3D microstructure onto a fluorescent screen, a charge coupled device (CCD) camera, or directly to exposed film located beneath the sample. TEM is known for extremely high resolution (0.1 nm), however sample preparation is usually quite demanding and time consuming as the sample must be meticulously thinned to achieve electron transparency [21] without introducing artifacts. The types and sizes of TEM samples are limited compared to those samples that can be imaged and analyzed in an SEM.

Information available from TEM analyses includes phase morphology, crystal type and orientation, and imaging of defects.

Conventional TEM was carried out for XY side, XY cross-section, XZ face, HC cross section, and HC face on a JEOL 2000FX with a LaB₆ electron source operating at 200 KV. A Gatan CCD camera was used for digital image capture of bright field and diffraction pattern images.

3.6. Scanning Transmission Electron Microscopy

Scanning transmission electron microscopy (STEM) combines elements from conventional TEM and SEM to appropriately handle imaging and microanalysis of thin samples. In this investigation, an SEM with STEM capabilities was used. In STEM the incident beam is focused to a small diameter and rastered across the sample. Differences in intensity are measured point-by-point, but the signals generated by the beam are transmitted through the sample and are collected below the sample.

As the incident beam interacts with a sample, scattering of the incident electrons results in beam broadening. For bulk samples, beam broadening can be in the range of 1000 nm whereas broadening of the electron beam passing through thin film samples is in the 1 to 10 nm range [22]. Resolution in STEM mode is governed by the probe size, which is a function of beam broadening b as defined by the equation:

$$b = b_0 + 625 \times 107 \times \frac{Z}{E_0} \times \left(\frac{\rho}{A} \right)^{1/2} \times t^{3/2} \quad (\text{Eq. 3.1})$$

where b_0 is the incident focused electron beam probe diameter in nm; E_0 is the incident beam voltage; Z is the atomic number; ρ is the specimen density in g/cm^3 ; A is the atomic weight, and t is the sample thickness $\times 10$ nm [23]. Image resolution and x-ray microanalysis can be achieved on the nanometer level as the spatial resolution is increased due to the absence of large beam spreading as it passes through a thin specimen.

The Hitachi S-5500 STEM was operated in transmission mode at 30 KV while examining the XZ face of a FIB-prepared sample. A Bruker AXS elemental dispersive x-ray spectroscopy (EDS) system was used on the S-5500 for localized chemical information. EDS data was taken in line and elemental mapping modes.

3.7. Energy Dispersive X-Ray Spectroscopy

Inner shell ionization occurs as the incident electron beam interacts with a tightly bound inner shell electron. The de-excitation that follows an electron transition causes emission of an x-ray that is characteristic of the element under electron bombardment. These characteristic x-rays can be detected and used for qualitative and quantitative elemental analysis.

In what is referred to as energy dispersive x-ray spectroscopy (EDS), an energy dispersive spectrometer collects x-ray photons emitted with characteristic energies from a sample and converts photon energy into an electrical signal through a solid-state Si(Li) crystal detector. The lithium-drifted Si(Li) detector absorbs x-ray photons and ejects photoelectrons which are amplified and processed to provide a final histogram of the intensity as a function of characteristic x-ray photon energy.

3.8. Grain Size Determination

Prior beta grain size was approximated per ASTM E 112 by counting the intercepts of a microstructural feature by several lines of known length which were re randomly drawn on optical micrographs. Four random lines of known length were drawn on each of five different images. The number of intersections between grain boundaries and lines were counted to obtain N_L , the number of intercepts per unit length of test line. The grain size G is determined by using the following relation.

$$G = -3.2877 + 6.6439 \log_{10} N_L \quad (\text{Eq. 3.2})$$

3.9. Volume Fraction Determination

The volume fractions of α and β phases present are estimated using a systematic manual point count per ASTM E 562-08. A regular pattern of intersecting lines is superimposed over the optical micrographs. The *Grid Overlay* plug-in in Image J is used to apply an evenly spaced point grid directly to the optical microscope digital images. Points that fall on boundary lines and other questionable intersections are given a value of one half to eliminate bias. The number of points that fall on the minor phase is counted for each image which is defined as P_i . Points that fall on the phase of interest are given a value of one. P_T is the total number of points used on the test grid. $\overline{P_p}$ is the arithmetic average defined by Eq. 3.3 where n is the number of images used to estimate the volume fraction.

$$\overline{P_p} = \frac{1}{n} \sum_{i=1}^n P_p(i) \quad (\text{Eq. 3.3})$$

$P_p(i)$ is the percentage of grid points that fall on the phase of interest defined in Eq. 3.4.

$$P_p(i) = \frac{P_i}{P_T} \times 100 \quad (\text{Eq. 3.4})$$

The volume percentage of a phase is thus given by Eq. 3.5.

$$V_v = \overline{P_p} \pm 95\% CI \quad (\text{Eq. 3.5})$$

95% CI is the confidence interval that is given by Eq. 3.6.

$$95\% CI = t \left(\frac{s}{\sqrt{n}} \right) \quad (\text{Eq. 3.6})$$

The variable t is a multiplier that is referenced from Table 1 in ASTM 562-08 and is used to determine the 95% CI and is related to the number of images used for estimating the volume fraction. An estimate of the standard deviation (s) is calculated by Equation 3.7.

$$s = \left[\frac{1}{n-1} \sum_{i=1}^n [P_p(i) - \overline{P_p}]^2 \right]^{1/2} \quad (\text{Eq. 3.7})$$

The relative accuracy (RA) estimate is obtained by Eq. 3.8.

$$\% RA = \frac{95\% CI}{\overline{P_p}} \times 100 \quad (\text{Eq. 3.8})$$

4. RESULTS AND DISCUSSION

This chapter begins with analysis of the exterior surface morphology of as-built Arcam S12 and A2 components using optical and scanning electron microscopy data. Comparisons are made between the forged turbine blade material and the particular three Arcam built samples in the areas of grain size and morphology and, α and β phase morphology and volume fraction. Quantification of the percentages of the α and β phases were determined from optical and SEM micrographs. In the samples polished and etched with Kroll's reagent, alpha was white in optical micrographs and black in SEM micrographs. The inverse is true for the beta phase. Grain size of the forged turbine blade and planar cross sections of Arcam components normal to the incident electron (melting) beam was estimated by counting the number of intersections of grain boundaries with a line of known length applied to optical micrographs per ASTM E 112. ASTM E 562-08 is used to describe the estimation of volume fractions of α and β as described in Experimental Procedure, Section 3.8.

The next portion of this chapter focuses on the microstructures of as-built Arcam components are investigated with optical microscopy, SEM and TEM, FIB and STEM were used for sectioning and analyses, respectively, of the XZ Face sample. SEM was used to investigate the intrinsic porosity of the as-built Arcam components.

The final section of this chapter presents TEM sample preparation results from electropolishing and focused ion beam techniques. Obstacles involved with electropolishing

and the corrective measures for producing successful electron transparent foils from as-built Arcam samples are addressed.

4.1. Exterior Morphology of Arcam Components

The exterior surface morphologies of the near-net shape components produced from the Arcam S12 and A2 EBM machines are presented in this section. Results for the as-built XY and XZ samples precede the horizontal cylinder (HC) sample.

4.1.1. Arcam S12 XY Component

The exterior surfaces of the as-built components produced by the Arcam EBM process shown in this section were cleaned with a wire brush to removed excess PREP powder that surrounded the component in the build tank during component growth but no further sample preparation was performed.

The Arcam electron beam probe diameter was approximately 100 μm and can be as large as 300 μm when the probe is slightly defocused. In Figure 4.1, the Arcam electron beam raster pattern is visible on the top surface of the specimen and the width of the melt pool ranges from 240 to 430 μm which is consistent with the probe size and 200 to 300 micron triangular swirl pattern of the Arcam electron beam.

The SEM view is normal to the XY Face, which is parallel to the Arcam electron beam. Some unmelted PREP powder is visible along the left edge, which is the XY Side surface. Although irregularities on the exterior morphologies are evident along the edge of the sample where the Side and Face surfaces meet in Figure 4.1 and subsequent SEM

micrographs of the surfaces of as-built Arcam components, these images show that the Arcam S12 EBM machine produces samples very close to their intended shapes.

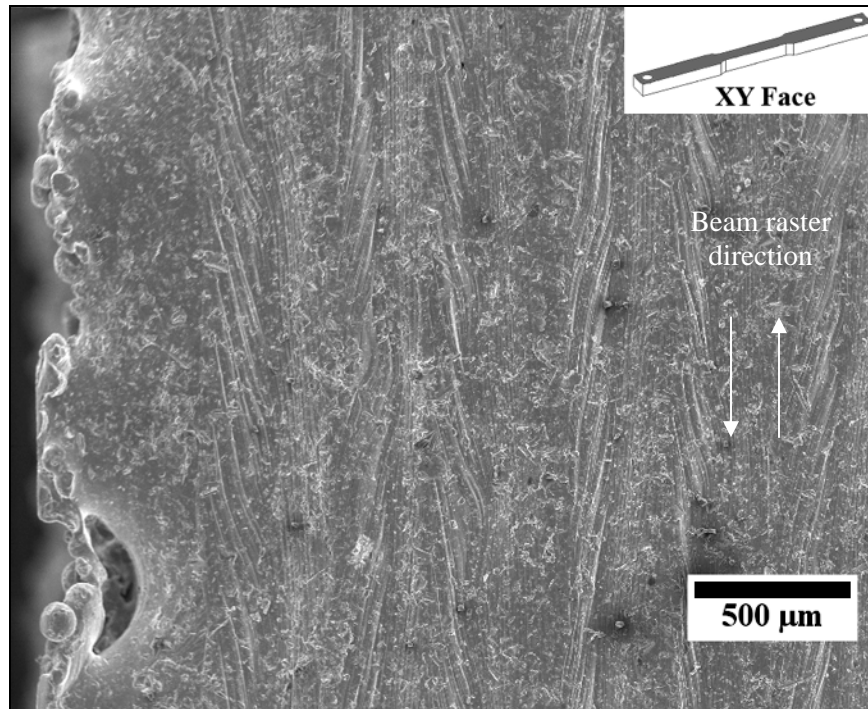


Figure 4.1. SEM image of XY Face exterior surface. Growth direction and incident Arcam electron beam are normal to page.

The exterior side surface of the as-built XY sample is shown in the SEM micrograph in Figure 4.2. As expected, surface topography is not as uniform or smooth, as is observed on the XY Face surface topography shown in Figure 4.1. Spherical powder particles from the surrounding area of the build tank are sintered onto the exterior surface of the sides of a component. The bottom of the sample in Figure 4.2 is the part of the component that is in contact with the build plate. Consequently a final finishing, such as sandblasting, machining,

and polishing steps would be required to produce a smooth surface with no unmelted powder particles.

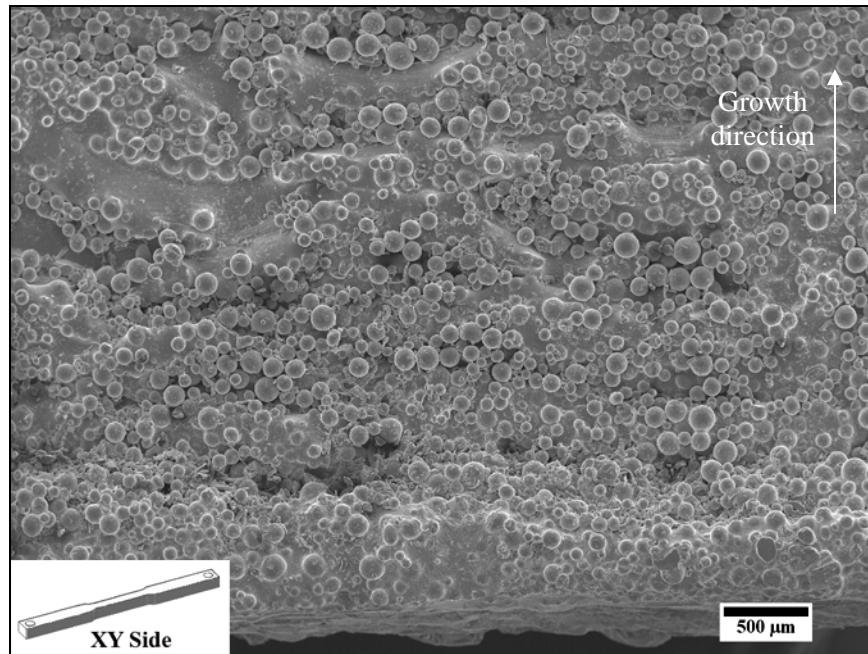


Figure 4.2. SEM image of XY Side exterior surface.

4.1.2. Arcam S12 XZ Component

The XZ Face surface of the tensile bar at the gage length area where its cross section is reduced is featured below in Figure 4.3. Distinct ledges are visible that are the result of additive deposition layers. The tensile bar is imaged on its side and the growth direction of the component is from right to left. The layers visible in this image are the build steps and are spaced approximately 360 to 410 microns apart. Careful examination of the image reveals that the incomplete melting of the powder creates notches between build layers and likely will result in increased porosity in the midline between build layers. Since the sample is

surrounded by the alloy powder as a component is being built, some of the powder particles fuse to the sample from the residual heat available in the component.

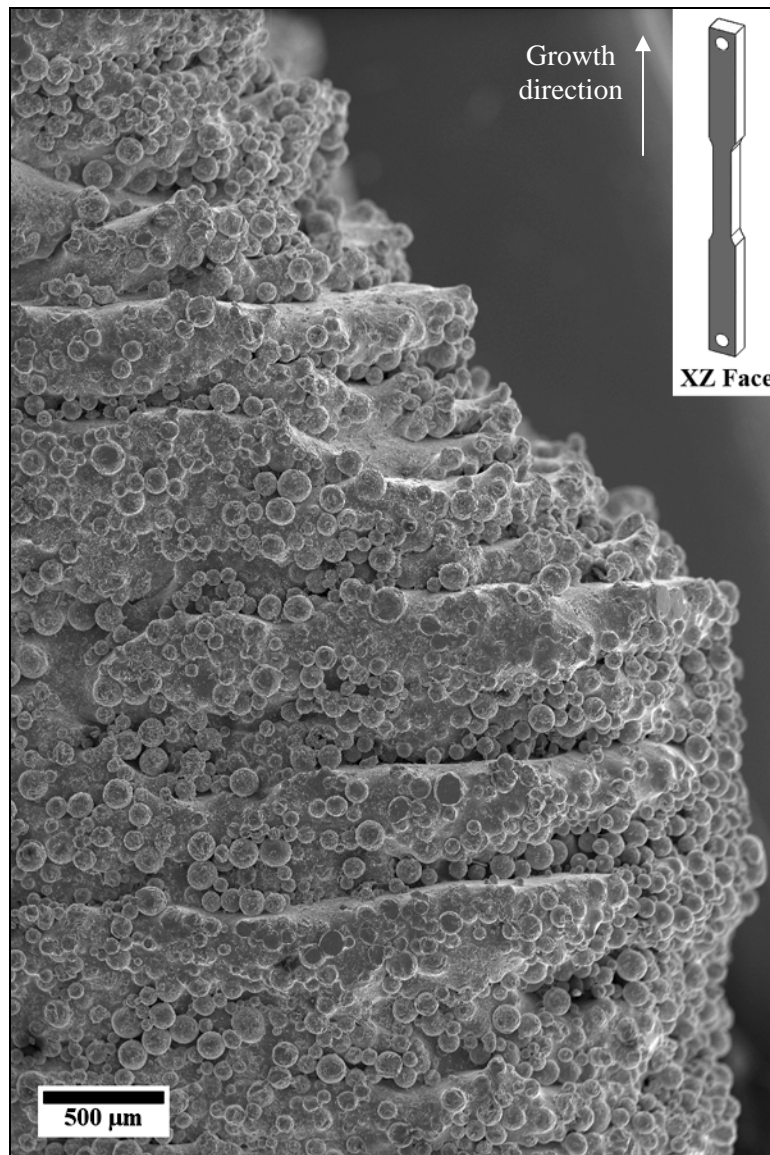


Figure 4.3. SEM image of XZ Face exterior surface.

Figure 4.4 is a higher magnification SEM micrograph of the XZ sample in Figure 4.3. Individual deposition layers can be seen in addition to the surface roughness consisting of

PREP powder spheres attached to the exterior. The sample had been handled and cleaned with a wire brush upon removal of the Arcam S12 EBM machine.

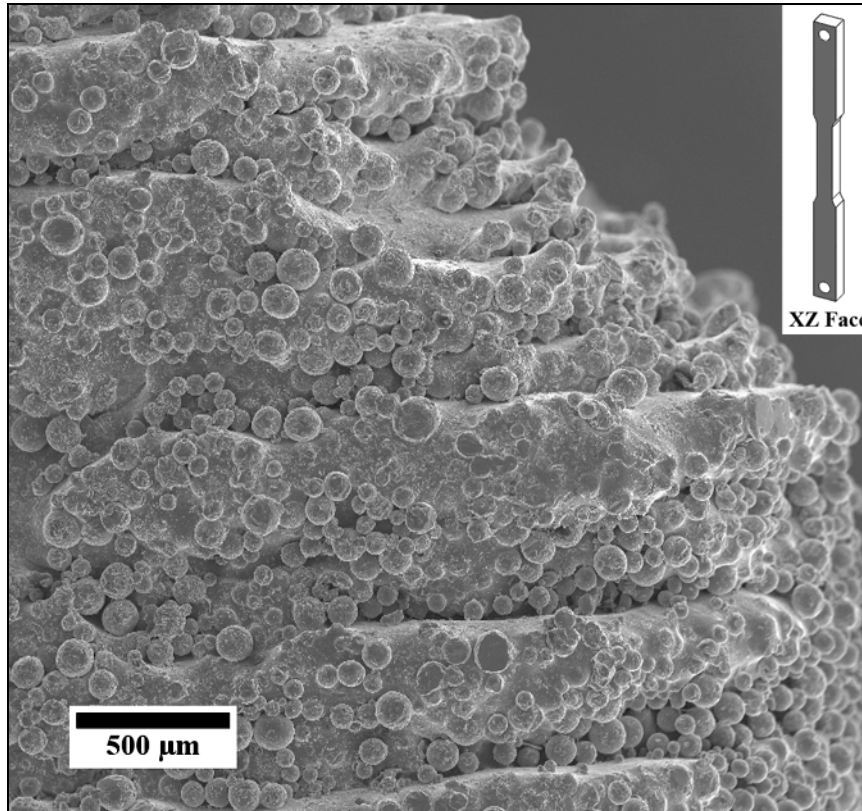


Figure 4.4. SEM image of XZ Face exterior surface featured in Figure 4.3.

Figure 4.5 shows the polished and etched cross section of the XZ Face plane as mounted in the thermoset resin used for the polishing and etching procedure described in Experimental Procedure. Of the PREP powder spheres remaining on the outer surface from the build process as seen in the optical micrograph of Figure 4.5, some are loosely attached which can be seen embedded in the black thermosetting resin on the left side of the image

and are not in contact with the component. Some of the spheres are clearly partially sintered to the component as seen in Figure 4.5.

Deposition layer heights measured from Figures 4.3 and 4.4 are well above the 100 μm layer height that is controlled by the Arcam EBM machine. This suggests that the machine does not actually control component growth in 100 μm layers as indicated by the build data that is logged by the software associated with the Arcam EBM machines.



Figure 4.5. Optical micrograph of XZ Face mounted, polished and etched.

4.1.2. Arcam A2 Horizontal Cylinder Component

The exterior surface of the horizontal cylinder (HC) grown in the Arcam A2 EBM machine is shown in the SEM micrographs in Figures 4.6 and 4.7 of the HC Face surface. Figure 4.6 was captured at top dead center of the cylinder, normal to the Arcam incident electron beam and the part growth direction. The width of the bead from the movement of

the melt pool is approximately 150 μm . The width of the melt pool in this region is 2 mm. The top surface of the sample has some remnants of the PREP powder spheres that are partially sintered to the surface at the melt pool edge.

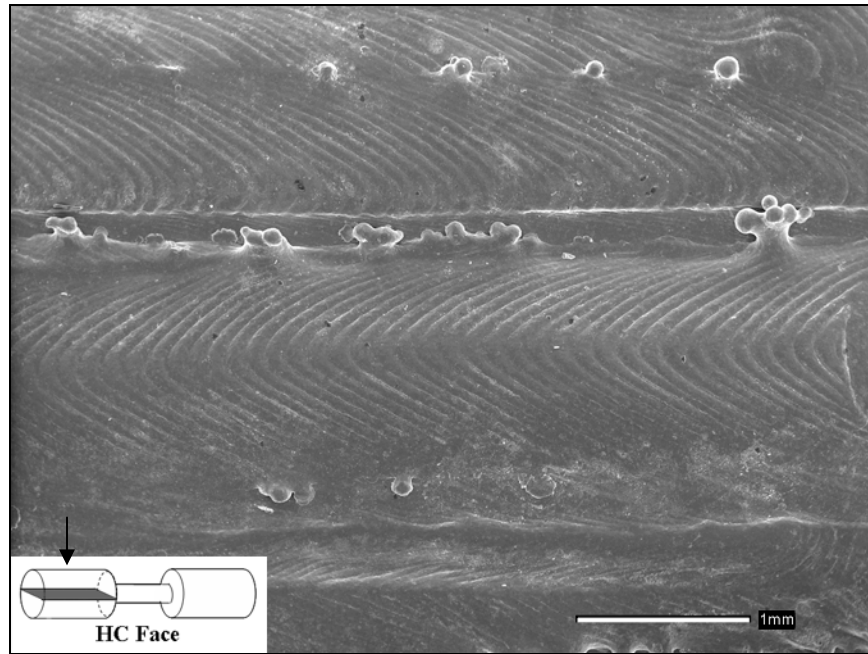


Figure 4.6. SEM image of HC Face exterior surface, top dead center.

The surface roughness of the HC component increases away from surfaces that are not perpendicular to the incident Arcam electron beam. Figure 4.7 is an SEM micrograph that shows the exterior of the curved surface of the cylinder away from the centerline in Figure 4.6. PREP powder spheres fused with the melted material are discernable along the edges of the layers, which are highly irregular, topographically.

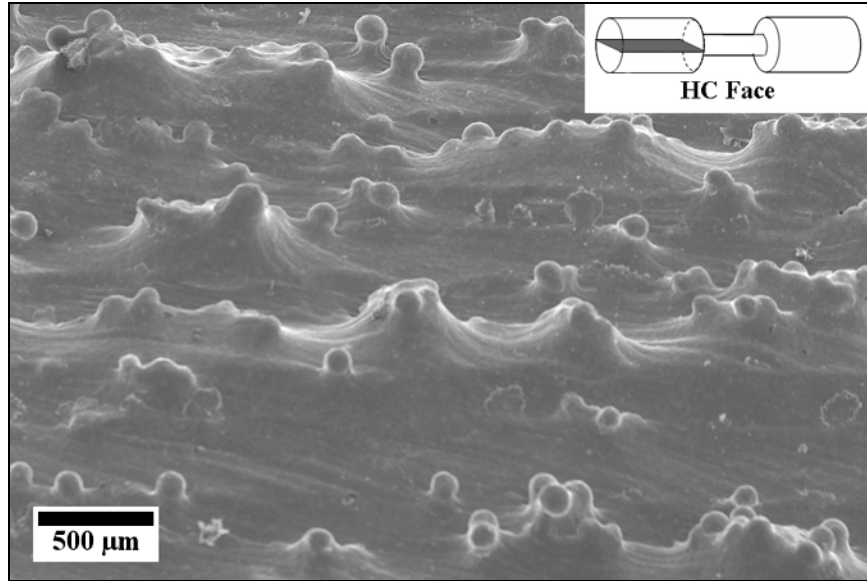


Figure 4.7. SEM image of HC Face exterior on a curved surface.

4.2. Microstructure of a Forged Turbine Blade

4.2.1. Grain Size and Morphology

The optical micrograph in Figure 4.8 is a polished and etched forged Ti-6Al-4V helicopter engine turbine blade that has been retired from service and is representative of the bulk material. The grain structure is equiaxed and represents an ideal grain size and shape for a many Ti-6Al-4V aircraft components. The forging process followed by a recrystallization anneal, typically 4 hours at 925°C [13], provide the thermo-mechanical energy required to obtain the equiaxed microstructure seen in Figure 4.8.

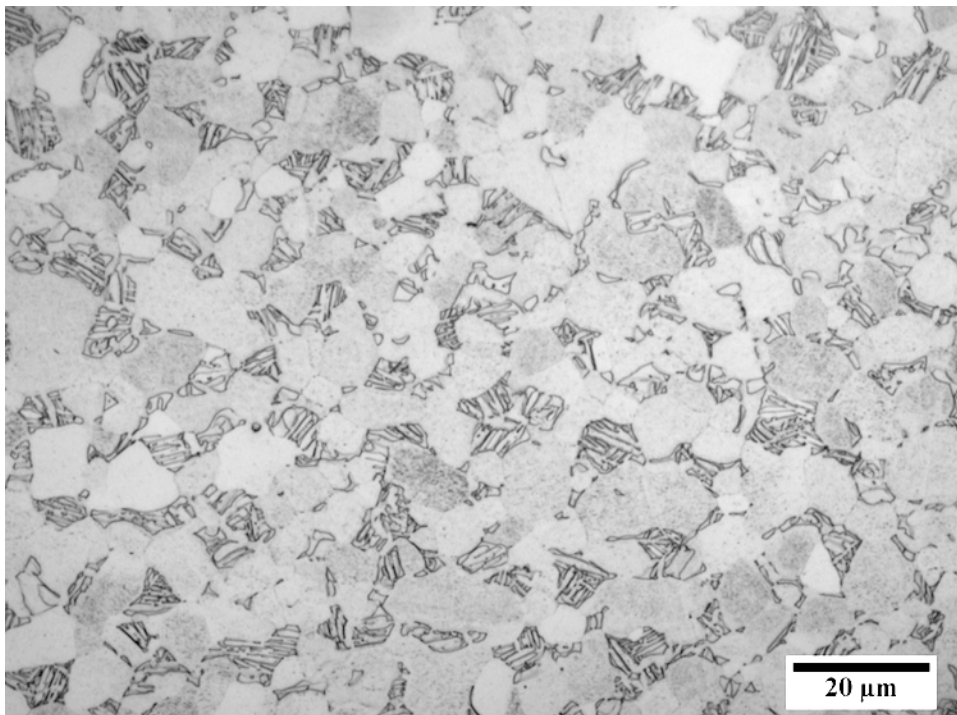


Figure 4.8. Optical micrograph of a Ti-6Al-4V forged turbine blade.

Grain size is estimated by using the ASTM E 112 intercept method described in Section 3.8 of Experimental Procedure. The number of intercepts per unit length of test line is for the forged turbine blade is 172.55 which gives a grain size of $G = 12$ when applied to Eq. 3.2. This correlates to an average grain size of $6.7 \mu\text{m}$.

4.2.2. Description of $\alpha + \beta$ Phase Morphology

Alpha phase appears light and beta phase appears dark in the optical micrograph in Figure 4.8. The microstructure of this specimen is equiaxed alpha grains in transformed beta matrix (intergranular), which contain coarse acicular α phase. Figure 4.9 is an SEM micrograph of the same sample in Figure 4.8. Alpha phase appears dark as it is etched preferentially over the beta phase, which appears lighter in contrast in SEM micrographs due to topographical difference.

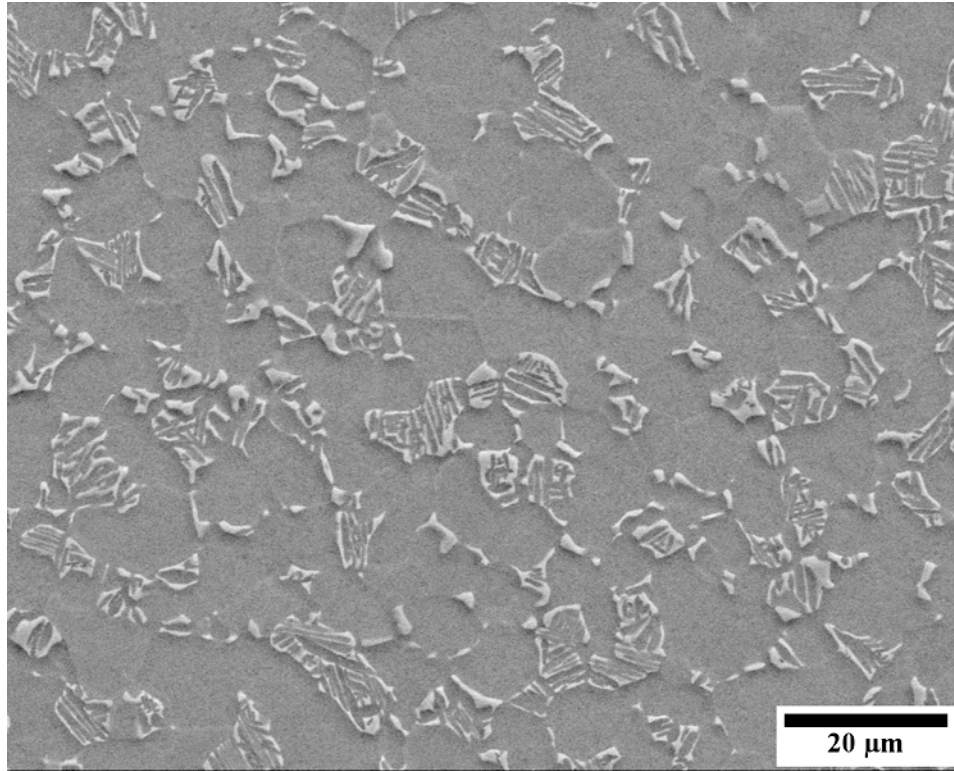


Figure 4.9. SEM micrograph of Ti-6Al-4V forged turbine blade.

4.2.3. Volume Fraction of β Phase

The volume fractions of β is measured using by a systematic point count method along the ASTM E 562-08 standard described in Section 3.9 of Experimental procedure. The number of points that fall on the minor phase are recorded. Five optical micrographs were used to calculate the volume fractions of each phase present. The arithmetic average for the volume fraction of beta is 27.4% with a standard deviation estimate of 5.1. The volume fraction of the beta phase is $27.4\% \pm 6.3$ (95% confidence interval). The relative accuracy for this measurement is 23%, which is a measure of the statistical precision.

Table 4.1. Volume fraction of beta phase for forged turbine blade sample.

Component Type	Volume Fraction of Beta Phase (%)	Relative Accuracy (%)
Forged Turbine Blade	27.4 ± 6.3	23

4.3. Microstructure of Arcam S12-Produced Components

4.3.1. Grain Size and Morphology

Figure 4.10 shows a cross section of the XY sample that was grown in the Arcam S12 EBM machine. This sample oriented in the XY Cross Section view was mounted in a thermosetting bulk molding compound and, after grinding and polishing, was etched with Kroll's reagent. The columnar structure observed here is oriented parallel to the rastered incident electron beam. These grain-like structures extend several millimeters, which in the case of the XY sample is the height of the sample itself. The incident electron beam of the Arcam EBM process was rastered in the x and y directions. The bottom of the sample in this image was in contact with the build plate during component fabrication. Macroscopic voids, on the order of tens of microns in diameter, appear as white spots from reflected light in this image. Such voids were a commonly observed part of the microstructure.

Bands running horizontally are visible resulting from the additive process of layers being melted sequentially. Silver paint (upper right corner of Figure 4.10) was applied to make a continuous conductive path from the polished surface of the edge of the alloy/bakelite interface to the SEM sample stub as seen in Figures 4.10. The accuracy of the Arcam S12 EBM machine of producing solid objects can be seen by observing only slight irregularity in the rectangular cross section at the interface of the sample edge and sample mounting media.

The columnar grain structure observed here extended several millimeters long in the vertical direction, parallel to the Arcam electron beam. These grain structures are quite

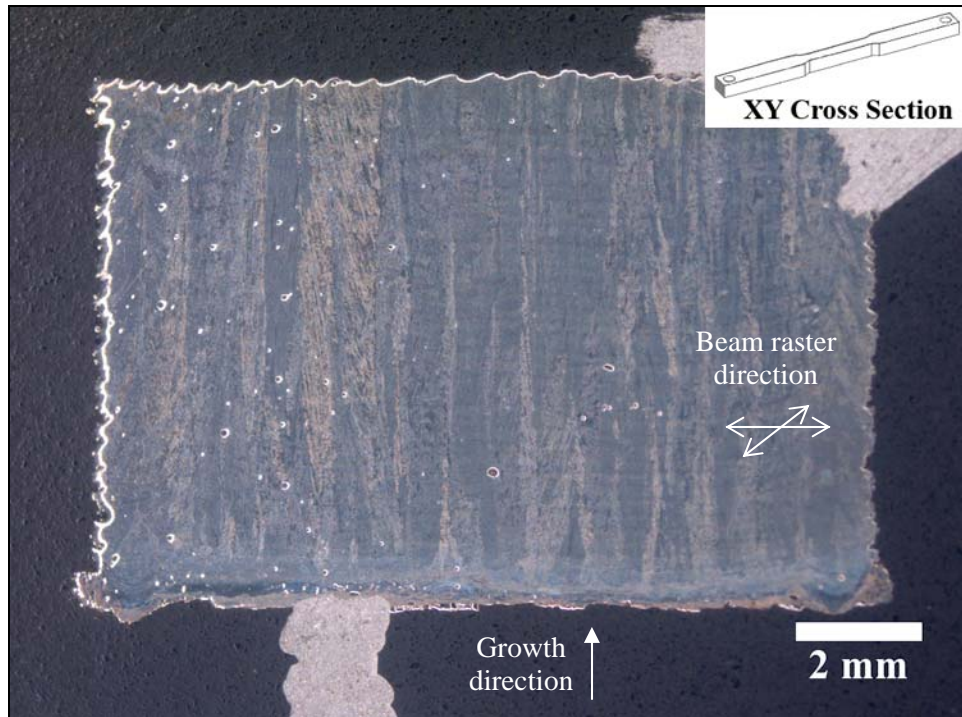


Figure 4.10. Low magnification optical image of mounted XY Cross Section samples as used for optical and scanning electron microscopy.

dissimilar to the equiaxed grains seen in the forged turbine blade in the preceding section which are a result of being mechanically processed below the beta transus temperature. As was observed in the Ti-6Al-4V deposition via DMD study by Dinda et al., although heat loss occurs through the surrounding atmosphere (vacuum in the Arcam systems) and the substrate, the columnar grain growth is a result of rapid cooling of the melt pool through the substrate as opposed to heat loss through convection and radiation [1]. Once nucleated, the columnar grains continue to grow parallel to the electron beam with each successive deposition layer.

Figure 4.10 is the XZ sample mounted such that the Face plane is in cross section. As was seen in the XY Cross Section plane of Figure 4.10, horizontal bands are present along with vertical columnar grain structure. Slight irregularity of the surface of the XZ component is apparent on the sides of the metal/bakelite interface on the left and right sides of Figure 4.11, which represent the front and rear surfaces of the XZ tensile specimen. In the XZ orientation, the tensile axis is parallel to the growth direction, and therefore parallel to the columnar grains. According to data reported by Bass [6], there appears to be no significant difference in tensile strength between the XY and XZ samples tested.

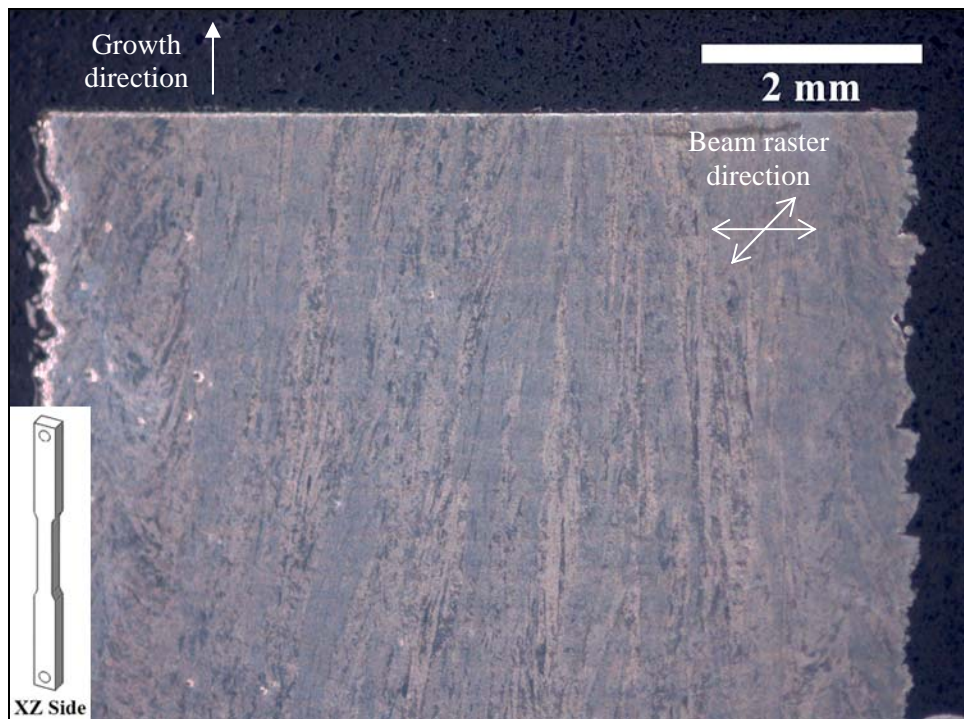


Figure 4.11. Low magnification optical images of mounted XZ Side sample as used for optical and scanning electron microscopy.

Figures 4.12 and 4.13 are XY Face plane and XZ Cross Section plane respectively, which are both normal to the incident electron beam. As in the previous two images, these samples were mounted in a thermosetting bulk molding compound and, after grinding and polishing, were etched with Kroll's reagent. Silver paint used for the promotion of conductivity for SEM is visible at the top left and bottom corner of Figure 4.12. The surface planes in Figure 4.12 and 4.13 are perpendicular to the Arcam electron beam, and thus, perpendicular to the growth direction. Grain structure is not clearly discernable from these images but do not have the columnar structure along the full length of the samples as seen in Figures 4.10 and 4.11. Higher magnification optical images were used to observe the nature of the grain structure later in this section.

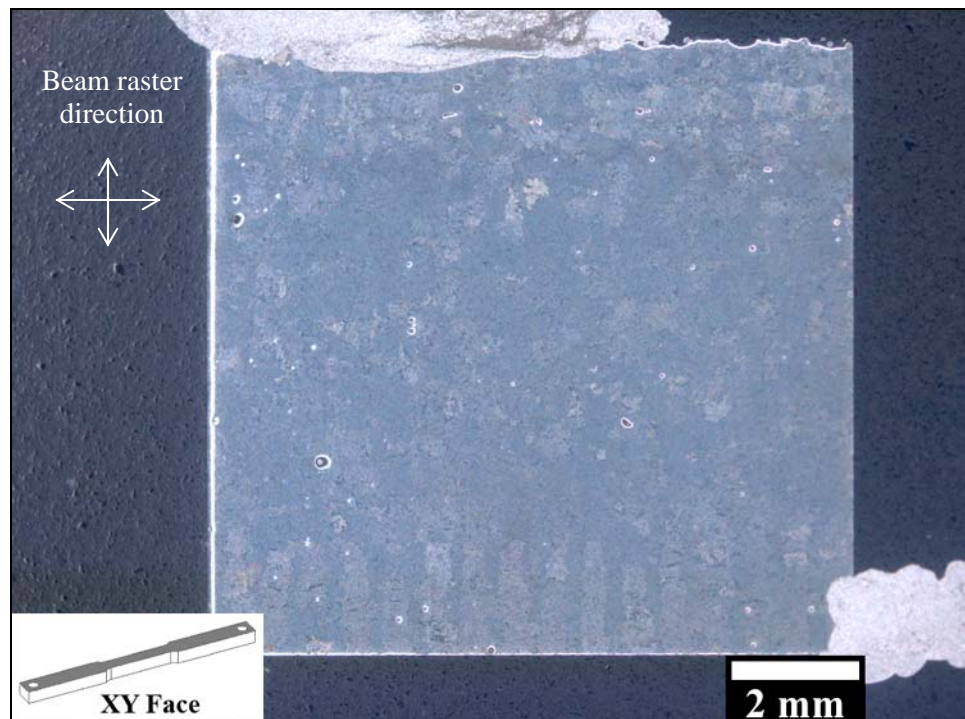


Figure 4.12. Low magnification optical image of mounted XY Face sample as used for optical microscopy and SEM. Component growth is normal to XY Face orientation.

Round shaped pores can be seen in these low magnification images in both the XY Face and XZ Cross Sections of Figures 4.12 and 4.13. The accuracy capability regarding solid object construction of the Arcam S12 EBM can be seen by the regularity of the three exterior surfaces in the XZ Cross Section of Figure 4.13 at the interface between the metal sample and the bakelite mounting material.

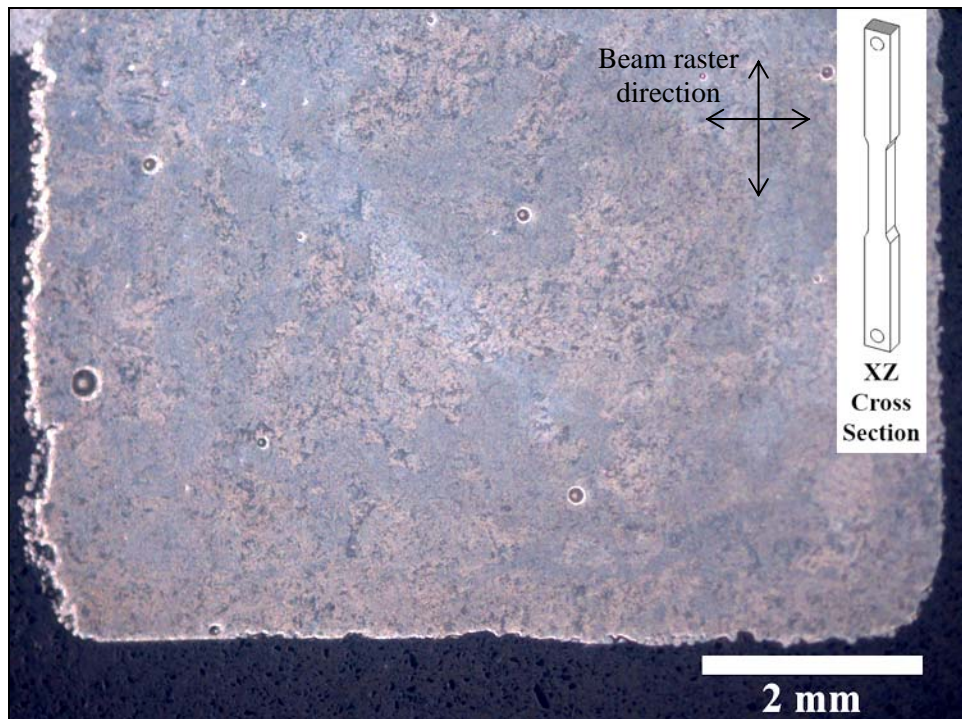


Figure 4.13. Low magnification optical image of mounted XZ Cross Section sample as used for optical microscopy and SEM. Component growth is normal to the Cross Section plane for XZ sample.

Figures 4.14 is a higher magnification optical micrographs of the polished and etched XY Face surface shown previously in Figure 4.12, with grain growth normal to the plane of

observation. When observing normal to the XY Face orientation, grain structure is relatively equiaxed compared to the columnar grains in the XZ Face component orientations shown in Figure 4.15. The growth direction of the XZ Cross Section plane is equivalent to that of the XY Face orientation. Figure 4.15 shows the equiaxed grain structure present in the XZ Cross Section plane (at higher magnification) that is present in the XY Face plane of Figure 4.14.

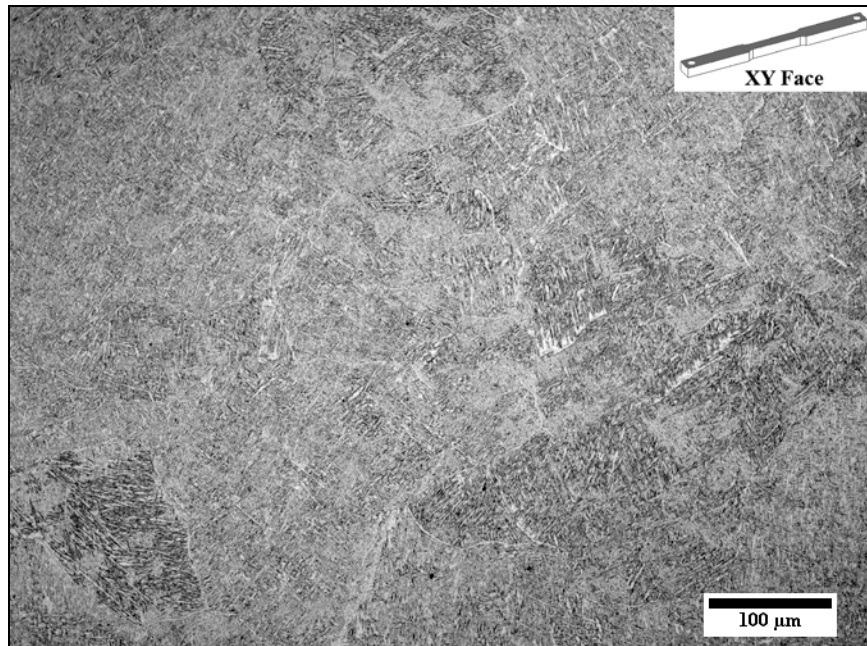


Figure 4.14. Optical micrograph of XY Face sample.

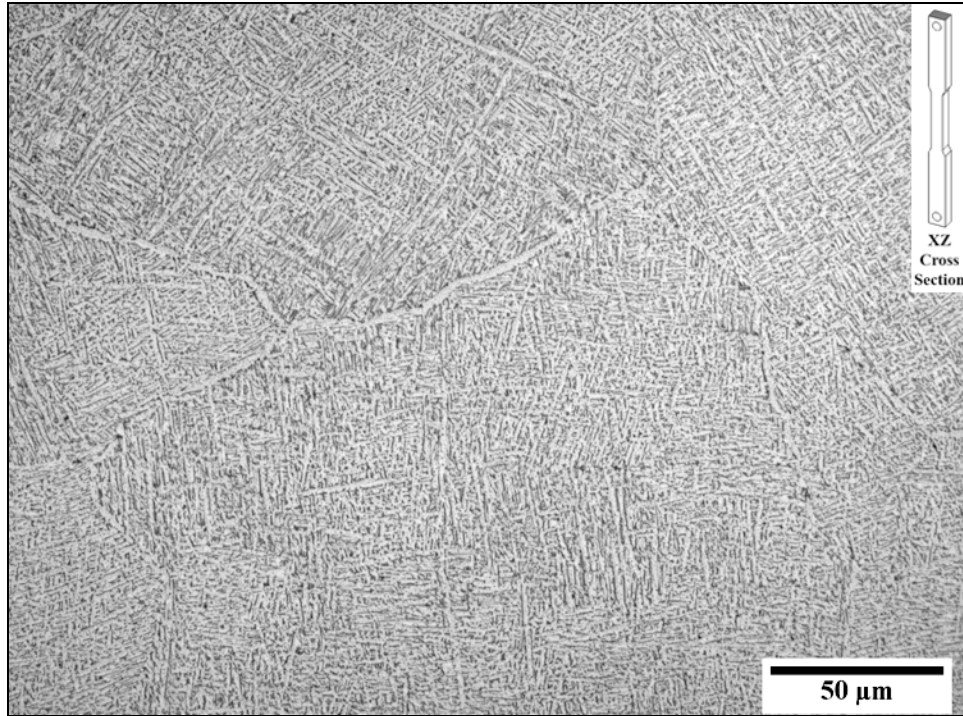


Figure 4.15. Optical micrograph of XZ Cross Section.

Figure 4.15 shows the existence of alpha at prior beta grain boundaries that define the resulting grain structure in the Arcam S12 produced samples. The average grain size diameter of prior beta grains is estimated based on the ASTM E 112 standard but should not be considered the absolute grain size due to the extremely long columnar structure parallel to the component growth direction. The grains themselves are difficult to discern and grain size is only reported as an estimate. Grain size is estimated by using the ASTM E 112 intercept method described in Section 3.8 of Experimental Procedure. The number of intercepts per unit length of test line (N_L) is for XY Face was 25.87 which gave a grain size of $G = 6$ when applied to Eq. 3.2. This correlates to an average prior beta grain size of 44.9 μm. The same

result was found for the XZ Cross Section sample; $N_L = 23.81$ for XZ $G = 6$ which calculates to an average grain size for this component to $44.9 \mu\text{m}$ also.

XZ Face and XZ Side orientations are equivalent as seen from figures 4.16 and 4.17 respectively. The grain morphologies of these two component orientations are equivalent. And are representative of the columnar structure defined by the alpha phase that has nucleated at prior beta grain boundaries during cooling. The Widmanstätten microstructure is present within the grains. The grains extending along the direction of the electron beam which is perpendicular to the solid/liquid interface do not show any evidence of discontinuity with each subsequent deposition layer.

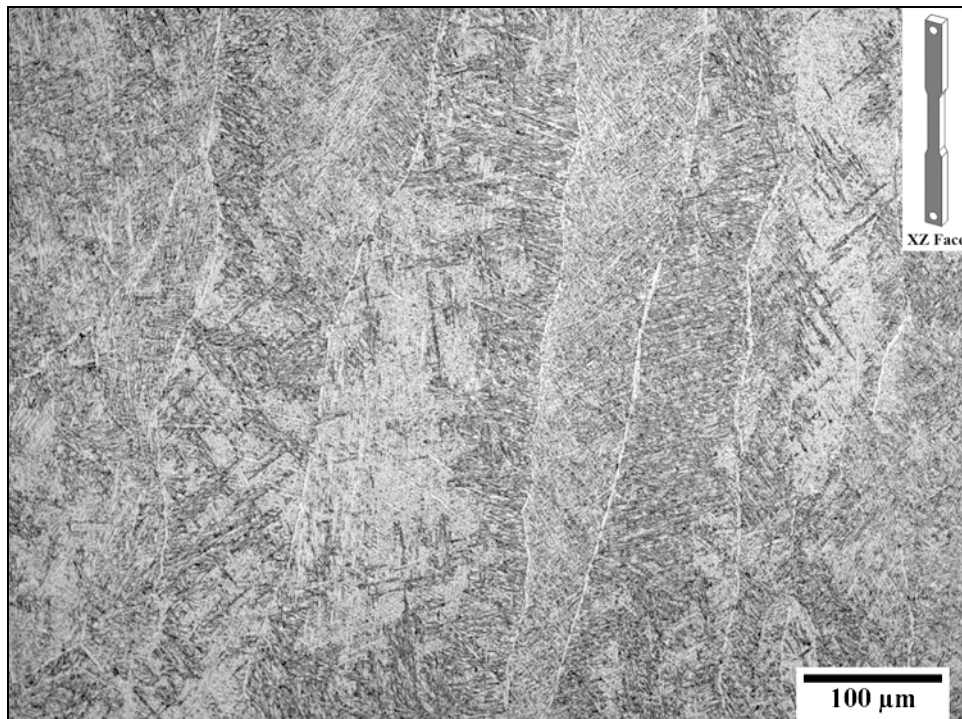


Figure 4.16. Optical micrograph of XZ Face.

Sample orientations perpendicular to the Arcam electron beam (i.e. XZ Face, XZ Side, XY, Cross Section, and XY Side), the images are oriented such that the growth direction is upward in the z-direction on the page. Assuming grain growth is approximately parallel to the z-direction, prior beta grains appear to have a tapered structure at their endpoints.

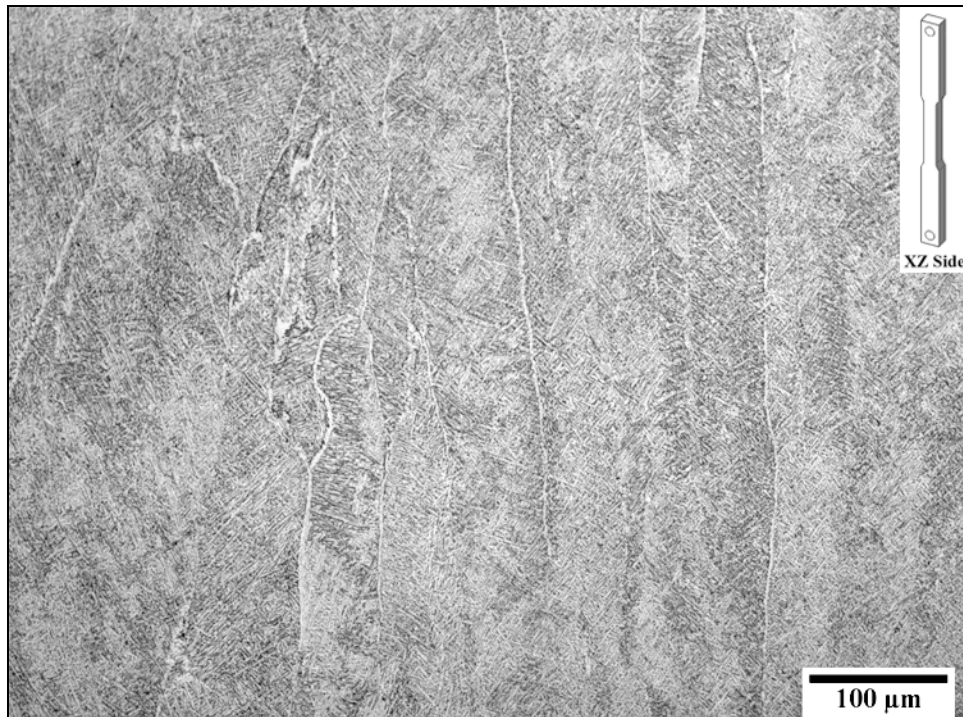


Figure 4.17. Optical micrograph of XZ Side.

The average width of the grains is based on several measurements from various optical and scanning electron microscope images captured perpendicular to the growth direction. The average grain width for the XY sample is 62 μm with a minimum of 15 μm and maximum of 153 μm . The average grain width for the XZ sample is 63 μm with a

minimum of 9 μm and maximum of 188 μm . A summary for the values for prior beta grain diameter and width for samples produced by the Arcam S12 EBM machine are listed below in Table 4.1. Interestingly, these values are close to the average initial particle size of 67 μm .

Table 4.2. Prior beta grain size measurements for Arcam S12 produced components.

Arcam S12 Component Type	Average Grain Size	Average Grain Size (Width)
	(μm) Parallel to Incident Arcam Electron Beam	(μm) Normal to Incident Arcam Electron Beam
XY	45	62
XZ	45	63

4.3.2. Description of $\alpha + \beta$ Phase Morphology

In Figure 4.18, higher magnification optical microscopy of the XY Side sample shows the columnar grain structure. The alpha (HCP) phase appears white and the beta (BCC) phase is the dark regions between the α phase. The microstructure that forms is Widmanstätten [1, 13] and is characterized by fine acicular α , with β phase present between the α phase. Coarse acicular and blocky alpha regions were observed in all Arcam produced samples as the microstructure features are not well defined throughout, but the microstructure is predominantly that of fine structures, usually less than 5 μm in lath width. The alpha phase has nucleated on prior beta grain boundaries having cooled from above the beta transus temperature, forming at the grain boundaries of the component at room temperature.

The alpha phase regions are described as lath and plate-like acicular alpha in both the XY Side sample in Figure 4.18 and the XY Cross Section in Figure 4.19. These alpha laths consist of a wide variety of lengths and widths. The prior beta grains (see arrow, Figure 4.18), which are predominantly alpha with some beta decoration.

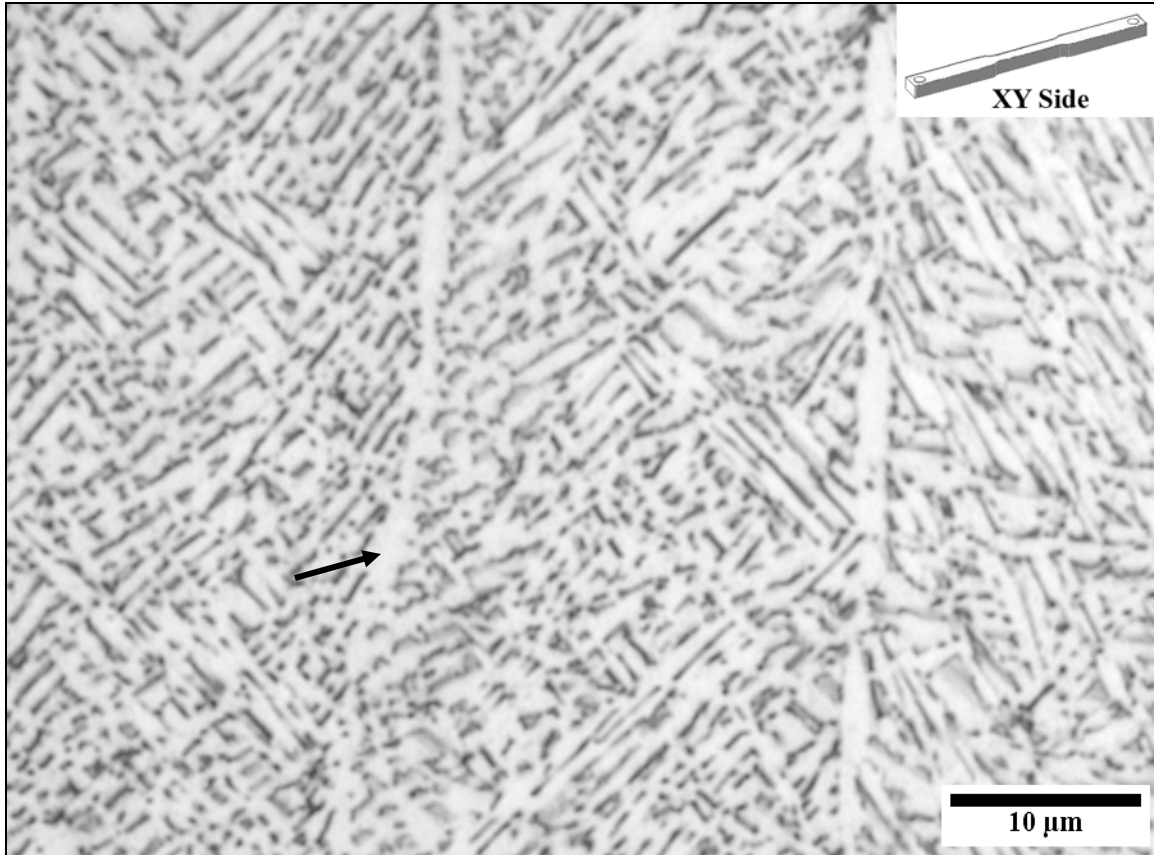


Figure 4.18. Optical micrograph of XY Side sample. Arrow identifies prior beta grain boundary.

The incident electron beam of the Arcam EBM process is normal to the XY Face sample surface shown in Figure 4.19 and therefore this view is normal to the columnar grains. In Figure 4.19, acicular α is observed in the XY Face component orientation with β phase between the α . Alpha existing at prior β grain boundaries contains small amounts of beta phase in some areas. A broad range of aspect ratios are observed for the acicular α in this component orientation as well. The Widmanstätten microstructural morphology of the α phase is clearly present. The Arcam process is considered a rapid solidification process but

the cooling rate is still slow enough to not induce a Martensitic transformation. The alloy powder is melted and then solidifies rapidly. The component retains heat but there is no mechanical processing possible in order to break up the Widmanstätten plates and achieve a microstructure other than that of a Widmanstätten type. The equiaxed microstructure observed in the forged turbine blade is a result of being mechanically processed in the α/β region (i.e. below the β transus temperature) of the phase diagram followed by a recrystallization anneal (925°C for 1 hour) and allowed to slow cool.

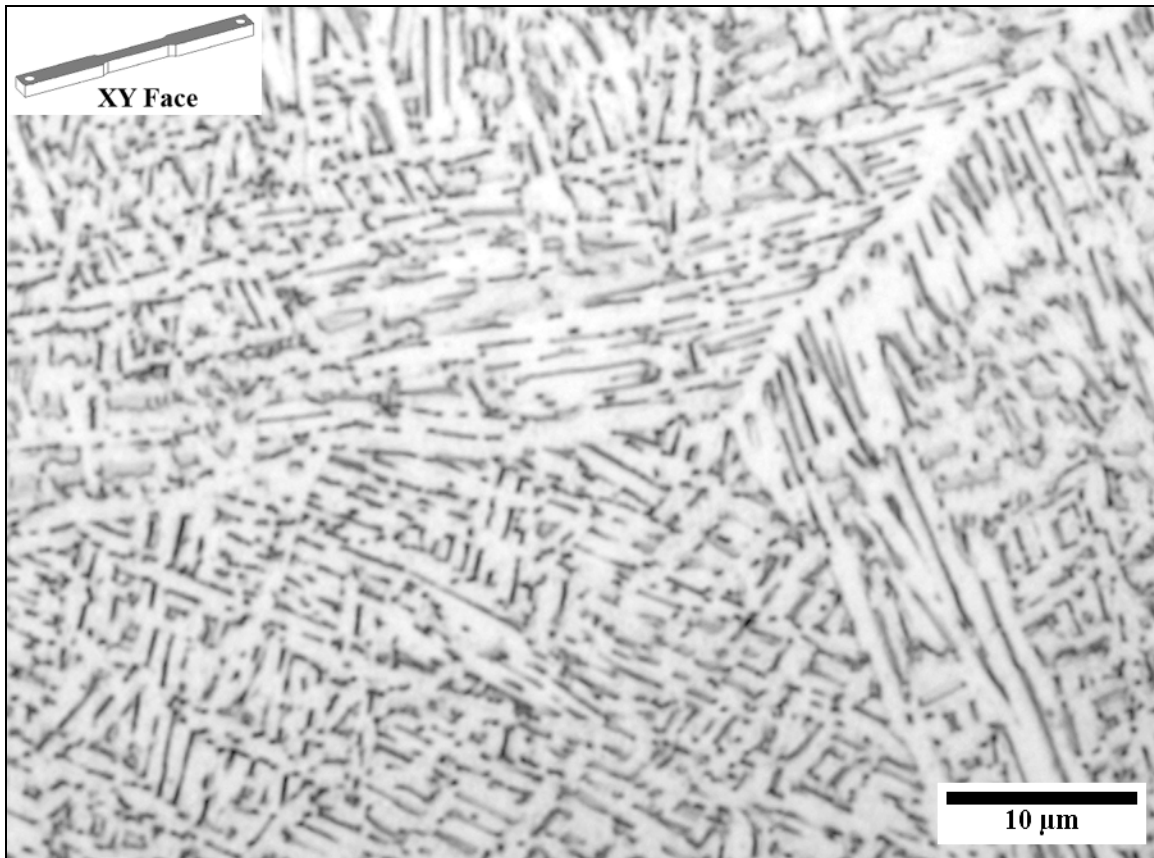


Figure 4.19. Optical micrograph of XY Face sample.

Figure 4.20 is an SEM micrograph of the XY Face plane. Figure 4.21 is an SEM micrograph of the XY Cross Section plane. The fine structure of the beta phase is visible in both images. A grain boundary is featured in Figure 4.21 which runs diagonally through the image separating two areas with different orientations. The cooling rate of the Arcam process is fast enough to promote the fine structure which may be responsible for the increased ductility observed in tensile testing [3] and which also may explain the unusually high percent elongation that was found by Bass [6]. Beta processed microstructures with alpha laths of low length/width ratios have been known to have increased ductility [24].

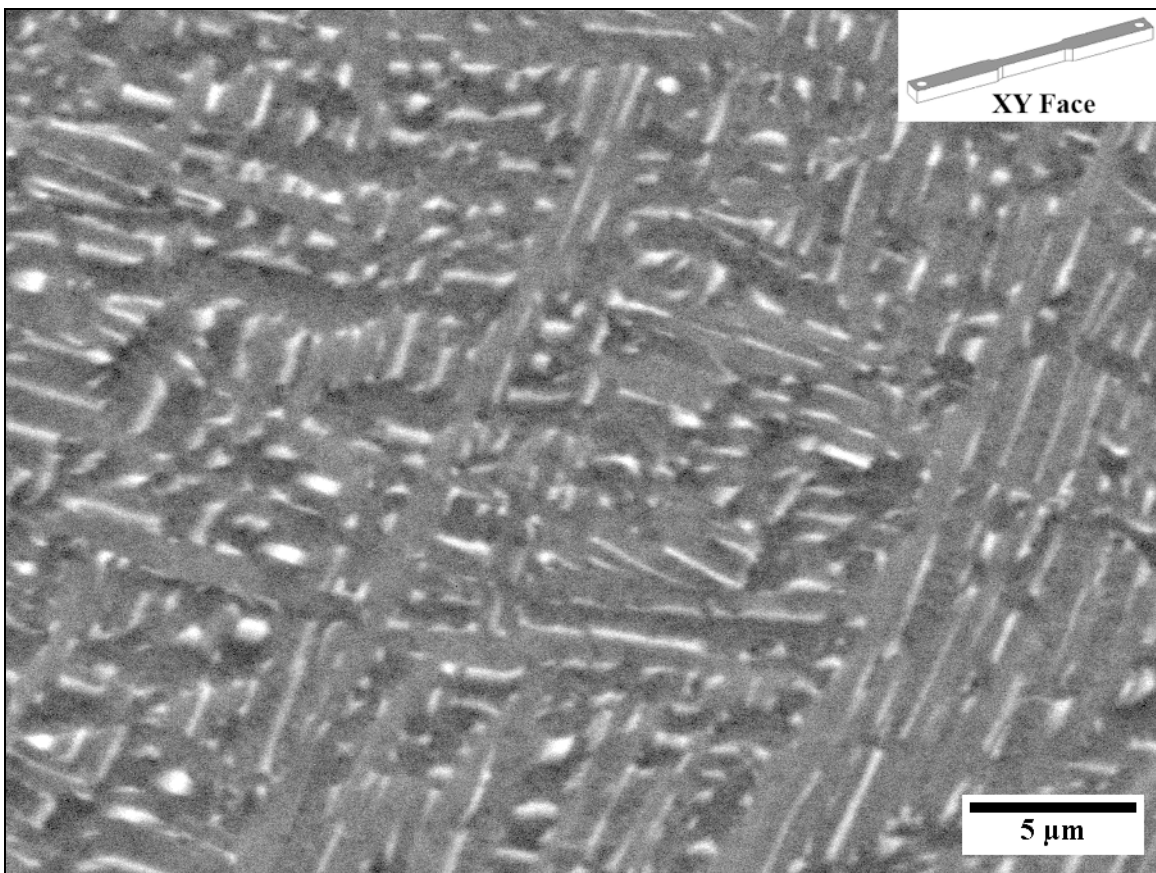


Figure 4.20. SEM micrograph image of XY Face.

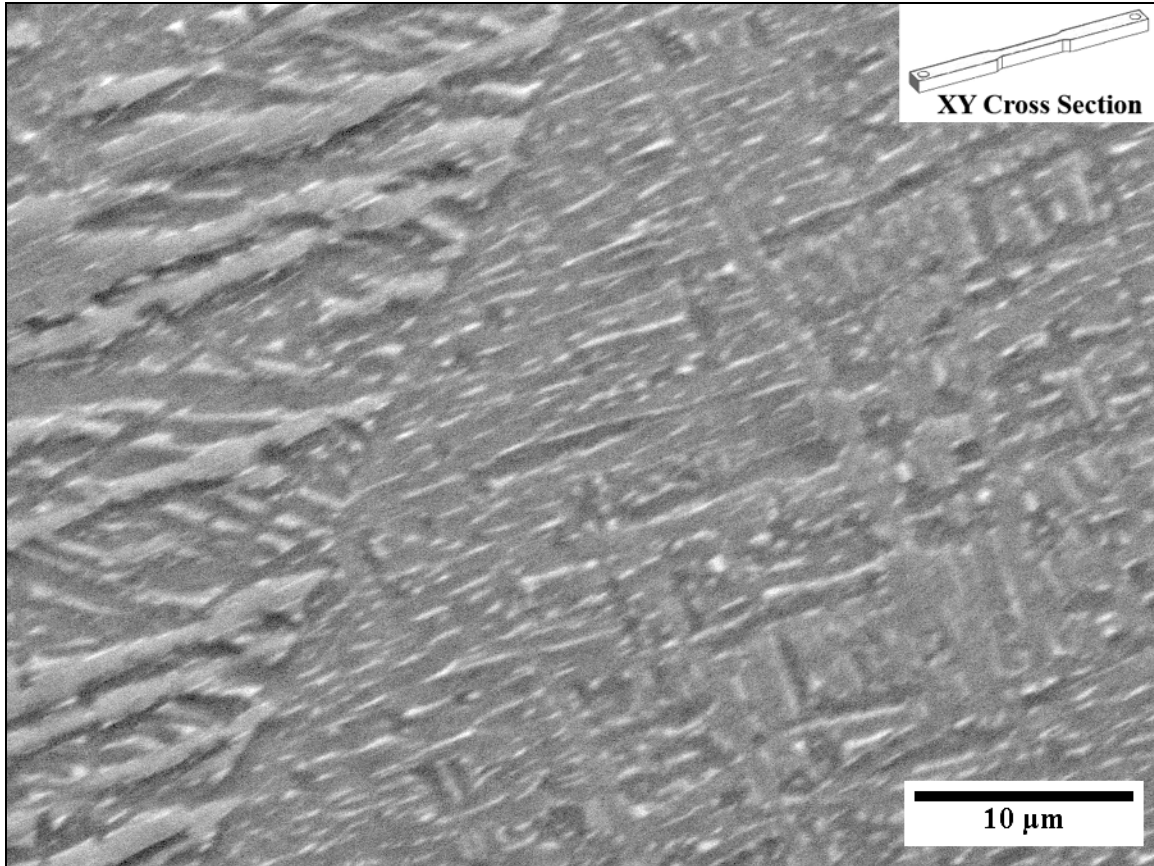


Figure 4.21. SEM micrograph image of XY Cross Section.

Similar fine microstructural features of the XZ specimen are shown in the SEM micrographs of the XZ Side plane of Figure 4.22 and the XZ Cross Section plane of Figure 4.23. A portion of the columnar grain boundary can be seen in Figure 4.22 (see arrow). The more equiaxed grain structure along the view that is perpendicular to the incident Arcam electron beam is shown in the XZ Cross Section plane of Figure 4.23.

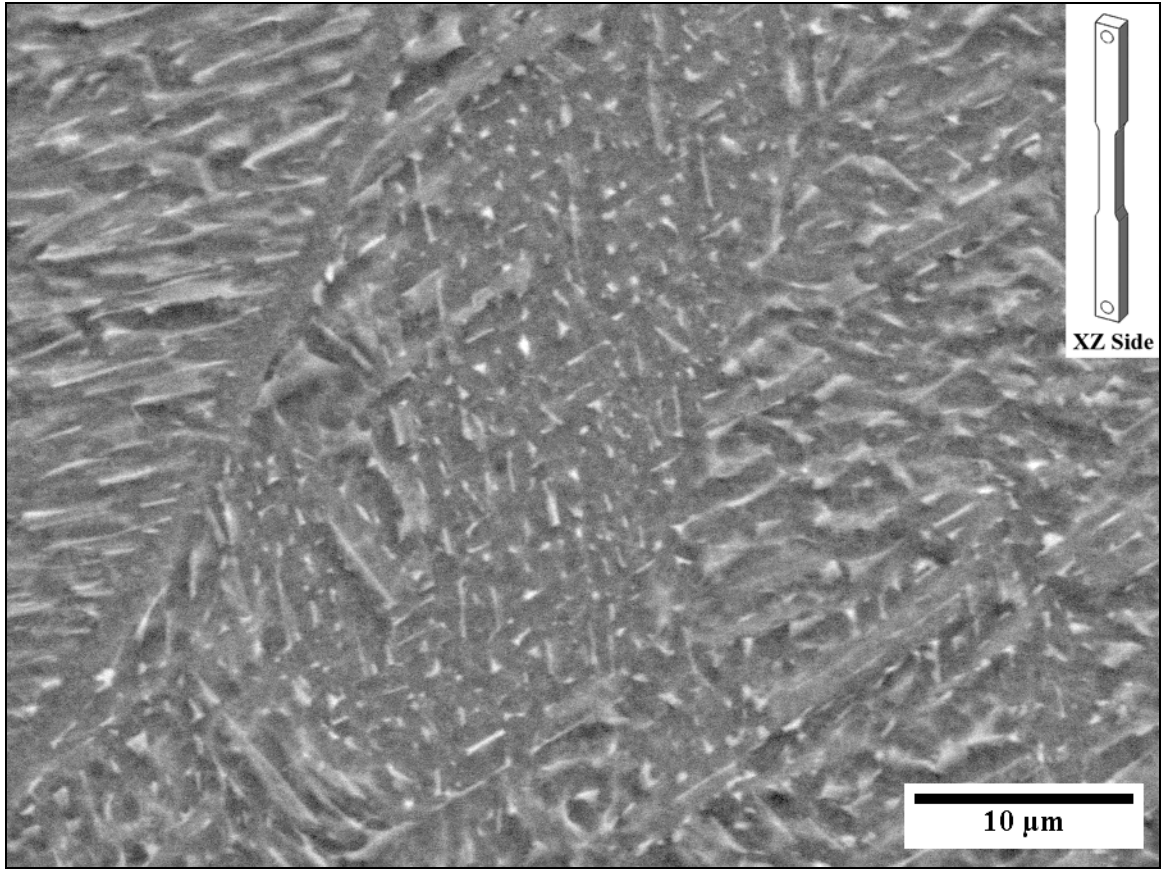


Figure 4.22. SEM micrograph image of XZ Side.

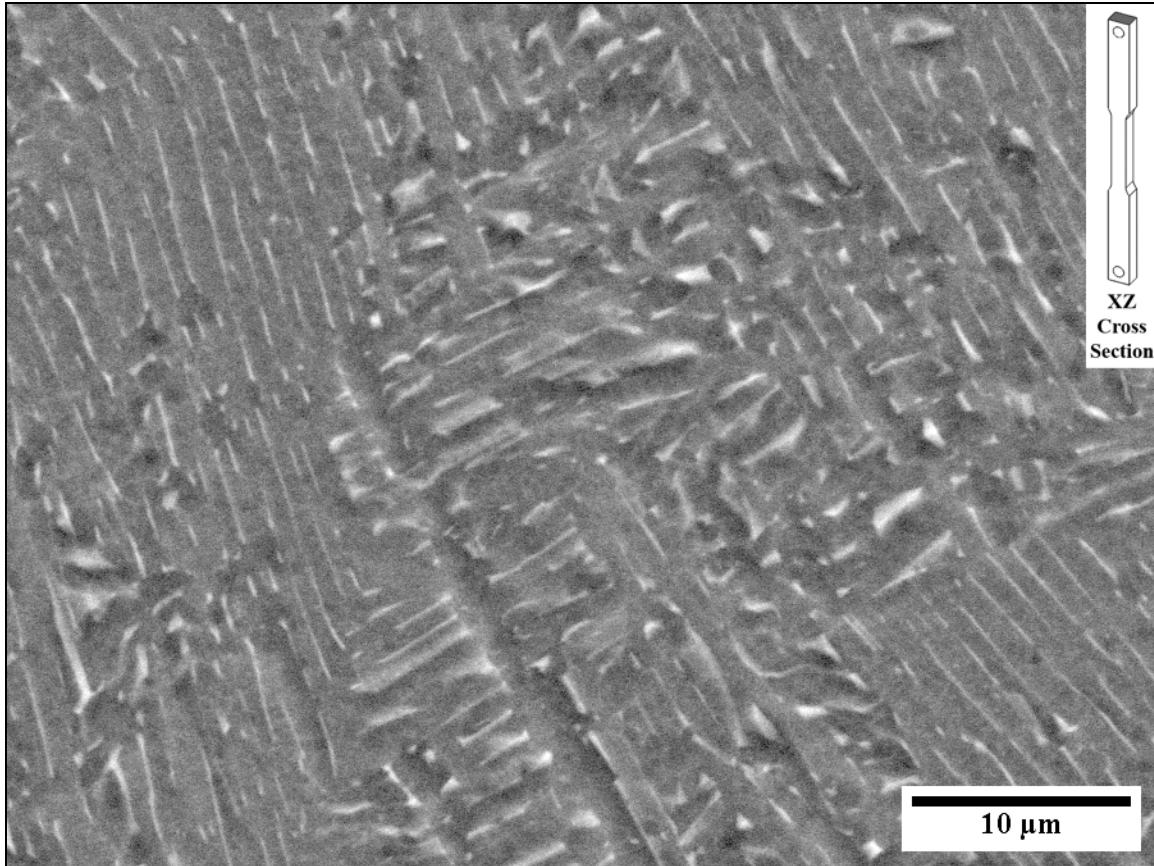


Figure 4.23. SEM micrograph image of XZ Cross Section.

4.3.3. Volume Fraction of β Phase

The volume fraction of β is measured using by a systematic point count method along the ASTM E 562-08 standard described in Section 3.9 of Experimental procedure. The number of points that fall on the minor phase are recorded. Twelve optical micrographs were used to calculate the volume fractions of each phase present for the XY and XZ orientation samples. Four images from each orientation (Face, Side, and Cross Section) were used. The arithmetic average for the volume fraction of beta in the XY sample is 31.8% with a standard deviation estimate of 5.8. The volume fraction of the beta phase is $31.8\% \pm 3.7$. The relative

accuracy for this measurement is 11.5%. The arithmetic average for the volume fraction of beta in the XZ sample is 41.6% with a standard deviation estimate of 4.3. The volume fraction of the beta phase is $41.6\% \pm 2.7$. The relative accuracy for this measurement is 6.6%.

Table 4.3. Volume fraction of beta phase for Arcam S12 produced components.

Arcam S12 Component Type	Volume Fraction of Beta Phase (%)	Relative Accuracy (%)
XY	31.8 ± 3.7	11.5
XZ	41.6 ± 2.7	6.6

4.3.4. Transmission Electron Microscopy of S12 - Produced Components

The following section shows TEM results for the microstructures of the XY and XZ orientation components produced by the Arcam S12 EBM machine. Acicular alpha plates are more clearly shown in Figure 4.24 which is a bright field TEM image of a section taken from the XY Side plane, prepared by electropolishing, captured in the [01-12] zone axis. The beta phase appears as the fine, dark regions between the alpha phase, which appears light on the left and right hand sides of the image. The darker appearance of the alpha plates in the center of the image is due to diffraction contrast. The alpha plates were found to be typically less than 2 microns across. The stitch-like features in the TEM images are dislocations arrays which define subgrains within the alpha plates.

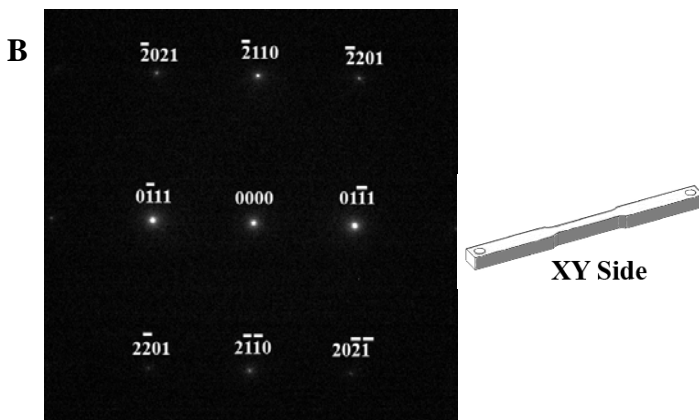
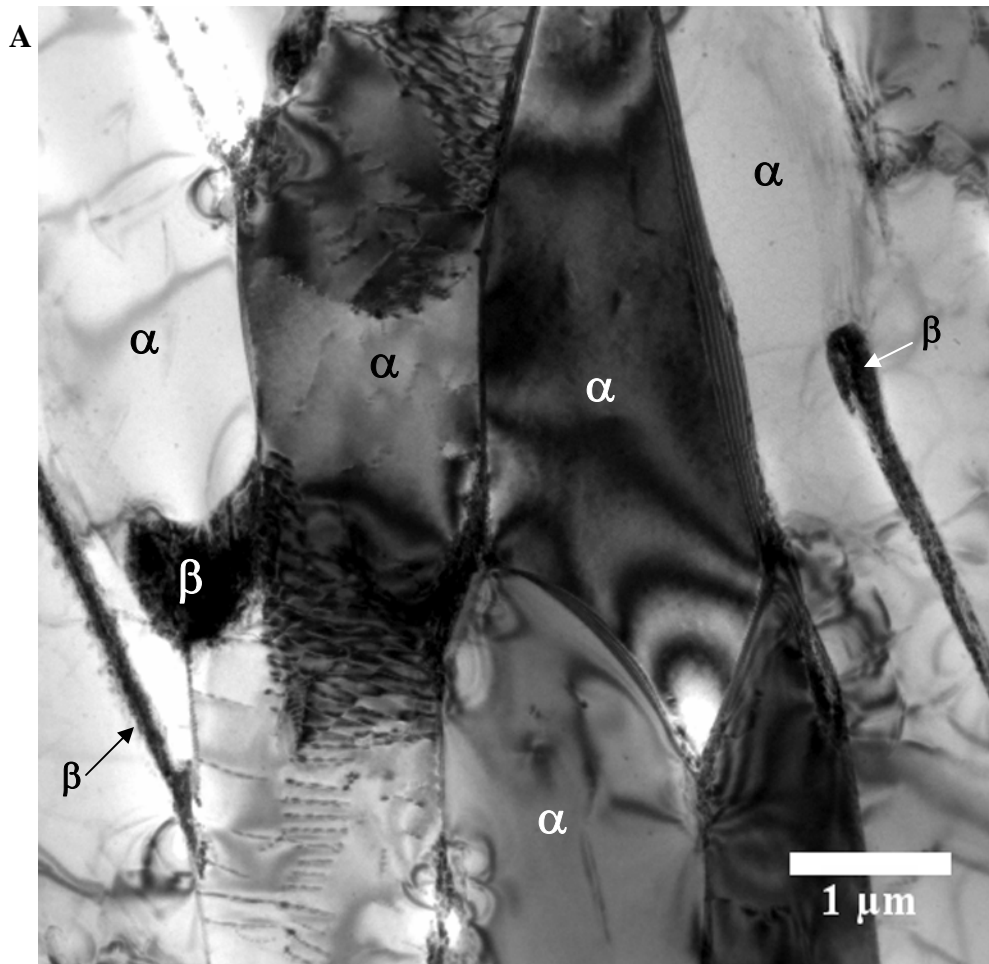


Figure 4.24. a) Bright field TEM micrograph of XY Side sample and, b) diffraction pattern.

Zone axis = $[01\bar{1}2]$.

Figure 4.25 is an increased magnification TEM bright field image illustrating the retained beta phase (shown by the arrows) that exists between alpha plates. The morphology of the beta phase shown here is similar to that seen in the literature [13]. The beta phase is approximately 60 nm in thickness.

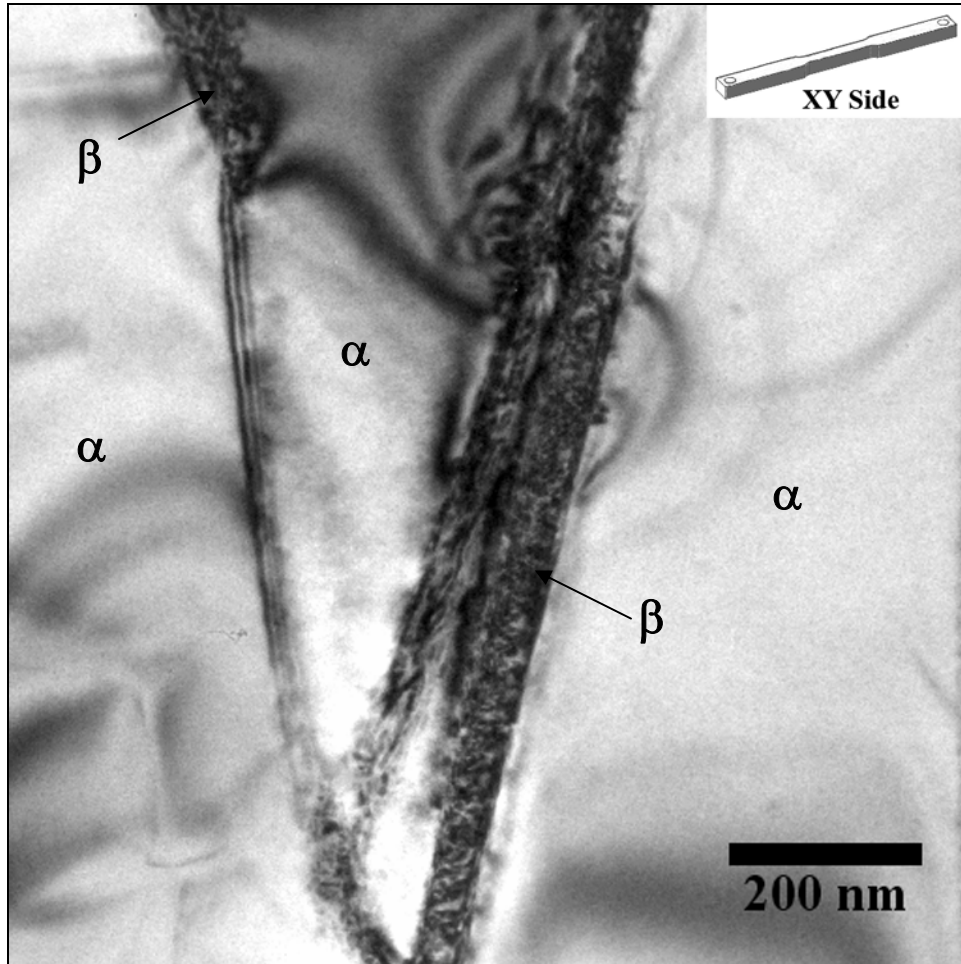


Figure 4.25. Bright field TEM micrograph of XY side sample.

The bright field TEM micrograph of the XZ Face plane in Figure 4.26 shows multiple regions of what may be the discontinuous beta phase that is seen in the SEM micrographs. Dislocation networks can be seen within the alpha matrix and extending between the various (potentially) beta phase regions, effectively creating alpha subgrains.

Figure 4.27 is a TEM bright field image close to the [01-10] zone axis of the HCP alpha phase. This sample was prepared from the XZ Face plane. This image also illustrates the size and shape of the (dark) beta phase regions within the alpha phase. The scale bar in this image is 0.5 μm . Dislocation networks are once again observed to be present between the α and β phases. Multiple dark spots within the supposed beta phase regions are observed in this micrograph which may suggest precipitation of another phase is present.

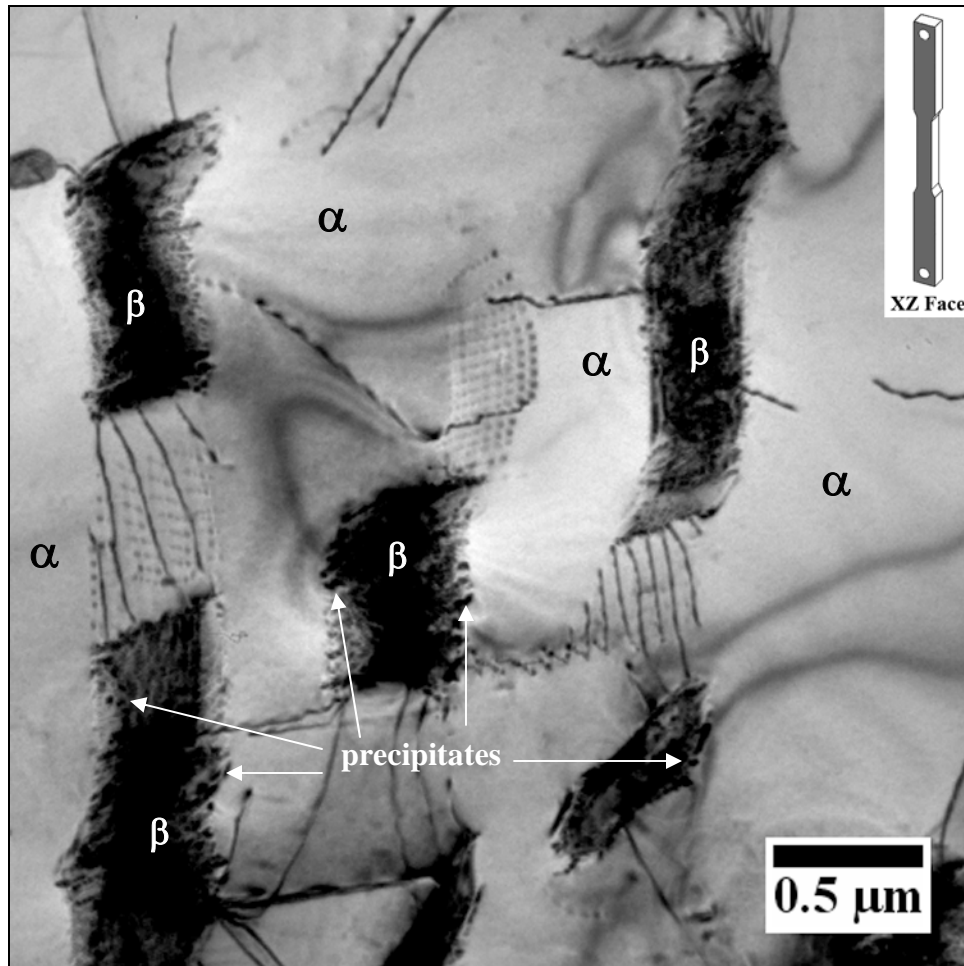


Figure 4.26. Bright field TEM micrograph of XZ Face sample.

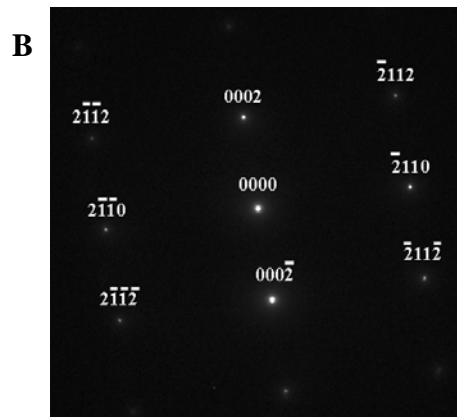
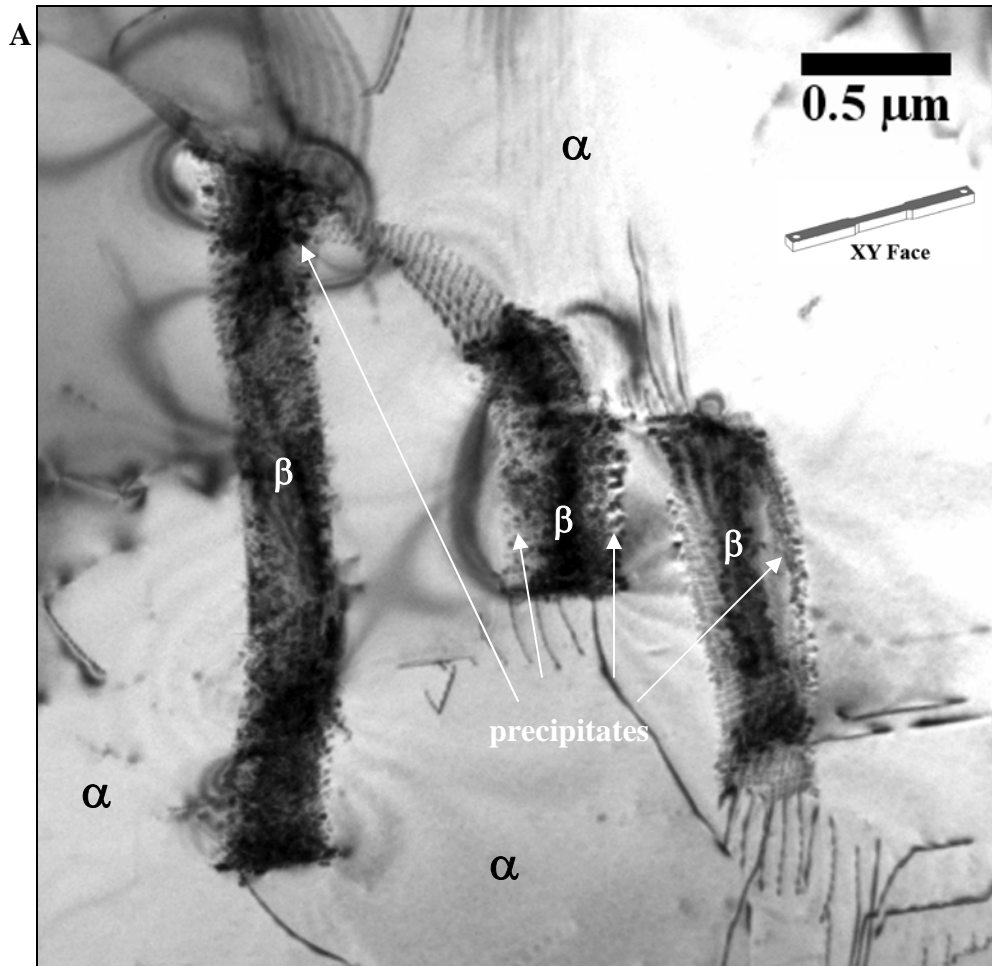


Figure 4.27. a) Bright field TEM micrograph of XZ Face sample and, b) diffraction pattern.

Zone axis = $[01\bar{1}0]$.

Figure 4.28 is a TEM bright field image of the XZ Face plane prepared by focused ion beam (FIB). Due to the ion beam sputtering process by which the FIB samples are produced, they are substantially thicker and have much less total thin area for examination than a good electropolished sample. Dislocations can be seen piled up in the alpha phase at the beta phase and pinned by the beta phase.

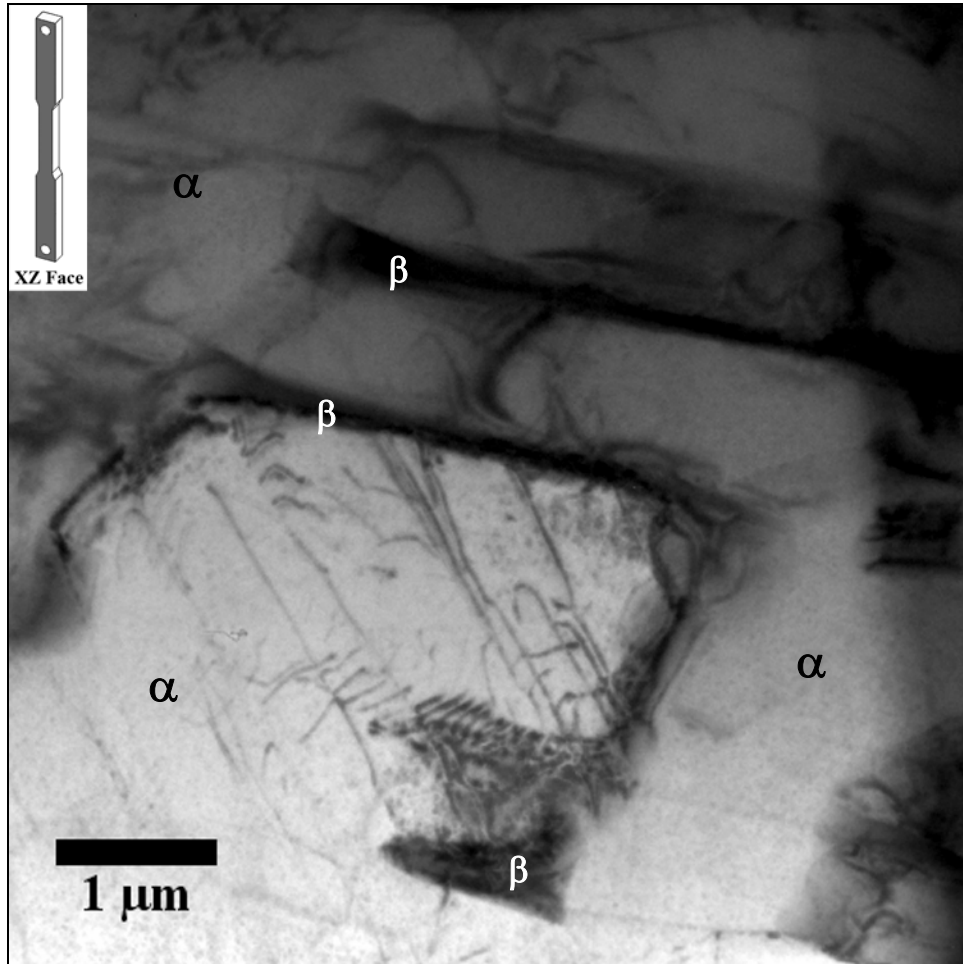


Figure 4.28. Bright field TEM image of XZ Face FIB sample.

4.3.5. Scanning Transmission Electron Microscopy of S12 - Produced Components

The following images are low energy, SEM-based STEM images of the XZ Face orientation that was prepared via FIB, featured at the end of the last section. Figure 4.30 is a dark field STEM image obtained in the Hitachi S-5500 at 30 kV. The region on the left of the micrograph has been thinned more so than the region on the right. The light regions are presumed to be the α phase. The dark regions are consistent in shape and size to be the β phase. An arrow in the figure points to a beta phase region. The purpose of this part of the study was to obtain chemical analysis data for the phases.

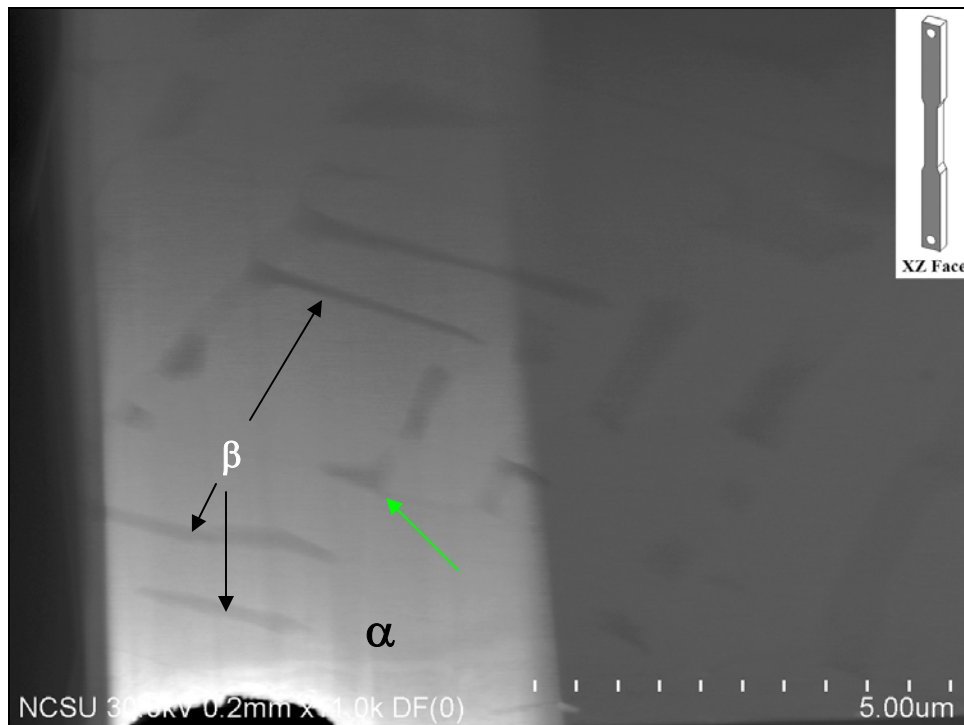


Figure 4.30. STEM image of XZ face FIB sample at 30 KV. Green arrow identifies EDS dot map region.

Energy dispersive X-ray spectroscopy (EDS) was performed on the FIB sample to substantiate the α and β regions. EDS mapping was performed on the area of interest shown by the arrow in Figure 4.30. Figure 4.31 is a secondary electron image of this area while Figure 4.32 is an EDS dot map of the same region that shows the presence of vanadium in proportion to the concentration across the area of Figure 4.31. Since vanadium is a beta stabilizer, the presence of vanadium in higher quantities than the surrounding areas suggests that the beta phase does in fact exist where presumed. Locci and Welsch [25] have shown beta phase in Ti-6Al-4V to be enriched in vanadium by using EDS. The shape of the beta particle in Figure 4.31 is reproduced by the green color that is used to show where the EDS system has detected more vanadium within the beta particle.

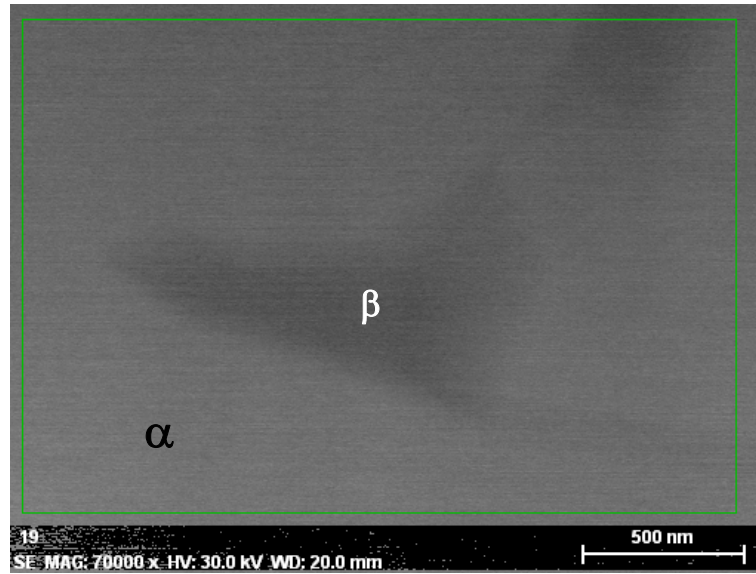


Figure 4.31. STEM image of XZ Face FIB sample at 30 KV. Area used for EDS dot mapping.

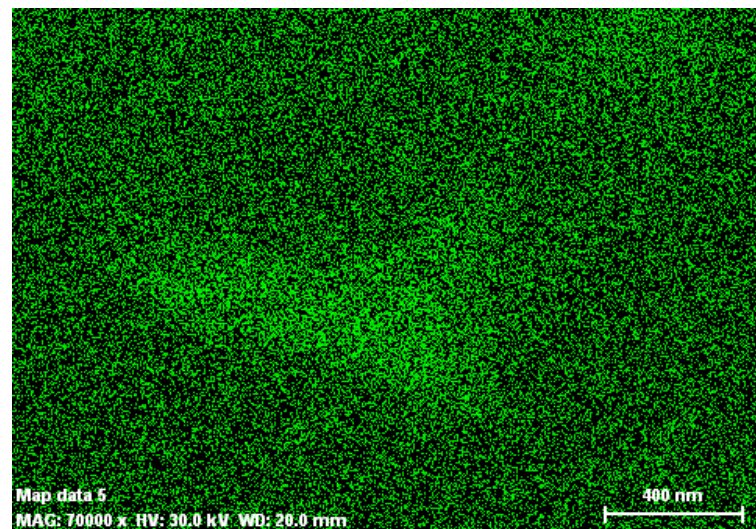


Figure 4.32. EDS vanadium (in green) map image of XZ face FIB sample at 30 KV.

Figure 4.33 is a STEM image of presumed beta phase from another area in close proximity of the beta particle examined in Figure 4.31. EDS data was acquired along the line that is drawn across the striped areas of the secondary electron image in Figure 4.33.

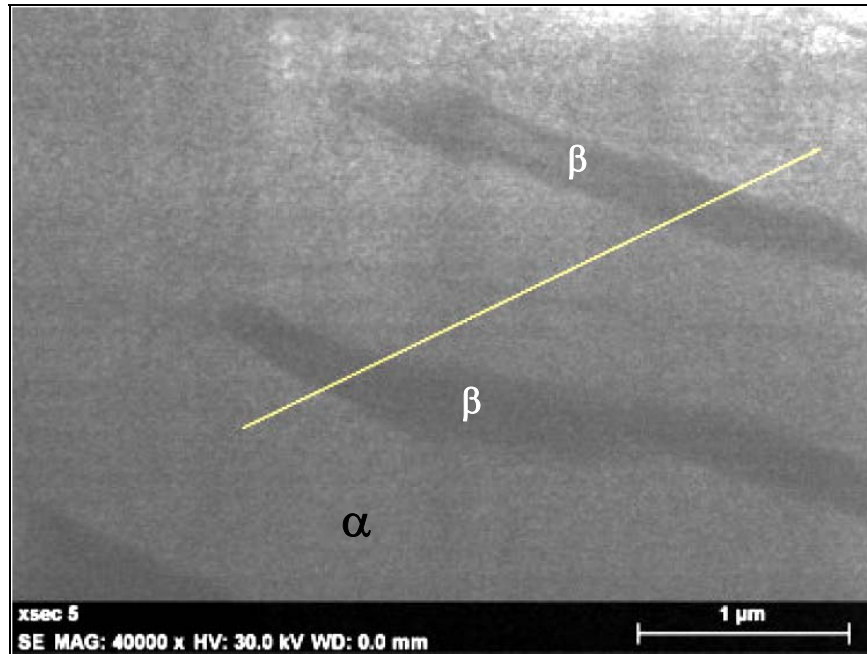


Figure 4.33. STEM image of XZ face FIB sample at 30 KV. Area used for EDS line scan.

Figure 4.34 shows the relative intensities for titanium, aluminum, and vanadium. In this chart, titanium is represented in green, vanadium in blue, and aluminum in red. Titanium is present in highest concentration as expected. The dark areas of Figure 4.33 that are presumed beta phase are clearly rich in the beta-stabilizing vanadium and deficient in the alpha-stabilizing aluminum.

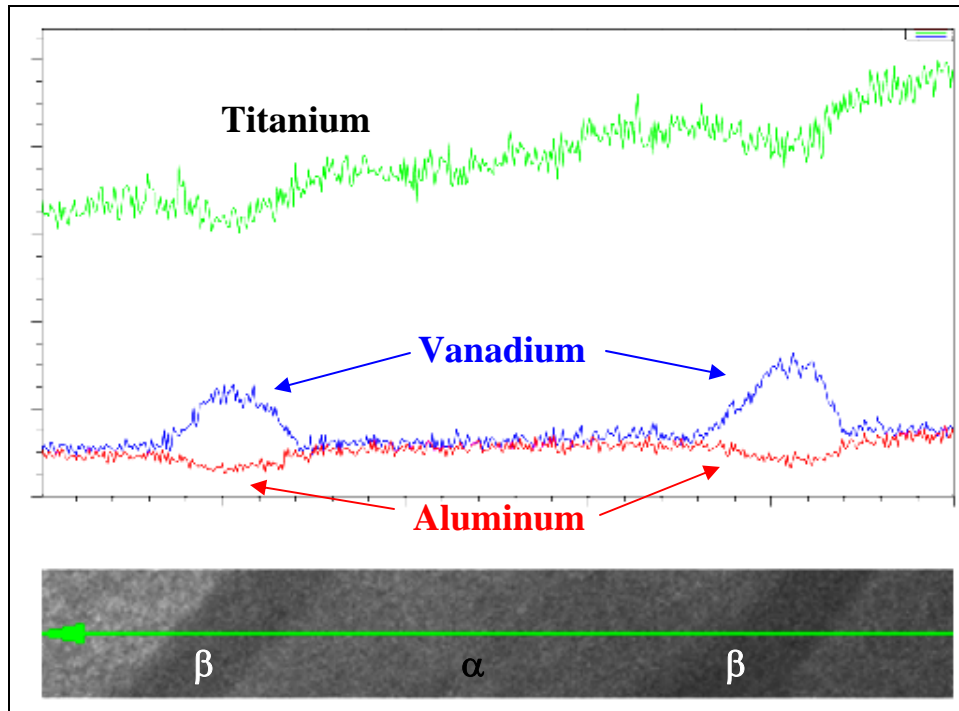


Figure 4.34. EDS line scan across two-phase region from STEM image of XZ face FIB sample at 30 KV. Chart shows relative amounts as a function of position.

Figure 4.35 shows the EDS spectra from the line scan of Figure 4.34. Characteristic energies for each element present are on the x-axis. The y-axis is a measure of intensity in the form of counts per second. The spectra confirms that sufficient counts have been collected (14, 590 count per second) but do not provide the localized information that is available in Figure 4.34.

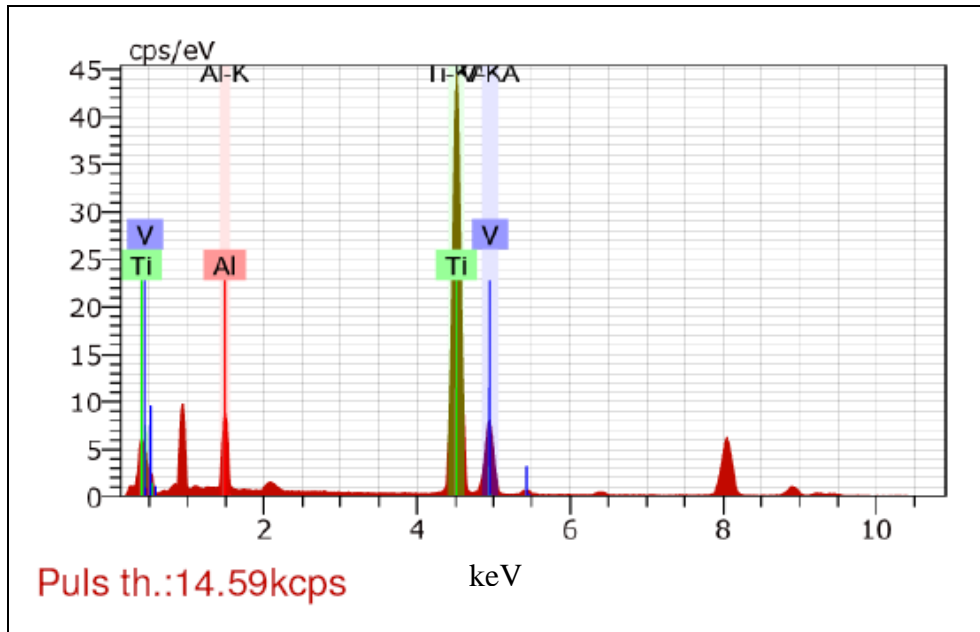


Figure 4.35. EDS spectrum from line scan from STEM image of XZ face FIB sample at 30 KV.

Existence of beta phase in Ti-6Al-4V samples from optical, SEM, and TEM micrographs as claimed can be done so from the recognition of features reported throughout published scientific literature [1, 16, 13, 25] and in the case of Locci and Welsch [25], the use of EDS in addition to TEM data. The dark spots appearing in the beta regions of the TEM micrographs of Figures 4.26 and 4.27 suggest that a more complex microstructure exists that cannot be described simply as beta phase particles.

4.4. Microstructure of Arcam A2-Produced Component

4.4.1. Grain Size and Morphology

Figure 4.36 is an optical micrograph of the horizontal cylinder (HC) mounted in bakelite and etched to expose the Cross Section plane. As was reported earlier for the samples grown in the S12 machine, long columnar grains were found to form parallel to the build growth direction with horizontal banding created parallel to and as a result of the additive layer growth method. Porosity within the sample was also again noted.

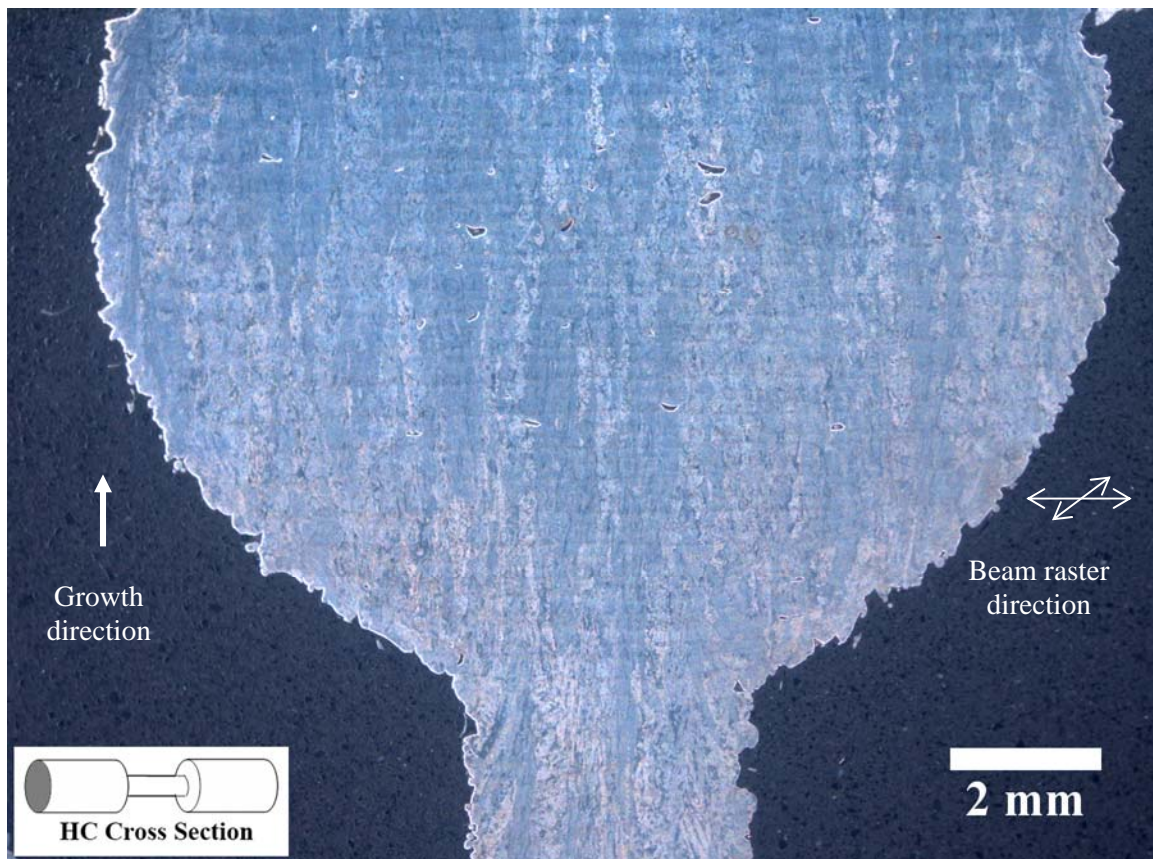


Figure 4.36. Low magnification optical images of mounted horizontal cylinder (HC) sample as used for optical and scanning electron microscopy.

The optical micrograph in Figure 4.37 is for the HC Face plane, perpendicular to the incident electron beam used for melting. Relatively equiaxed grains are observed along with regions containing porosity, such as at the lower left in the image.

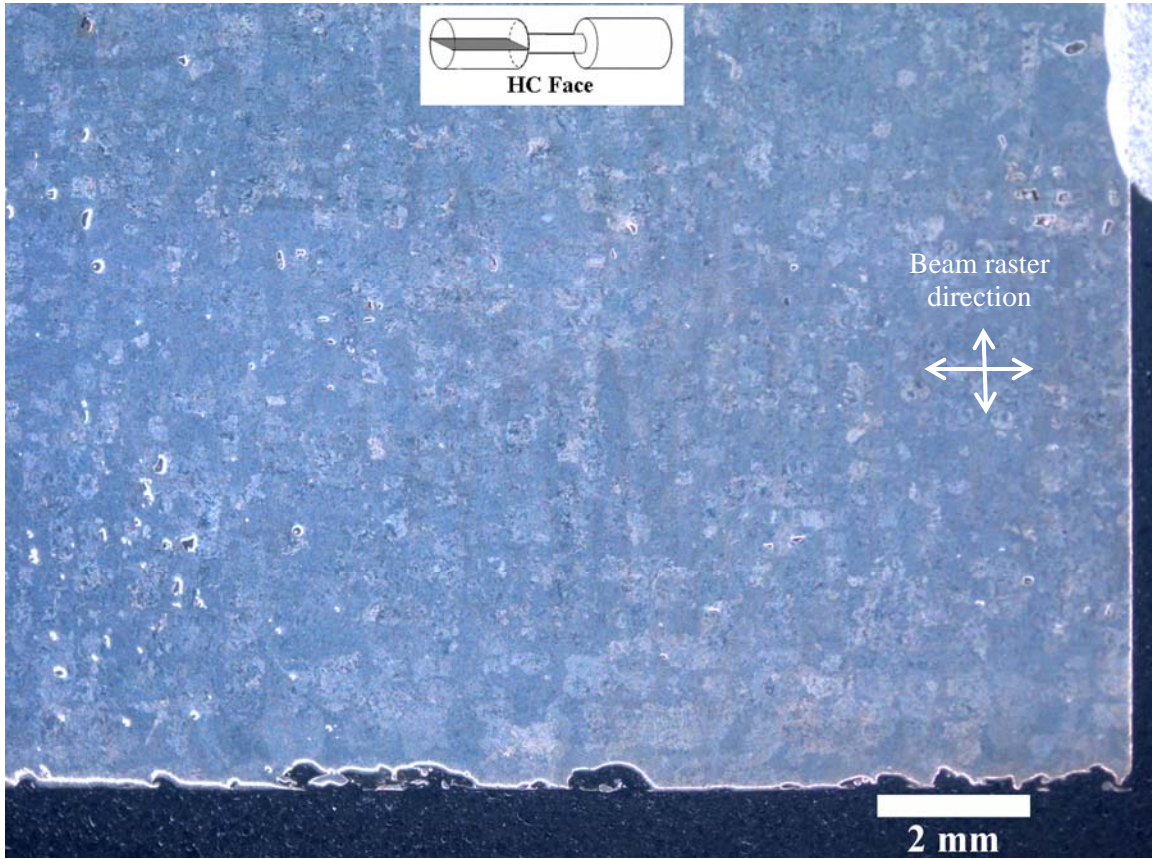


Figure 4.37. Low magnification optical images of horizontal cylinder (HC) sample used for optical and scanning electron microscopy. Component growth is normal to the face orientation for HC sample.

Figures 4.38 and 4.39 are optical micrographs of increasing magnification that feature the equiaxed grain structure parallel to the growth direction of the HC Face plane. Alpha phase is present at prior beta grain boundaries and appear as the white areas forming grain

boundaries. Figure 4.40 is an optical micrograph of the HC Cross Section plane. Elongated grains are apparent and are somewhat irregular in shape. Tapered regions are shown where new grains are formed.

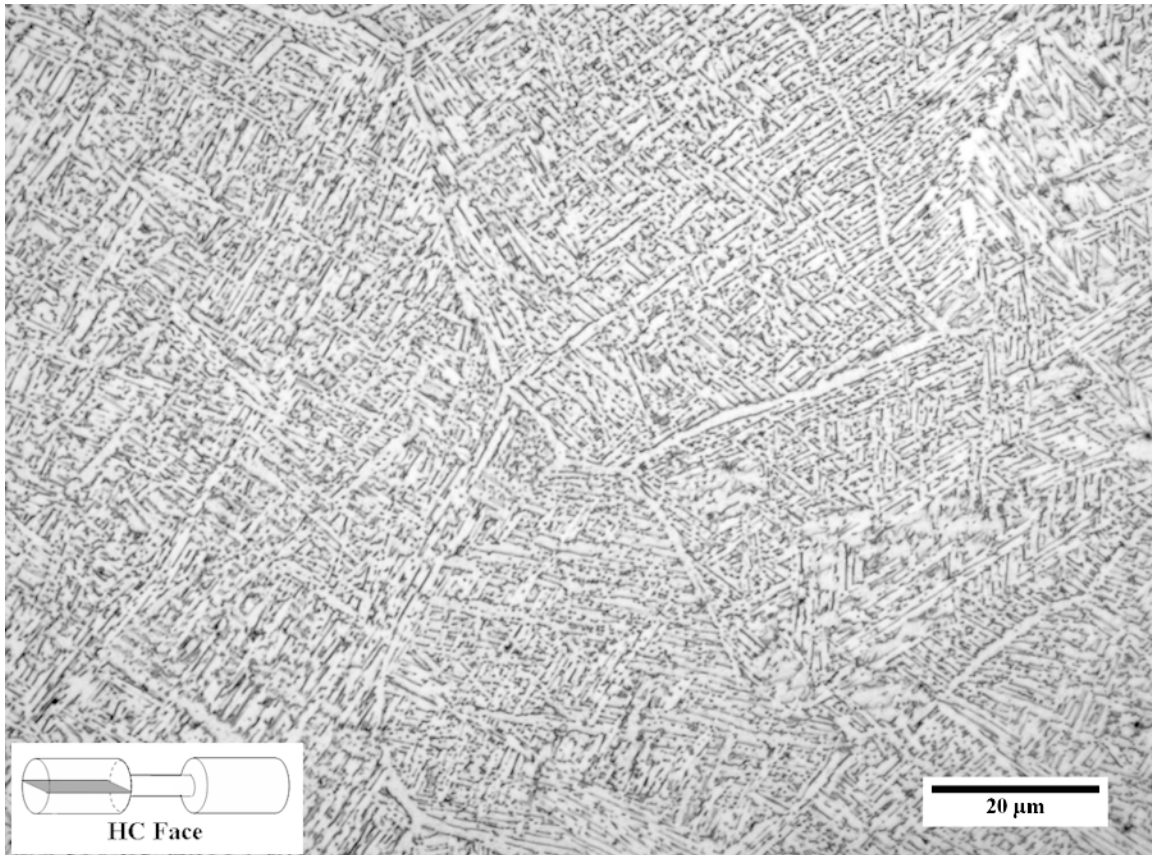


Figure 4.38. Optical micrograph of HC Face (normal to growth direction).

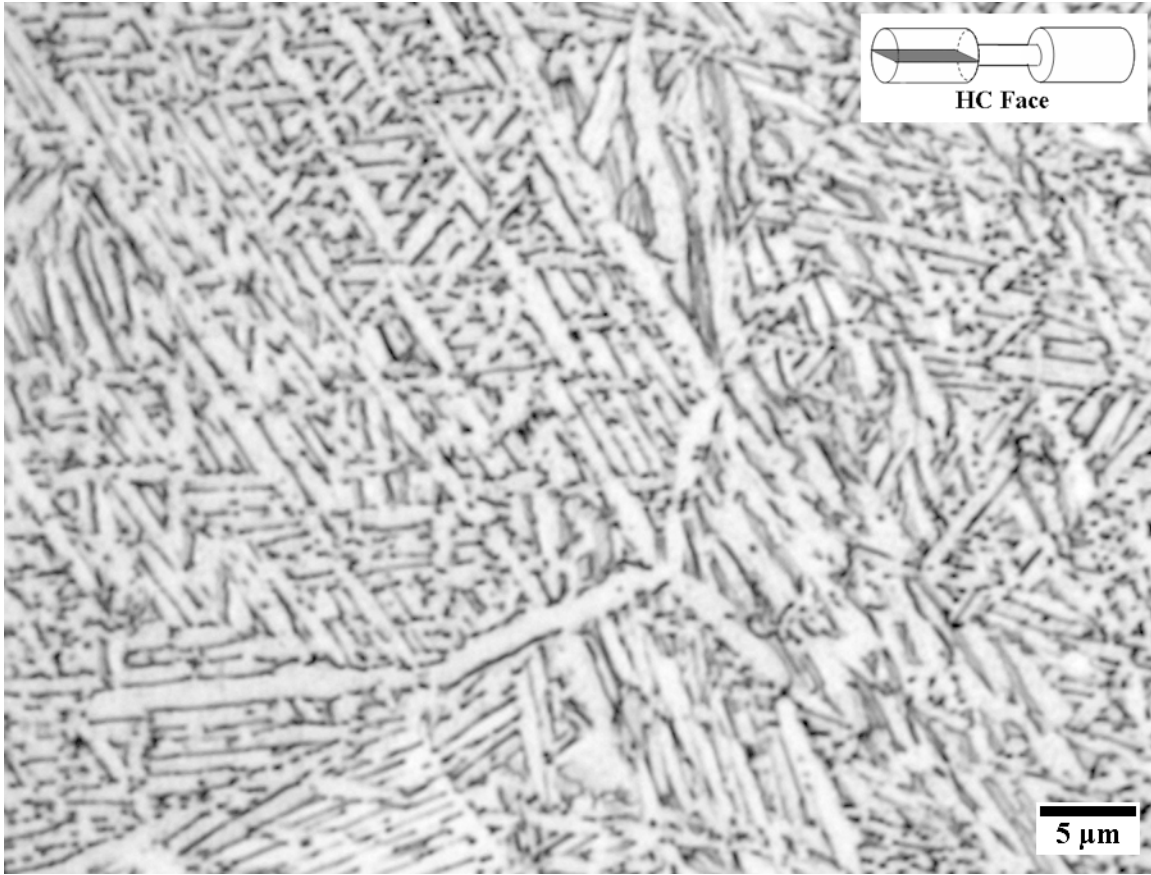


Figure 4.39. Optical micrograph of HC Face (normal to growth direction).

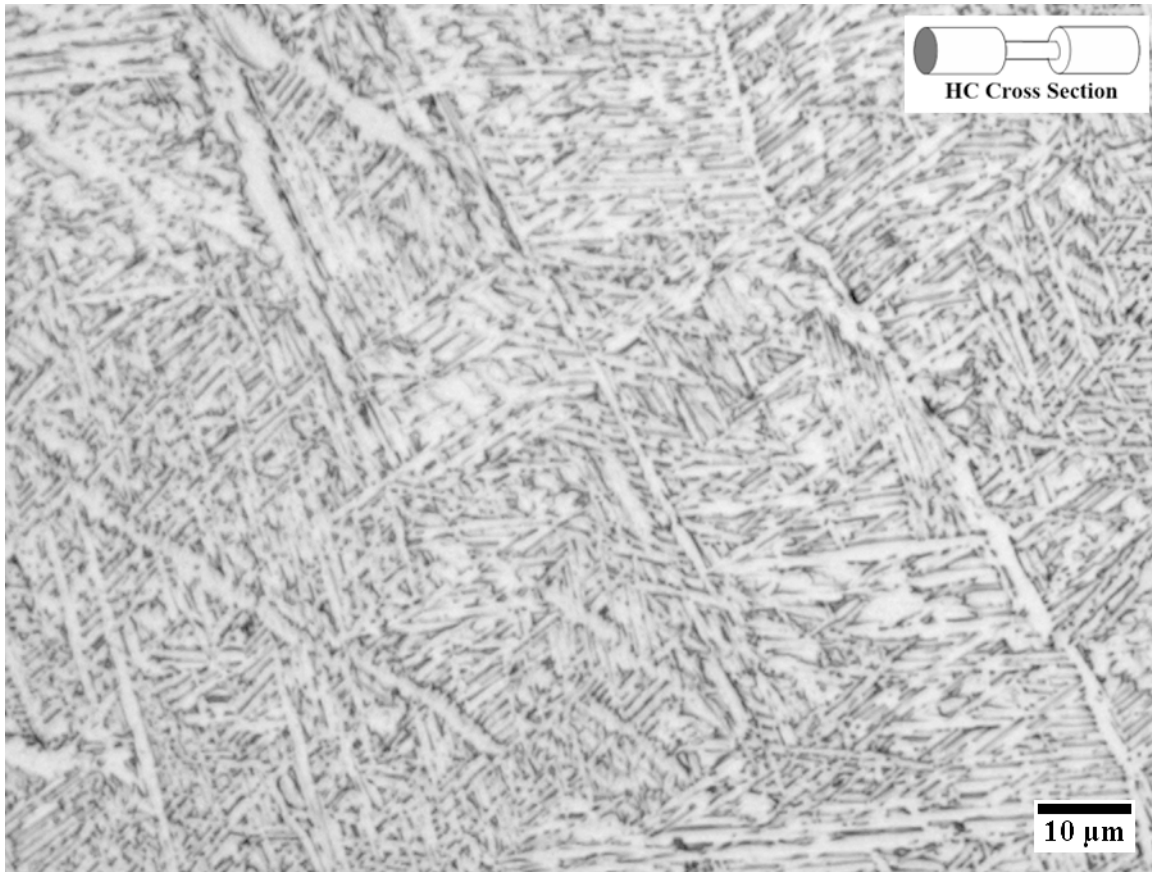


Figure 4.40. Optical micrograph of HC cross section (parallel to growth direction).

Average grain size diameter of prior beta grains is estimated based on the ASTM E 112 standard but should not be considered the absolute grain size due to the extremely long columnar structure parallel to the component growth direction. The grains themselves are difficult to discern and is only reported as an estimate. Grain size is estimated by using the ASTM E 112 intercept method described in Section 3.8 of Experimental Procedure. The number of intercepts per unit length of test line (N_L) is for HC Face is 31.36 which gives a grain size of $G = 7$ when applied to Eq. 3.2. This correlates to an average grain size of 31.8 μm . The average width of the grains is based on several measurements from various fields

perpendicular to the growth direction. The average grain width for the HC sample is 51 μm with a minimum of 9 μm and maximum of 225 μm . The values for prior beta grain diameter and width for samples produced by the Arcam A2 EBM machine along with grain size data for all samples examined are listed in Table 4.4.

Table 4.4. Summary of all grain size measurements for all samples.

Component Type	Average Grain Size (μm)	Average Grain Size (Width) (μm) Normal to Incident Arcam Electron Beam
Forged Turbine Blade	6.7	N/A
Arcam S12 XY	45	62
Arcam S12 XZ	45	63
Arcam A2 HC	32	51

4.4.2. Description of $\alpha + \beta$ Phase Morphology

Figure 4.39 clearly illustrates the Widmanstätten structure of α and β are seen in the Arcam A2-produced component as was observed in the S12-produced components that are consistent with the microstructure that has been documented [1,13,16]. Once again, acicular α is present with retained β phase present between the α phase that has been trapped between the α plates as they grow. There is also discontinuous β seen throughout that may be the result of advancing alpha plate growth characteristic of the rapid solidification that occurs in the Arcam process. The SEM micrograph in Figure 4.41 shows the cellular structure of the HC Face plane and more clearly shows the discontinuous nature of the β phase which appears as the light regions. Alpha phase is the darker areas in the SEM images.

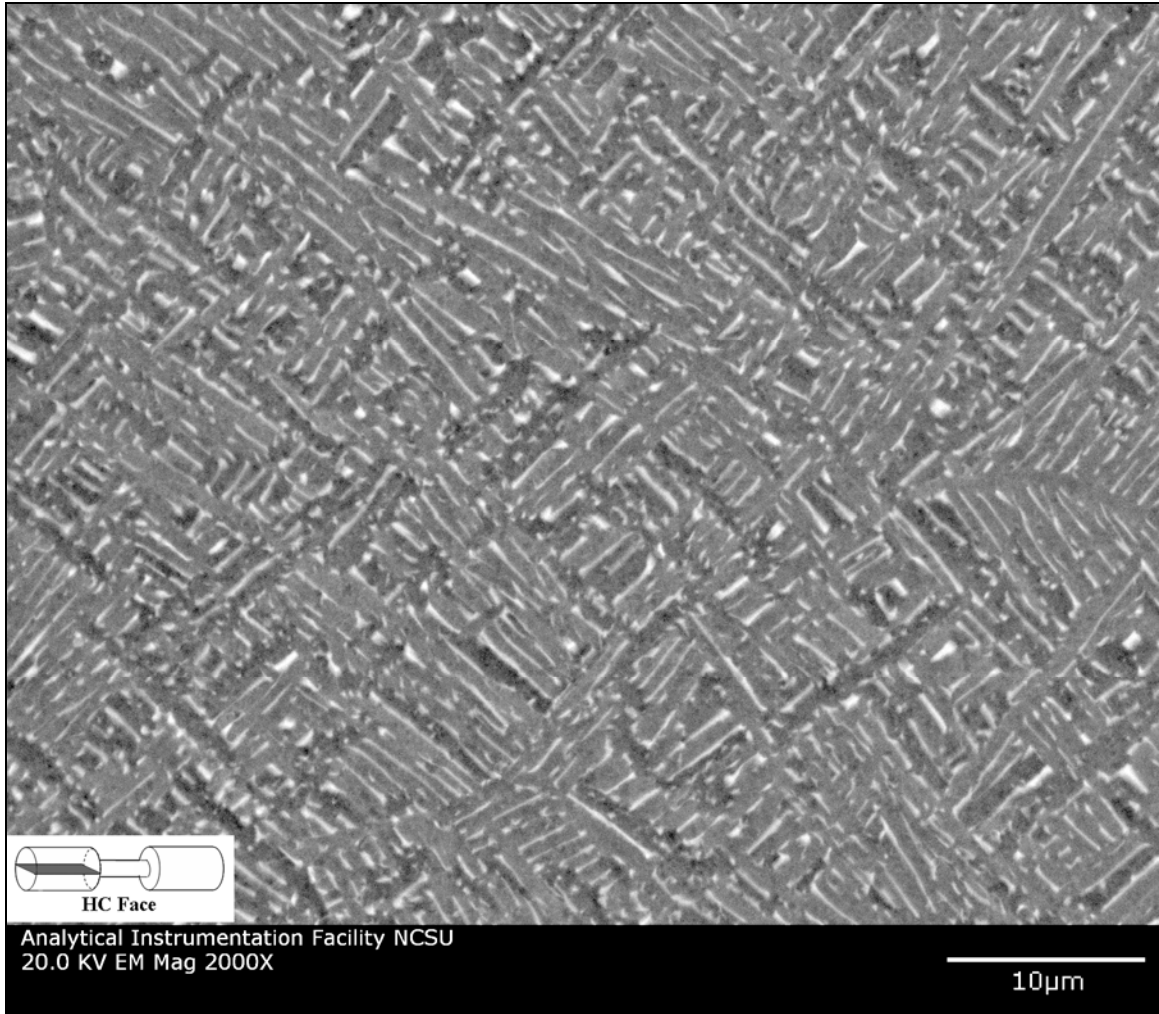


Figure 4.41. SEM micrograph of HC Face.

The SEM micrograph of the HC Cross Section plane in Figure 4.42 shows a portion of the columnar grain structure and also provides further illustration of the Widmanstätten structure. Although the image is oriented such that the growth direction is vertical, a grain boundary is visible diagonally from bottom left to upper right. The interior of the two grains separated by this grain boundary appear to have different crystallographic orientations.

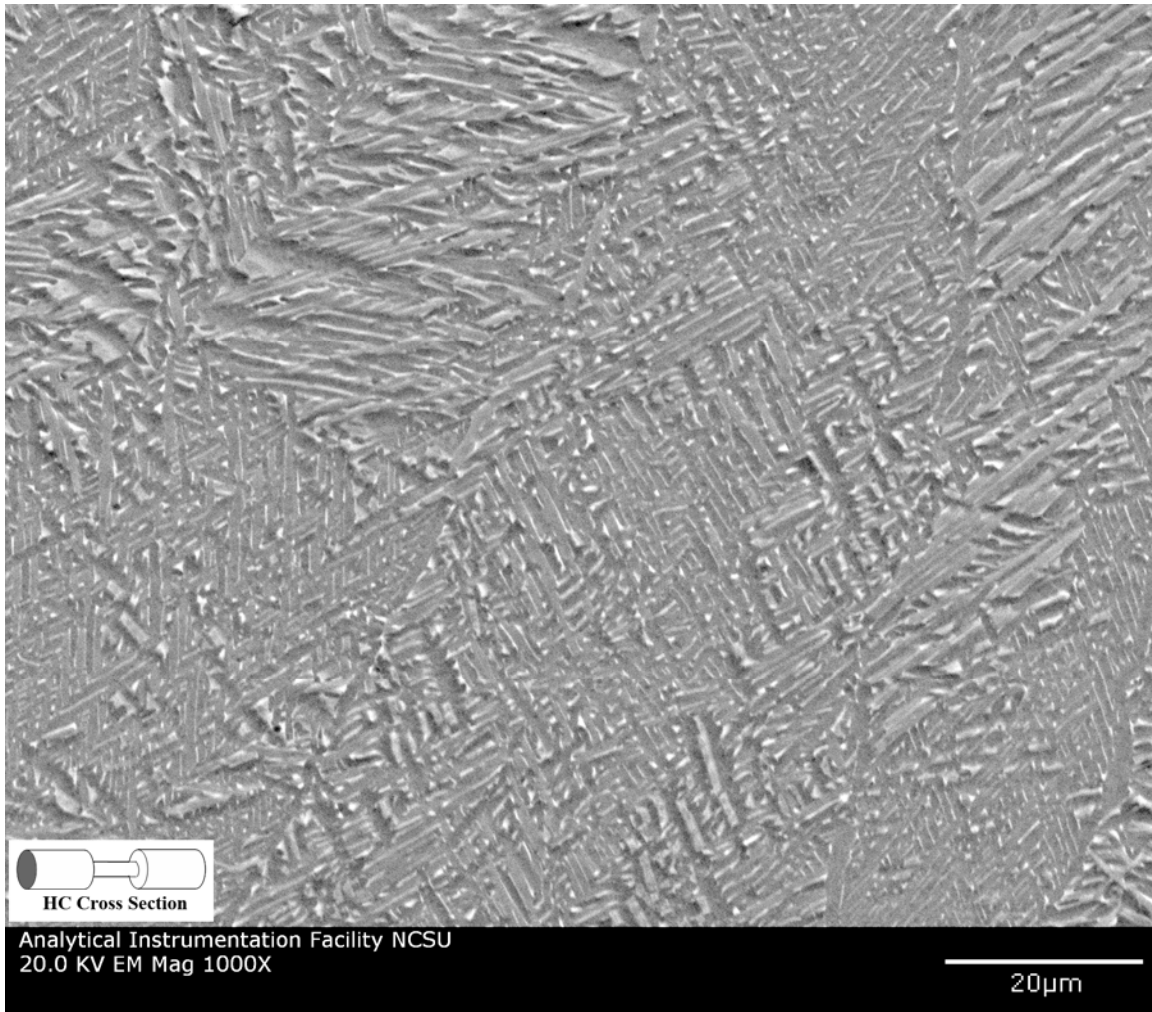


Figure 4.42. SEM micrograph of HC Cross Section.

4.4.3. Volume Fraction of β Phase

The volume fraction of β is measured using by a systematic point count method along the ASTM E 562-08 standard described in Section 3.9 of Experimental procedure. The number of points that fall on the minor phase are recorded. Five optical micrographs were used to calculate the volume fractions of each phase present. The arithmetic average for the volume fraction of beta is 46.9% with a standard deviation estimate of 4.3. The volume

fraction of the beta phase is $46.9\% \pm 5.3$. The relative accuracy for this measurement is 11.4%.

Table 4.5. Summary table for volume fraction of beta phase for all samples.

Component Type	Volume Fraction of Beta Phase (%)	Relative Accuracy (%)
Forged Turbine Blade	27.4 ± 6.3	23
Arcam S12 XY	31.8 ± 3.7	11.5
Arcam S12 XZ	41.6 ± 2.7	6.6
Arcam A2 HC	46.9 ± 5.3	11.4

4.3.4. Transmission Electron Microscopy of S12 - Produced Components

The following section shows the HC orientation components produced by the Arcam A2 EBM machine. The TEM samples in this section were all prepared by electropolishing as described in Experimental Procedure. Figure 4.43 is a bright field TEM image of the HC Face plane tilted to the [5-1-43] zone axis of the α HCP phase. Finer detail of the acicular alpha plates (light regions) can be seen with (darker) beta phase between the alpha sub-grain structures. From looking at diffraction data while performing transmission electron microscopy, it was clear that all of the alpha sub-grains are in the same crystallographic orientation with less than 4° tilt between each sub-grain. The microstructure in this micrograph is most likely the result of beta phase that is trapped as alpha phase nucleates from a prior beta grain boundary from an initially fully beta polycrystalline matrix.

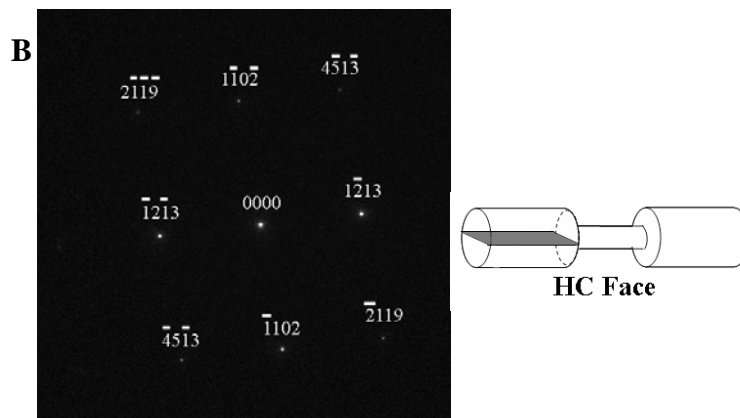
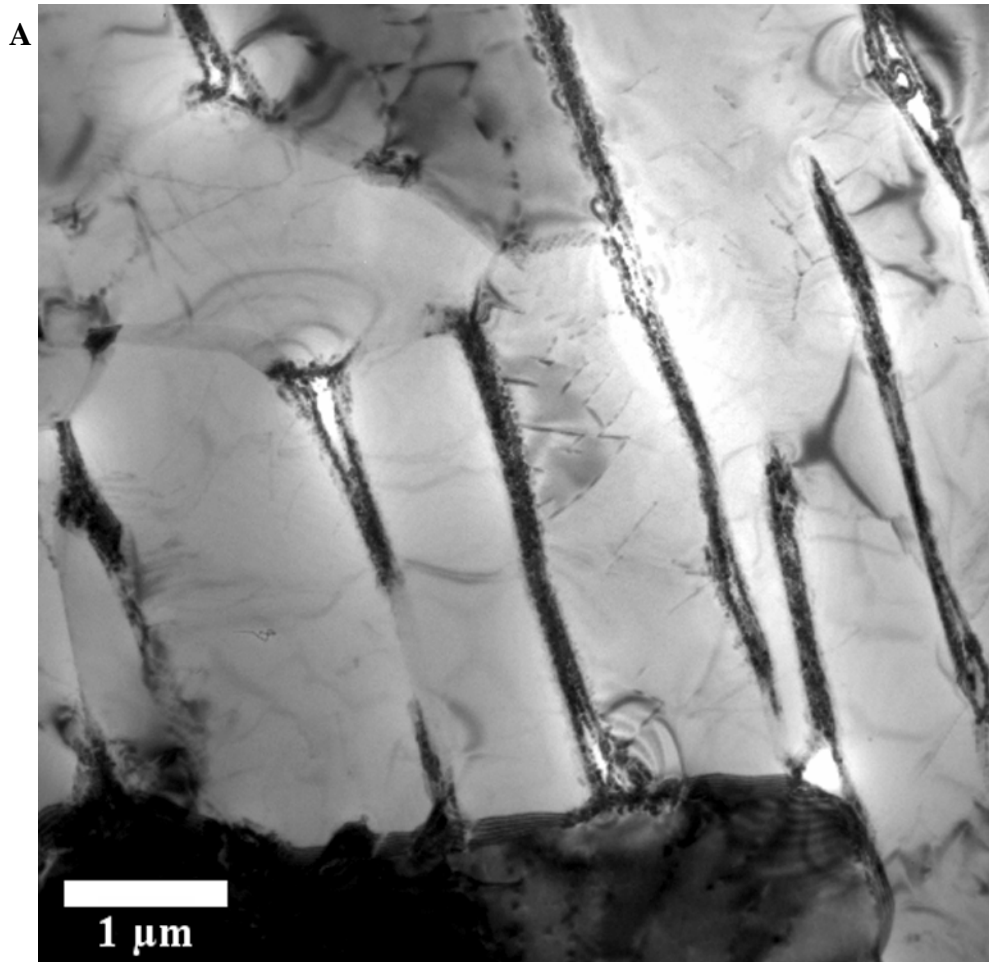


Figure 4.43. a) Bright field TEM micrograph of HC Face and diffraction pattern.

b) Zone axis = $[5\bar{1}\bar{4}3]$.

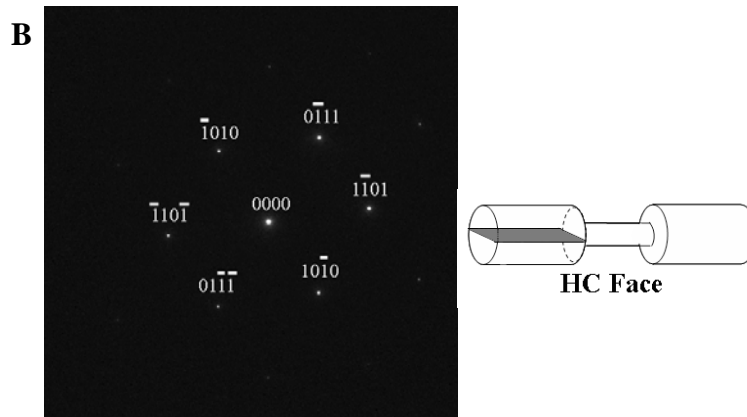
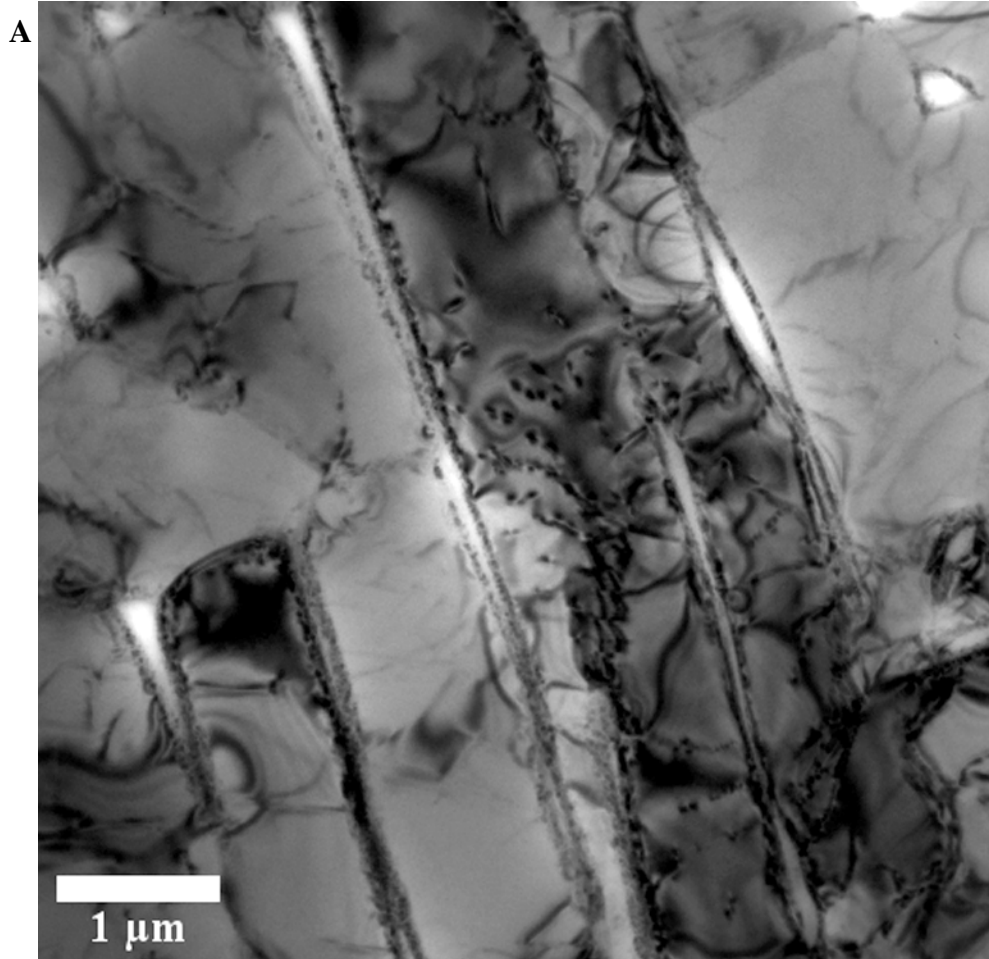


Figure 4.44. a) Bright field TEM micrograph of HC Face and diffraction pattern.

b) Zone axis = $[-12-13]$.

Figure 4.44 is the same sample and region featured in Figure 4.43, tilted in the $[-12-13]$ zone axis. Dislocations are more visible when tilted to this zone although the alpha phase sub-grains are more difficult to examine due to excessive diffraction contrast. This image is therefore complimentary to Figure 4.43.

Figure 4.45 is a TEM bright field micrograph of the HC Cross Section plane tilted in the $[10-11]$ zone axis. The tapered morphology of the acicular alpha platelets can be seen here in addition to dislocations that are present from the sub-grain boundary of the platelet in the lower right area of the image. The dark sub-grain in the lower left region is presumed to be alpha but appears dark from being normal to the incident electron beam which causes strong diffraction contrast.

Another TEM bright field image in HC Cross Section plane is shown in Figure 4.46, which is tilted to the $[01-10]$ zone axis. Alpha and beta phase are labeled accordingly. Dislocations within the alpha phase can be seen located perpendicularly to the beta phases.

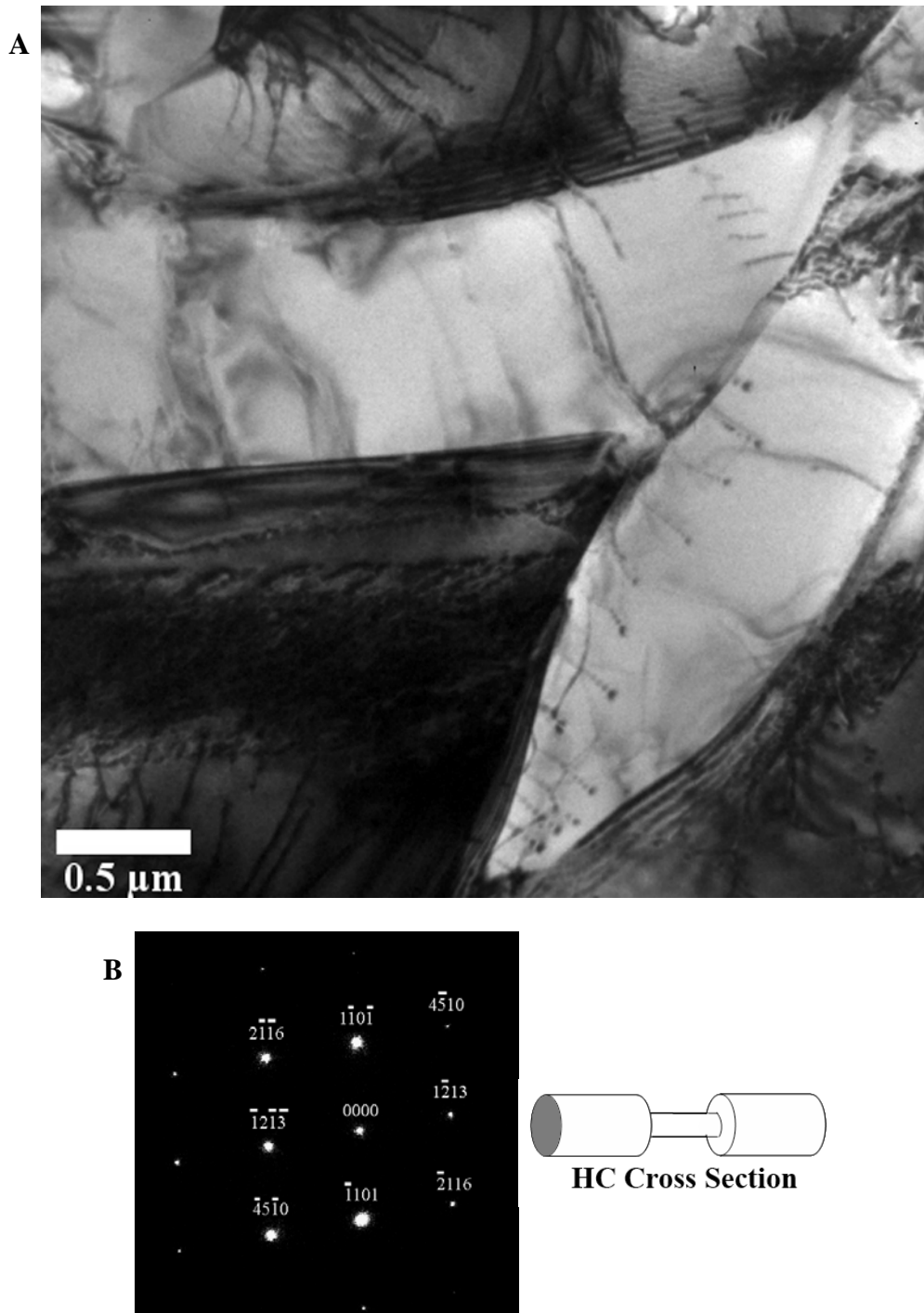


Figure 4.45. a) Bright field TEM micrograph of HC Cross Section and diffraction pattern.

b) Zone axis = $[10\bar{1}1]$.

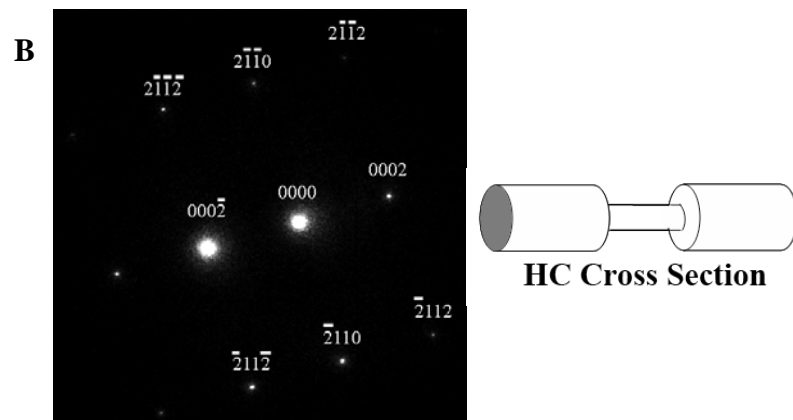
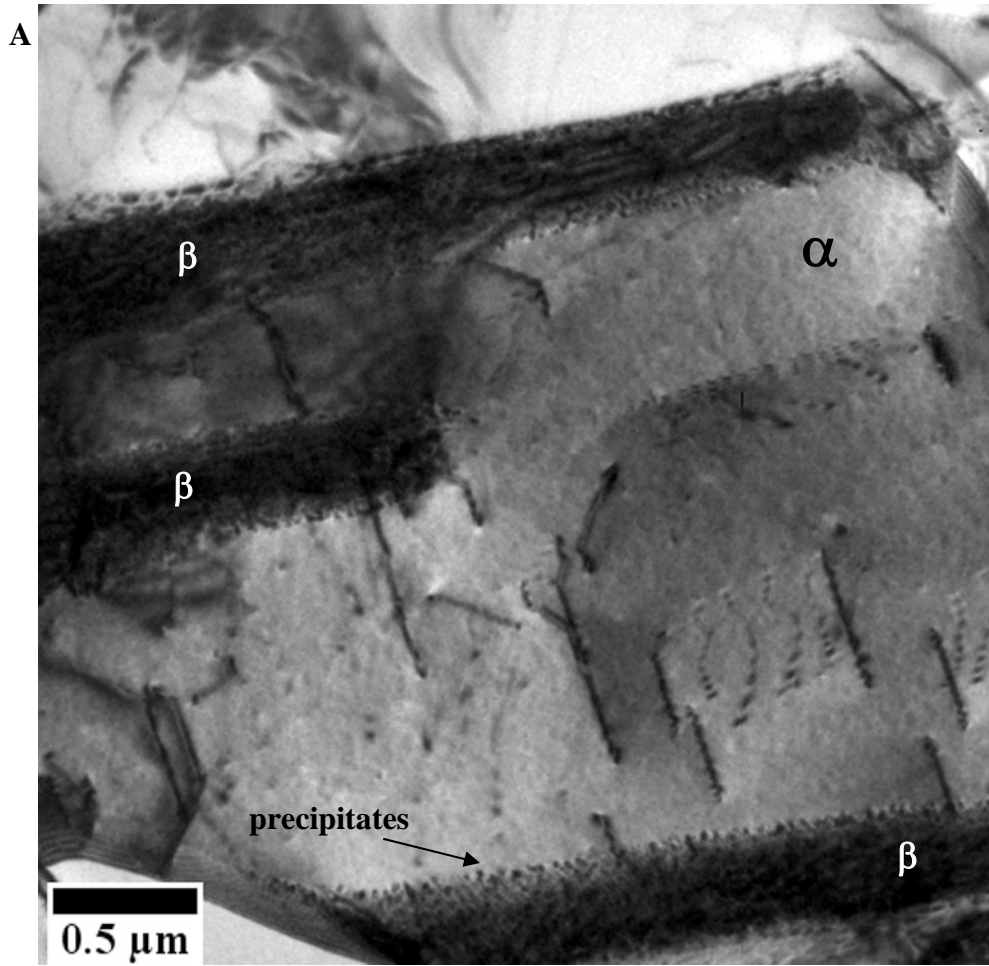


Figure 4.46. a) Bright field TEM micrograph of HC Cross Section and diffraction pattern.

b) Zone axis = $[01\bar{1}0]$.

Figure 4.47 is a higher magnification image of a beta phase region between the alpha phase that closely resembles beta phase that has been reported by Donachie [13] and Servant [26]. The beta phase region is 125 nm wide here. This area would be a prime candidate for further studies of investigating the presence of a face-centered cubic (FCC) crystal structure at the α/β interface as reported by Servant [26]. As seen in TEM micrographs of samples produced by the Arcam S12 EBM machine, the beta phase contains small, roughly spherical spots along the α/β interface in Figures 4.46 and 4.47.

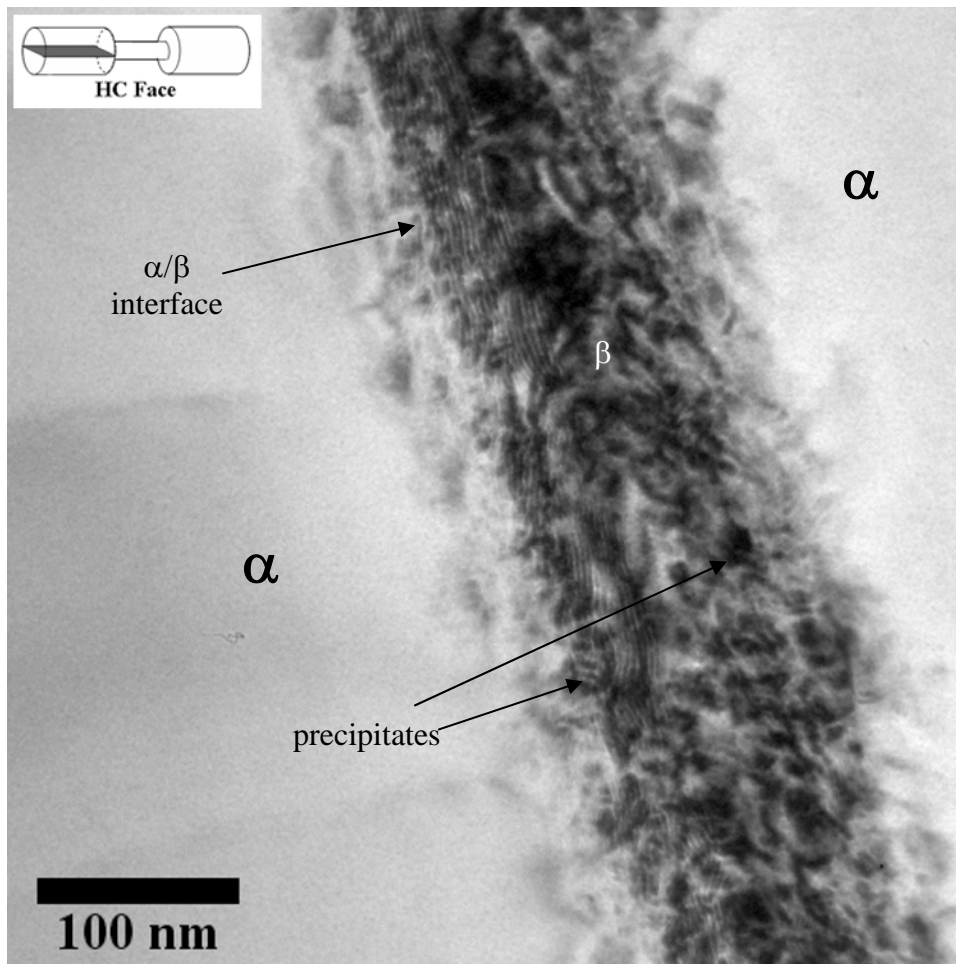


Figure 4.47. TEM micrograph of HC Face, alpha/ beta phase interface region.

4.5. Porosity

Voids were discovered throughout the bulk material in polished and etched samples of components that had been fabricated by Arcam S12 and A2 EBM machines for this study. Macroscopic pores are visible at various locations on optical micrographs in Figures 4.x, y, z, shown previously in Section 4.2. Scanning electron microscopy of these Arcam-produced components provides more detailed, three-dimensional information of the enclosed cavities that are exposed as a result of careful sectioning and polishing. XY and HC Cross Section and Side plane samples are oriented perpendicular to the growth direction, such that the bottom of the image is consistent with the bottom on the component in contact with the build plate.

4.5.1. Porosity of Arcam S12 Components

Figure 4.48 is an optical micrograph taken at the build plate of the XY sample in cross section. Crack-like voids are present at the interface between the unmelted PREP powder and the solid component. Grains structure appears irregular near the build plate. In the XY Cross Section sample of Figure 4.48. Columnar grains begin formation approximately 350 μm away from the build plate. Figure 4.49 is an optical micrograph of the XY Side orientation of the same sample XY sample, at the build plate/specimen interface where it begins growth on the build plate. Unmelted Ti-6Al-4V PREP powder spheres were found at the bottom of the sample. Melt pool overlap areas run horizontally and are visible in the middle of the micrograph.



Figure 4.48. Optical micrograph of XY Cross Section sample near build plate.

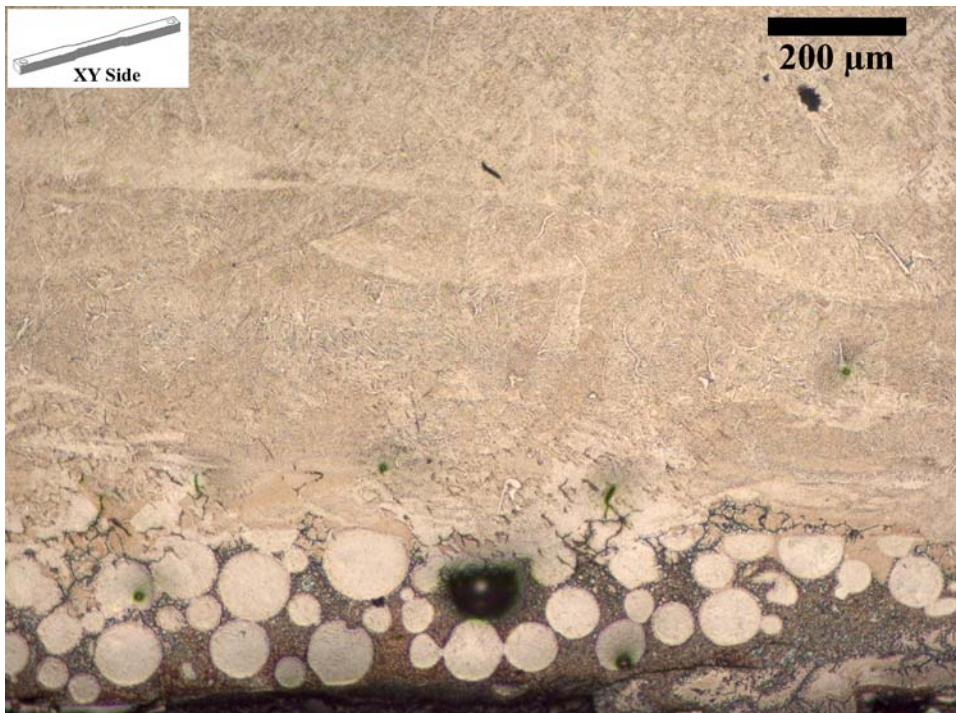


Figure 4.49. Optical micrographs of XY Side sample at the build plate.

AMS 4999 mandates that a tolerance of 760 μm of the exterior surface of a component be machined to the desired net shape. Figures 4.1, 4.5, 4.10, 4.11, 4.13, 4.36, and 4.48 provide information that the Arcam S12 and A2 EBM machines can produce a component that can successfully meet the tolerance requirement without having to machine beyond said tolerance, which minimizes scrap material. The microstructure is consistent beyond 760 μm within the components examined in this study.

The SEM micrograph in Figure 4.50 shows four layers of the XY Side plane near the build plate, as the growth direction is from the bottom of the image upwards. The first distinct melted layer at the bottom of this image has a height of approximately 160 μm and appears to have complete densification in this region. Incomplete melting of precursor material is seen in the next layer along with voids between the 30 to 75 μm diameter alloy powder spheres. A 200 μm long void exists horizontally between the first and second layer. Microstructural consistent with the majority of the component begins to form in the third layer, which is about 300 μm from the build plate.

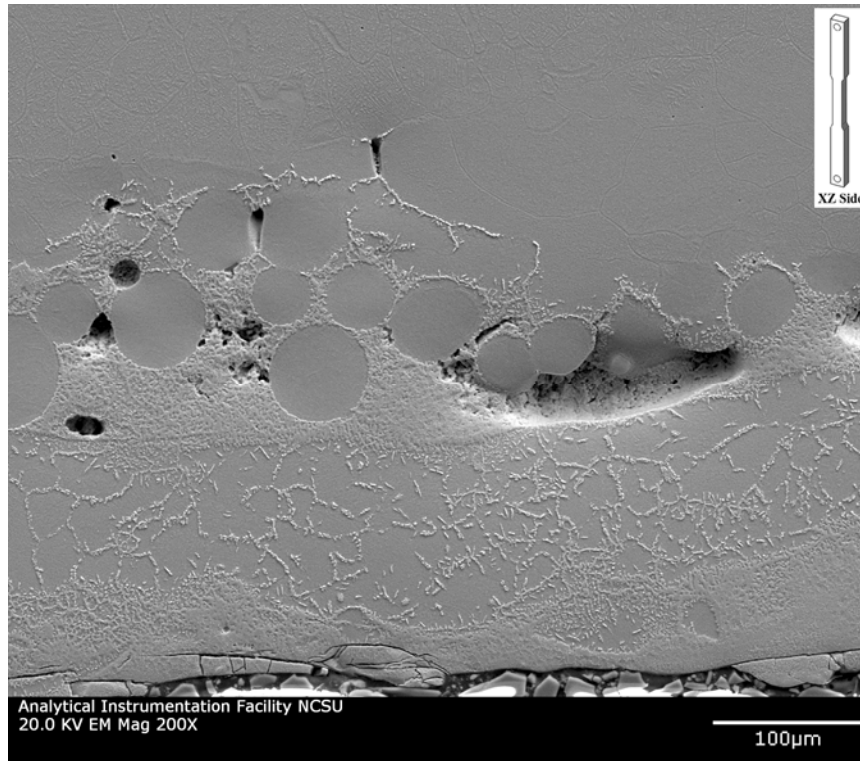


Figure 4.50. SEM micrograph image of XY Side plane near the build plate.

Figure 4.50 is an SEM micrograph of a polished and etched XY Cross Section surface. The void on the left side is 368 μm long by 47 μm at its widest point. Rounded areas such as at the right side of this micrograph are PREP powder spheres that have not been fully melted during processing. Note the sphere visible in the roughly 150 μm by 275 μm wide. The areas around these defects appear to be satisfactorily densified by the melting process. Since these voids are visible from a polished section and depth of the void can be seen, these defects obviously exist in three dimensions.

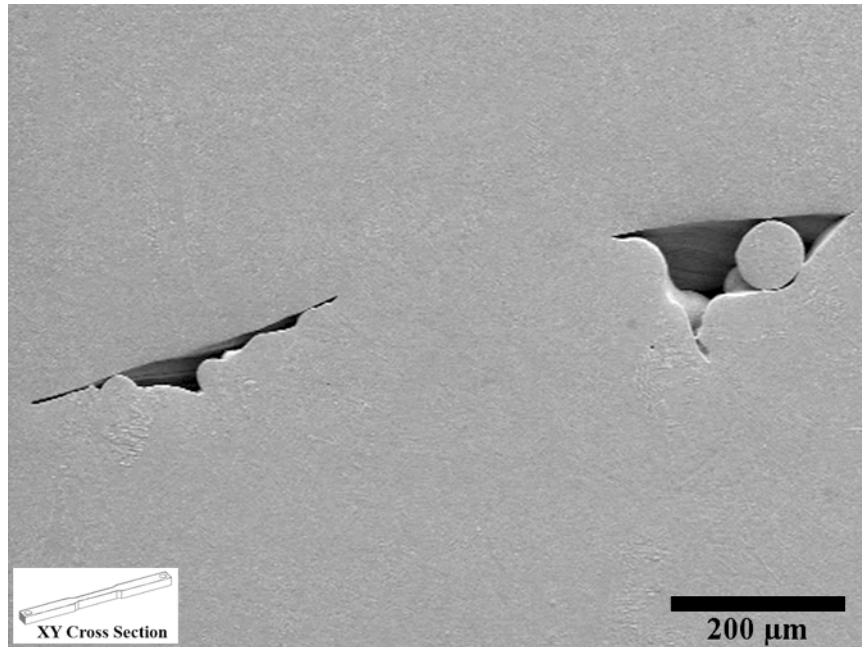


Figure 4.51. SEM micrograph image of XY Cross Section illustrating component fabrication defects.

Figure 4.52 is an image of the void on the right side of Figure 4.51. Incomplete melting of the 70 μm diameter sphere shows evidence of partial sintering but has clearly retained its initial shape. Other spheres can be seen to have only partially melted into the bulk component. The large gap which could easily accommodate additional PREP powder particles, suggests that inefficient particle packing is a problem prior to the application of the Arcam electron beam.

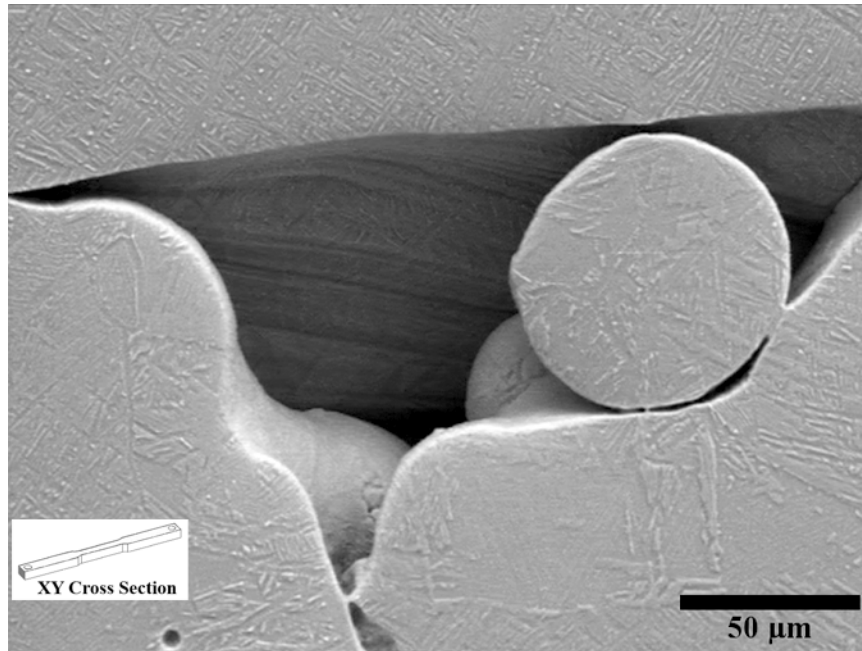


Figure 4.52. Increased magnification SEM micrograph of XY Cross Section illustrating component fabrication defect from Figure 4.51.

The microstructure in the area in and below the void appears different than that of the adjacent material seen above the void line, leading to the suggestion that sufficient heating is not occurring. Explanations of this lack of melting could involve variation in the electron beam energy or lateral velocity and/or lack of powder in the volume due to inefficient packing or supply. Figure 4.53 shows another region on the same XY Face sample where incomplete melting is observed. In this image, the void band width ranges from 105 μm on the left to 140 μm on the right. From the close proximity of the spheres, initial particle packing looks reasonable and the spheres are partially sintered to the surrounding regions but they have retained their original shape. Increased power input, controlled by the beam current

(i_b) by the condenser lens strength may be necessary in addition to the appropriate lateral beam velocity (V_B) to completely melt all PREP alloy powder throughout the component during the build.

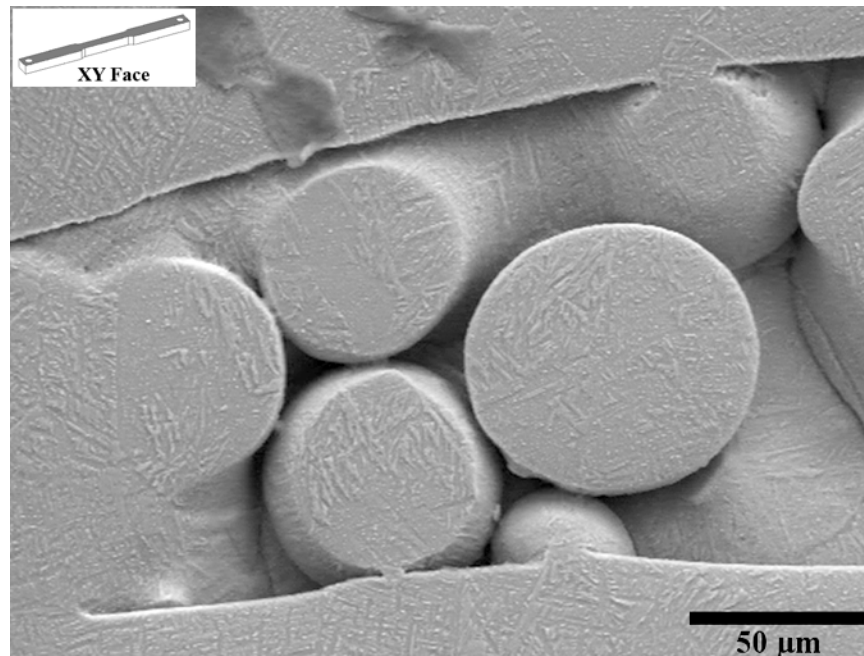


Figure 4.53. SEM micrograph images of XY Face illustrating incomplete packing and sintering defect.

Details of the lower right region of the void in Figure 4.53 are shown below in Figure 4.54. Based on the diameter of the sphere located in the top right of Figure 4.53 (top left of Figure 4.54) the depth of this void is at least 50 μm . Presence of alpha at a prior beta grain boundary can be seen on the surface and extending into the void region (see arrows).

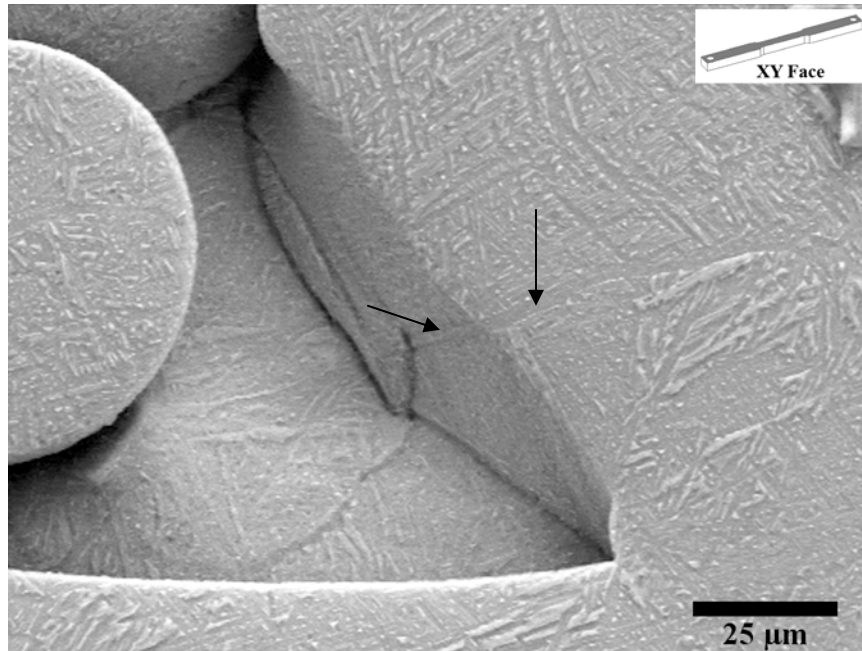


Figure 4.54. Increased magnification SEM micrograph of XY Face illustrating component fabrication defect from Figure 4.53. Arrows show alpha grain boundary.

The defect in Figure 4.55 exists between two melted layers in the cross section plane of the XY sample. Component growth orientation is from bottom to top of this image. The void on the left is 100 μm in length and 9 μm in height. The void in the center of the image is 37 μm in length by 14 μm in height. Columnar grain growth is disrupted in the area between these two main voids and equiaxed grains are observed above the layer interface. Voids of this nature between melted layers are observed in many other areas throughout Arcam-produced components. The velocity of the Arcam electron beam may be traveling too rapidly to allow for the flow of material.

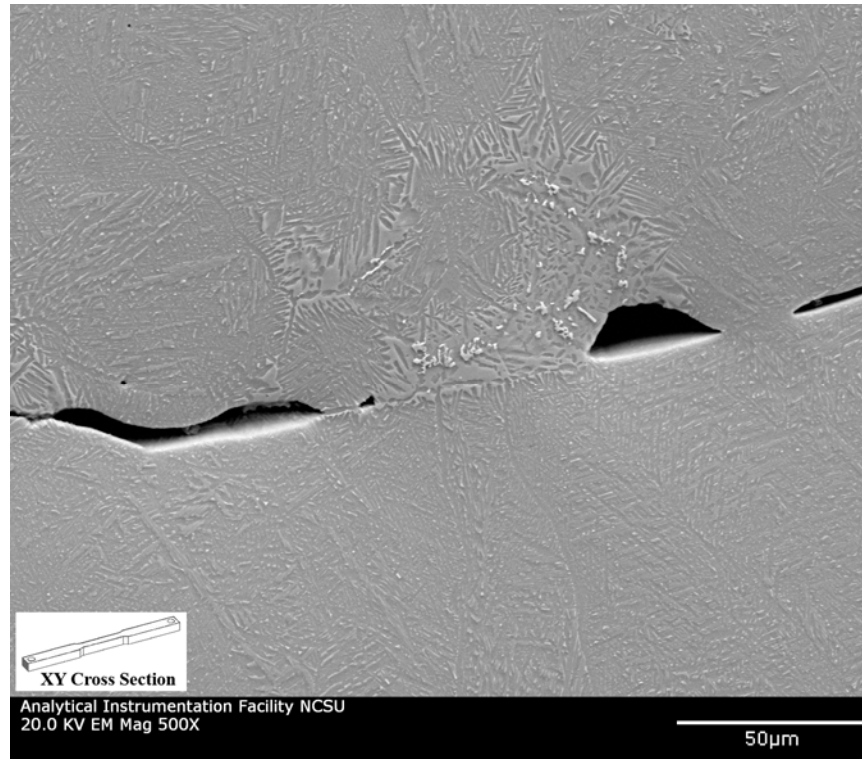


Figure 4.55. SEM micrograph of XY Cross Section.

Unmelted regions such as those observed in the XY sample where the starting material spheres are discernable were not observed as frequently in the XZ sample. Pores of spherical shape were observed. The SEM micrograph in Figure 4.56 is representative of the defects present in the XZ sample grown in the Arcam S12 unit. The largest pore in this image is 60 μm across. Pore dimension have been seen to be as large as 250 μm at the particular cross sections examined. A series of cross sections would be necessary to correctly characterize the average pore size. Although the bar geometry is the same, the profile in the growth (z) direction of the XZ sample is much smaller than that of the XY sample. The compact profile may allow for more complete melting and flow of molten alloy at if one

layer of each bar in the build tank is addressed at one time by the electron beam as opposed to the electron beam having to travel the entire distance of the tensile bar in the XY orientation.

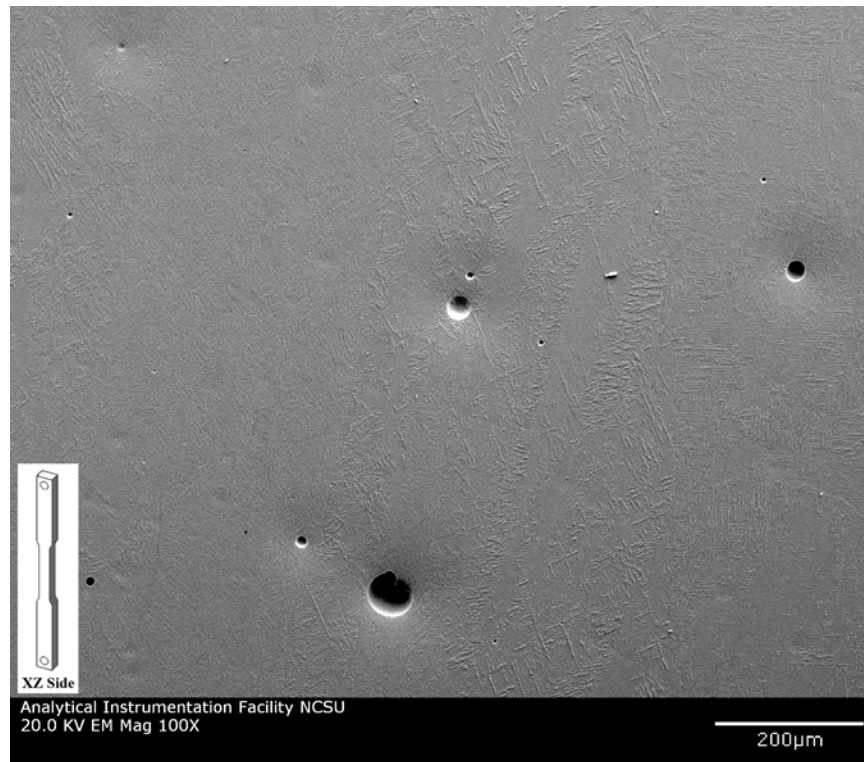


Figure 4.56. SEM micrograph of XZ Side.

Although the XZ sample grown in the Arcam S12 did not have the unmelted powder issue that was present in the XY (S12) and Horizontal Cylinder (A2) (see following section), there was no advantage in terms of mechanical properties according to Bass [6]

4.5.2. Porosity of Arcam A2 Component

A severe amount of porosity is observed in the following SEM micrographs of the horizontal cylinder tensile bar grown in the Arcam A2 EBM machine. Figure 4.309 shows several defects within one location on the Face plane of the horizontal cylinder. Component growth for the HC Face plane is normal to the plane of the page. These defects are over 200 μm in size in some areas. Incomplete melting of the starting material was observed as well as large areas where the pre-alloyed powder was completely absent. The tapered, alternating patterns of the defect areas in Figure 4.57 running horizontally were consistent with the melt pool morphology seen on the exterior of the XY sample in Figure 4.1. The widths of the patterns seen here are related to the Arcam electron beam pass, which are between 200 and 250 μm . Controlled by scan coils, the Arcam beam follows an equilateral triangular hatching pattern with distances of approximately 100 μm as it moves laterally across the powder bed.

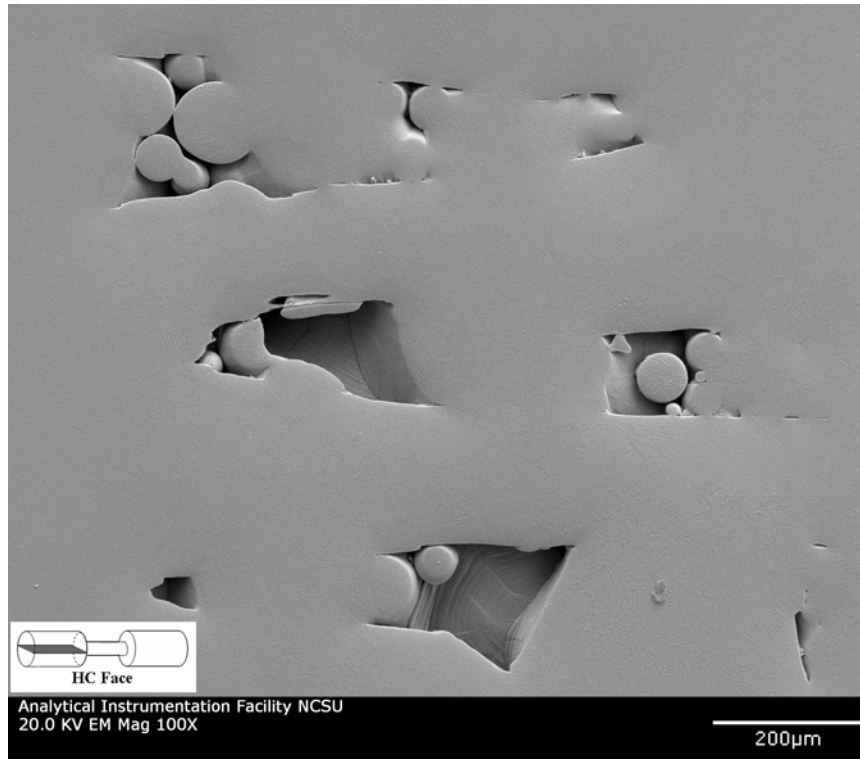


Figure 4.57. SEM micrograph of HC Face.

Another exceptionally large area of unmelted PREP powder in the Face plane of the HC sample is shown below in Figure 4.58. In this region, partial melting and extensive sintering of the alloy spheres has taken place but there are several spheres, which have retained their original dimensions. The size of the large defect on the left side of Figure 4.58 is 0.9 mm in diagonal and 0.42 mm across. On the right side of this image, a single unmelted of 75 μm diameter sphere can be seen inside a void. The arrow in this image points to a pore that may be a result of pre-existing porosity within the starting material.

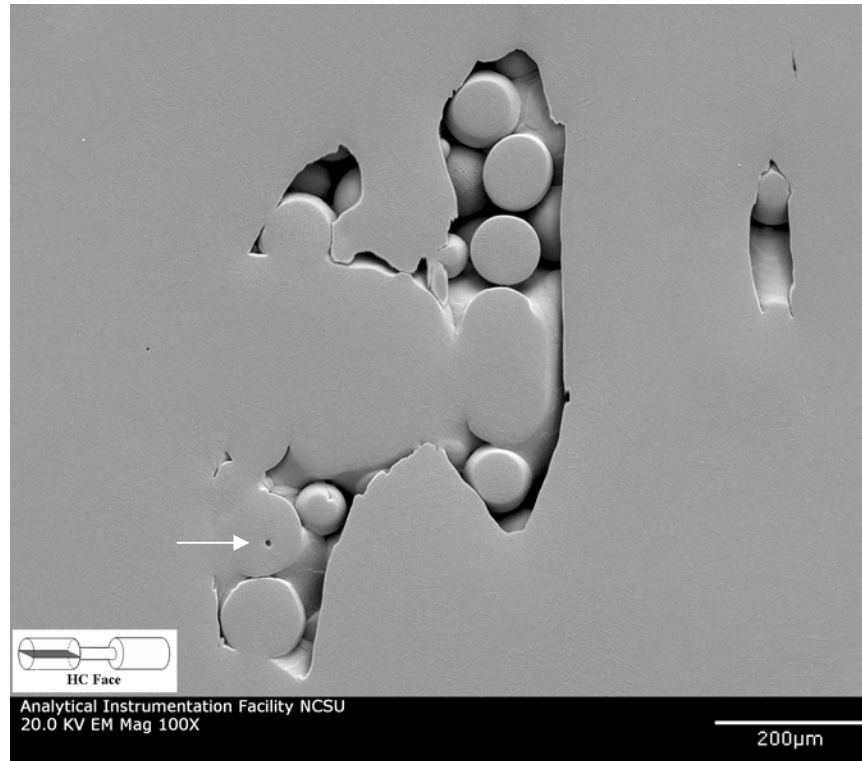


Figure 4.58. SEM micrograph of defects in HC Face plane.

The SEM micrograph in Figure 4.59 is another enclosed defect in the Face plane of the HC sample. Diameters of the two incompletely melted alloy spheres visible in this image are approximately 35 μm and 85 μm . Void dimensions for the region shown is 162 μm wide by 115 μm in height. Unlike the incomplete melting in the defect in Figure 4.58, where particle packing appears sufficient, inefficient particle packing is observed in the void shown in Figure 4.59 due to the absence of spheres in this void. Figure 4.57 also shows two regions that do not show any evidence that alloy powder had been present in the layer prior to melting with the Arcam electron beam.

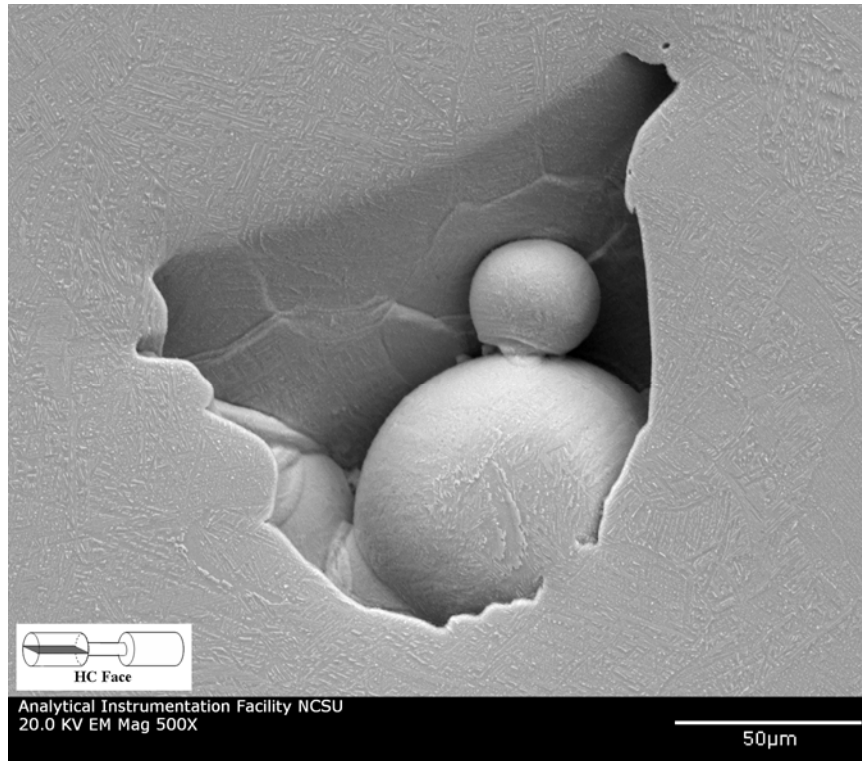


Figure 4.59. SEM micrograph of defect in HC Face plane.

The remaining scanning electron micrographs in this section are representative of voids found in the Arcam A2-by examination of the HC Cross Section plane. Component growth is in the plane of the page from bottom to top and samples are oriented accordingly. The following low magnification micrograph shows several voids located at various depths within the component. Figure 4.60 shows 2.25 mm of the sample height in cross section, which represents up to four layers of component growth from the layer band data taken from Figure XX. Void sizes in this region up to 250 μm across and 100 μm in height are present.



Figure 4.60. SEM micrograph of HC Cross Section.

Gas pores (located top right and lower left) and incomplete melting defects are visible in the HC Cross Section plane shown in the SEM micrograph Figure 4.61. Incomplete melted regions clearly exist at multiple layers in this region of the sample. The powder spheres have retained their original shape in this defect. The large void on the lower right area is 130 μm in height and in excess of 450 μm wide.

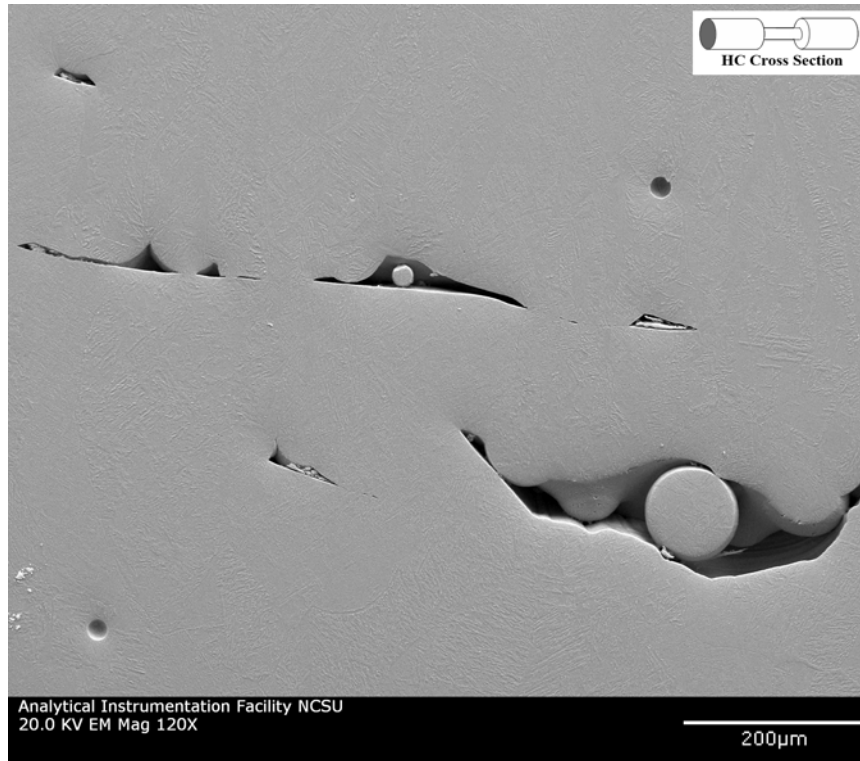


Figure 4.61. SEM micrograph of HC Cross Section.

The void in Figure 4.62 is from the HC Cross Section plane and is typical of the defects seen throughout Arcam-produced Ti-6Al-4V components from the Arcam S12 and A2 machines. This void measures 77 μm in height by 203 μm wide. Depth of this defect is at least equal to the diameter of the 66 μm unmelted alloy sphere.

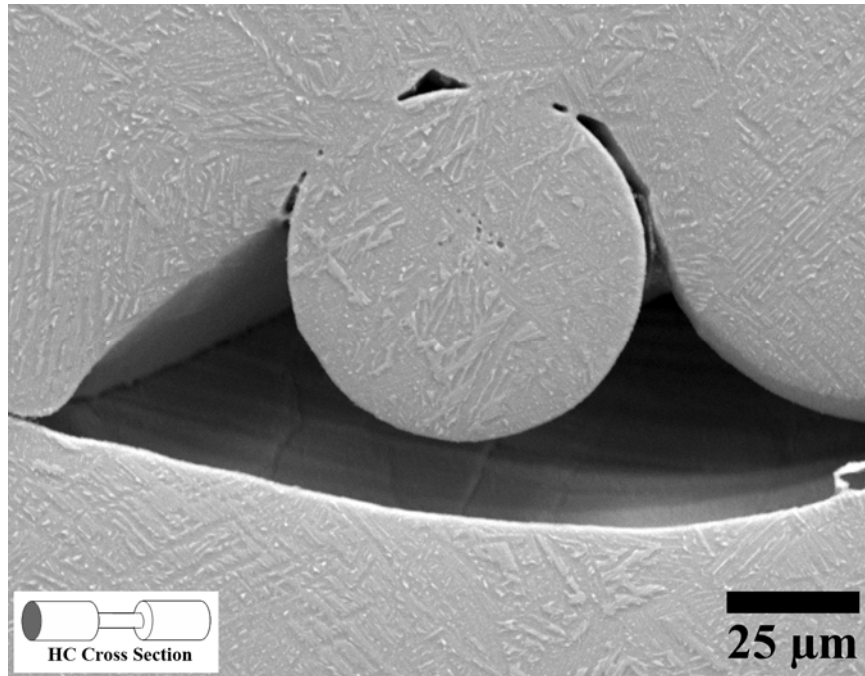
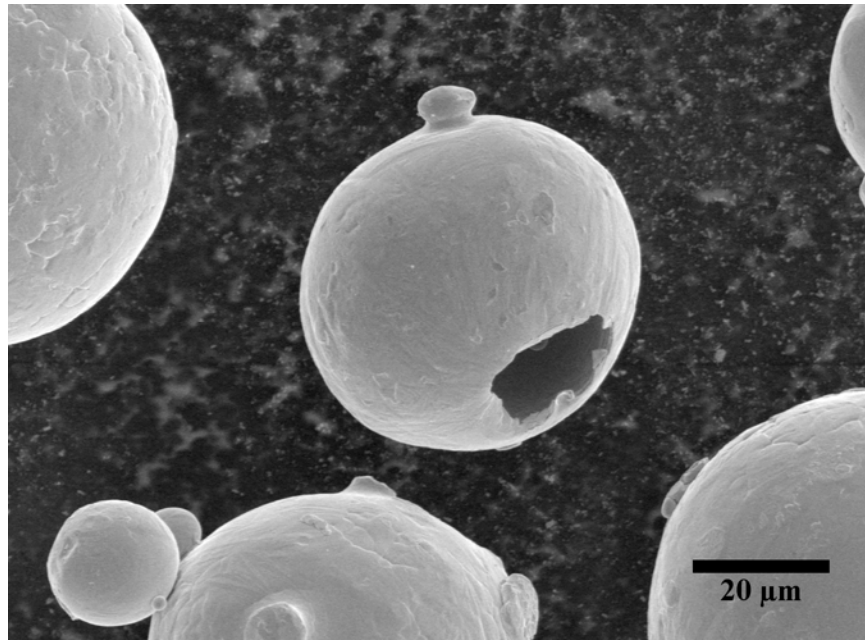


Figure 4.62. SEM micrograph of HC Cross Section.

Small pores exist within the center of 66 μm alloy sphere particle above and were seen in other unmelted spheres that reside in the bulk material. These pores are miniscule compared to the larger voids but may contribute to the entrapped gases that form the larger spherical pores that are observed in all samples and/or are a result of elemental losses through vaporization during melting. These smaller pores initially present in the PREP powder could combine when fully melted, yet are trapped due to the rapid solidification.

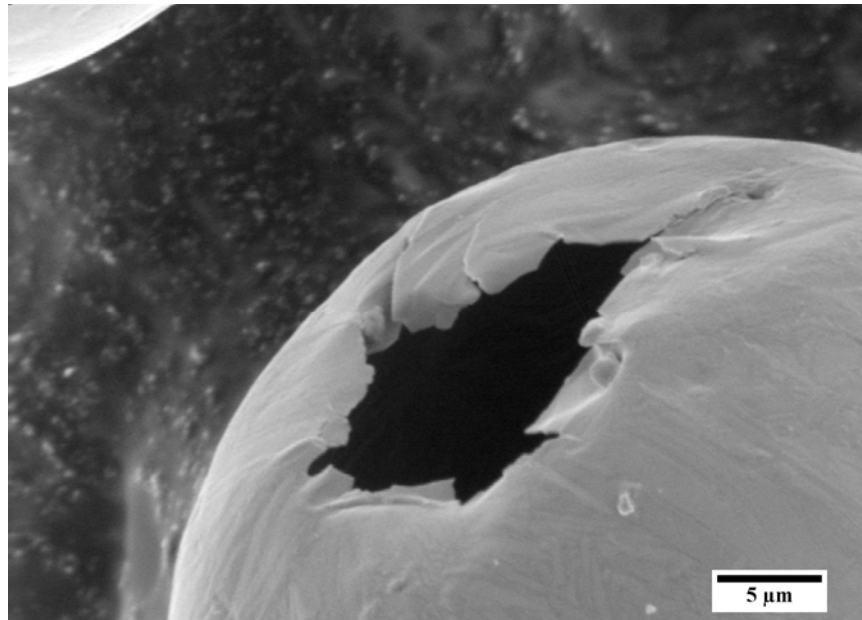
4.5.3. Porosity and Aggregation in PREP Powder

From SEM micrographs of the pre-alloyed PREP powder it is clear that some of the alloy spheres contain pores as-received or are semi-hollow as seen below in Figures 4.63 and 4.64.



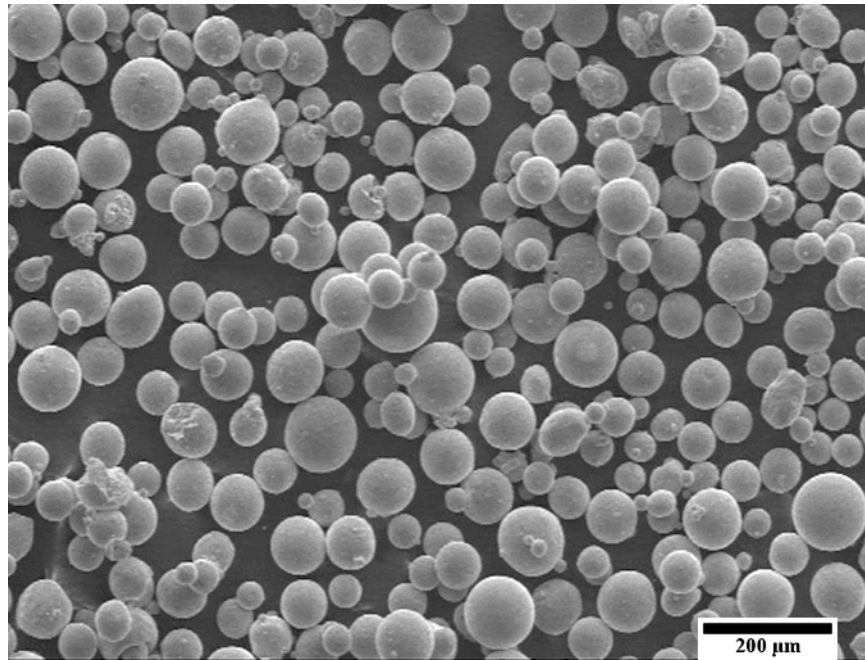
Figures 4.63. Semi-hollow Ti-6Al-4V PREP powder particle.

The SEM micrograph in Figure 4.64 shows the detail of a Ti-6Al-4V semi-hollow powder sphere with an opening that is approximately 20 μm across.



Figures 4.64. Ti-6Al-4V PREP powder showing porous particle.

No mechanical compaction or vibration of the alloy powder bed is applied prior to the application of the Arcam electron beam. The alloy spheres were found to agglomerate prior to being deposited as seen in low-magnification SEM micrograph of Figure 4.65, which can inhibit particle packing. The agglomerated clusters may contribute to intrinsic porosity of Arcam-produced components by preventing even distribution of particles on a previously melted layer as may be the case in Figures 4.61 and 4.62. Additionally, agglomerated powder clusters will be taller than 100 μm in height when applied to the previously melted layer of the solid object being built and powder particles of diameter larger than 100 μm were observed. If the build height for each layer is in fact 100 μm , the powder particles larger than 100 μm could inhibit uniform powder distribution on a build layer by being pushed through the fresh powder layer by the rakes that provide the spreading action.



Figures 4.65. Ti-6Al-4V PREP powder showing agglomerated particles.

If unmelted PREP powder from previous builds is collected and returned to the powder supply hopper due to its high cost, the agglomerated powder should be filtered and / or sonicated to minimize inefficient packing upon spreading powder subjected to heat back onto the build plane.

Dinda et al. make no mention of such porosity problems in the fabrication of scaffolds from Ti-6Al-4V using a DMD system [1]. In the study performed by Murr, et al using an Arcam EBM S400, pores resulting from particles that were not melted were observed yet reported to be rare [16]. No observed porosity was document by Bass [6] or Ervin [15] in prior Arcam studies.

4.6. Transmission Electron Microscopy Sample Preparation

Two methods of sample preparation techniques were used to produce electron transparent samples for TEM and STEM in this study; twin-jet electropolishing and focused ion beam (FIB). The presence of porosity in the bulk components produced by the Arcam EBM process prevented early attempts at obtaining electron transparent samples by electropolishing. The substantial number and size of the pores grossly affected the ability to achieve samples appropriate for TEM because the electropolishing process was halted once perforation occurred when jet-polishing the 3 mm disks. FIB was used as a complimentary and alternate method and to avoid zero sample production success rate due to porosity.

4.6.1. Electropolishing

As introduced in Experimental Procedure, TEM samples are discs 3 mm in diameter that have been sectioned from the bulk material and are mechanically thinned and polished prior to electropolishing. Figure 4.66 is an optical micrograph of an XY Cross Section TEM sample in progress that has been mechanically polished on one side using the same sequence of SiC paper from 180 through 1200 grit with a final polish of 1.0 μm aluminum oxide slurry. The image of the sample is captured with the eyepiece exposed to the room lighting of the laboratory. The reflection of the laboratory ceiling verifies the mirror-finish, high quality of the final polishing step prior to electropolishing. The reflection of the ceiling tiles are straight shows that the surface is smooth and uniformly flat. Its thickness at this stage is

in the range of 0.2 to 0.5 mm. The sample is shown mounted on a stainless steel cylinder used for precision grinding and polishing in conjunction with the Gatan 623 Disc Grinder. The irregularity on the bottom of the 3mm disc is the exterior edge of the XY tensile sample in Figures 4.66 and 4.67.



Figure 4.66. 3mm disc XY Cross Section Ti-6Al-4V TEM sample in progress.

Pre-existing porosity in the bulk material is evident in the 3mm disc intended for TEM sample preparation via electropolishing in Figure 4.67. Macroscopic voids appear as white spots in the optical micrograph in Figure 4.67 which is an image of the same XY Cross Section sample shown in Figure 4.66 but with limited lighting, making it possible to observe the voids.

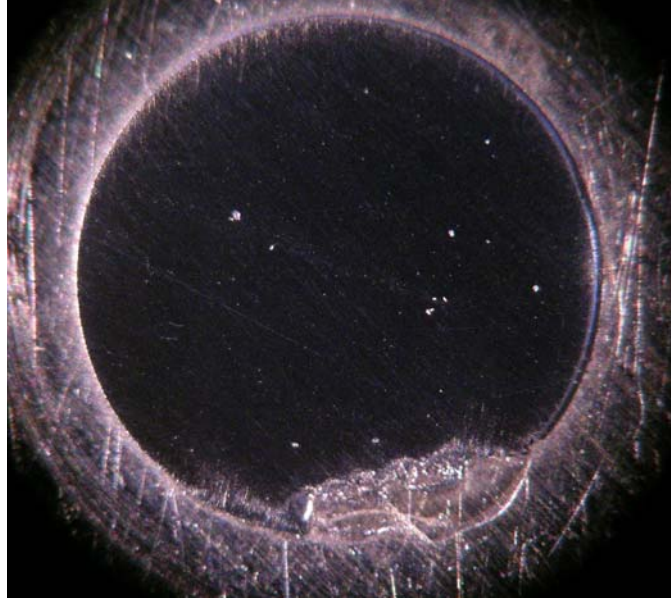


Figure 4.67. 3mm disc XY Cross Section Ti-6Al-4V TEM sample in progress. (Same sample in Figure 4.66)

Figures 4.68 and 4.69 are optical micrographs show the same XY cross section sample after electropolishing with the same lighting conditions used in Figures 4.66 and 4.67 respectively. In Figure 4.3 a relatively good electropolish has been achieved since acceptable light reflectivity is present with only slight pitting, which appears as the diffuse white ring at the edge of the center of the sample that is exposed to the electrolytic solution during electropolishing. Perforation has occurred prior to achieving electron transparency, shown by the arrow in Figure 4.68.

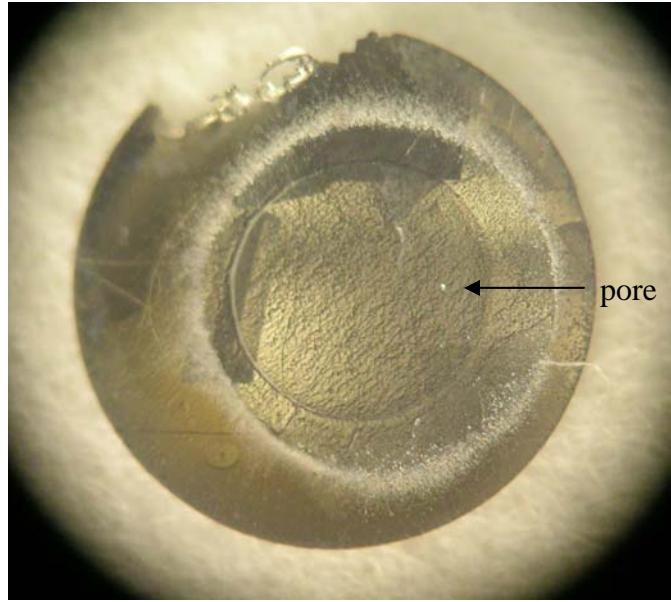


Figure 4.68. Electropolished XY Cross Section Ti-6Al-4V 3mm disc TEM sample.

The grain structure is visible following electropolishing, running east - west in Figure 4.69. The build layer bands are also visible, which are orthogonal to the grains.

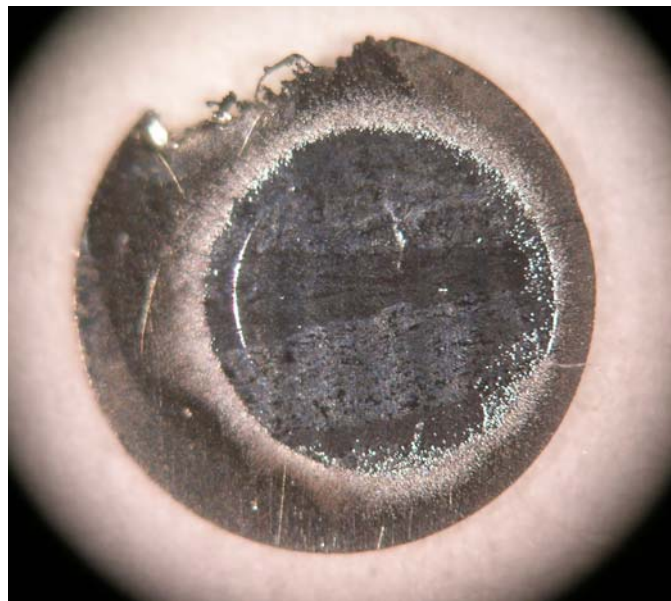


Figure 4.69. Electropolished XY Cross Section Ti-6Al-4V 3mm disc TEM sample.

The low magnification optical image of a different XY Cross Section electropolished TEM sample in Figure 4.70 has a large pore that is circular in shape, which is indicative of a gas bubble that was entrapped at the layer of material to be thinned to electron transparency. This image was captured with the same lighting conditions as those used for Figures 4.66 and 4.68 which show that an acceptable polish has been achieved, although electron transparency has not been achieved. A decent reflection of the laboratory ceiling proves that the quality of the electropolishing procedure is acceptable. Figure 4.71 is an image of the same XY Cross Section sample with the same lighting as used for Figures 4.67 and 4.69 that allow the pore to be seen more clearly.

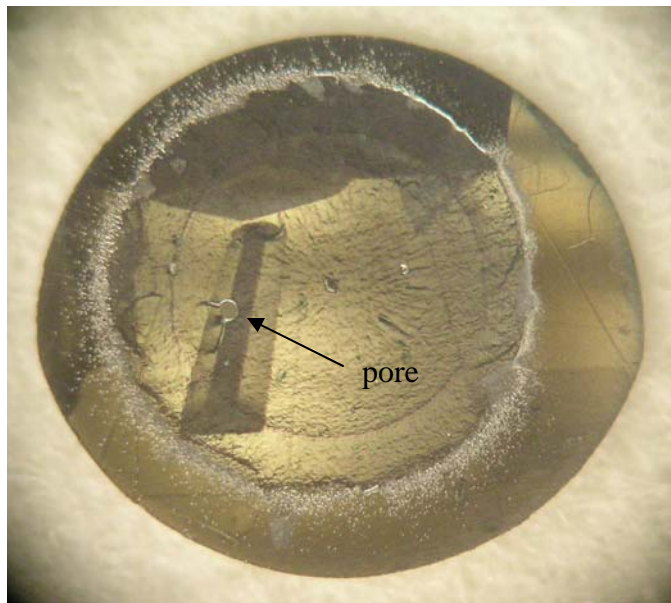


Figure 4.70. Electropolished XY Cross Section Ti-6Al-4V 3mm disc TEM sample.

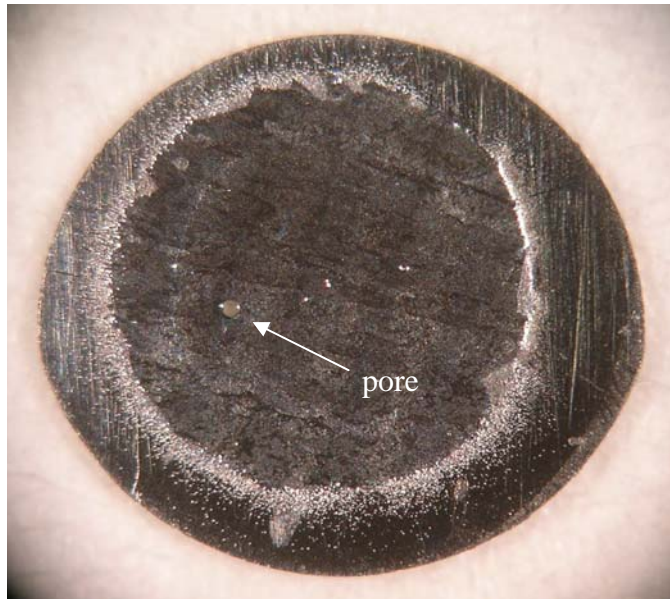


Figure 4.71. Electropolished XY Cross Section Ti-6Al-4V 3mm disc TEM sample.

The SEM micrograph shown in Figure 4.72 is a secondary electron image of the pore shown in Figure 4.71. The electropolishing process ceases when perforation occurs in the sample, in this case on a pore site. The region at the inner edge of the hole is electron transparent but it is less than 1 micron in width. In this sample and others containing porosity, the angle at which the alloy material exists away from the pore is steep leading to a sample thickness that is not electron transparent. An ideal TEM sample would consist of an acute-angled wedge of material away from the perforation, allowing a large area of visibility when investigated with the electron beam of a TEM or STEM.

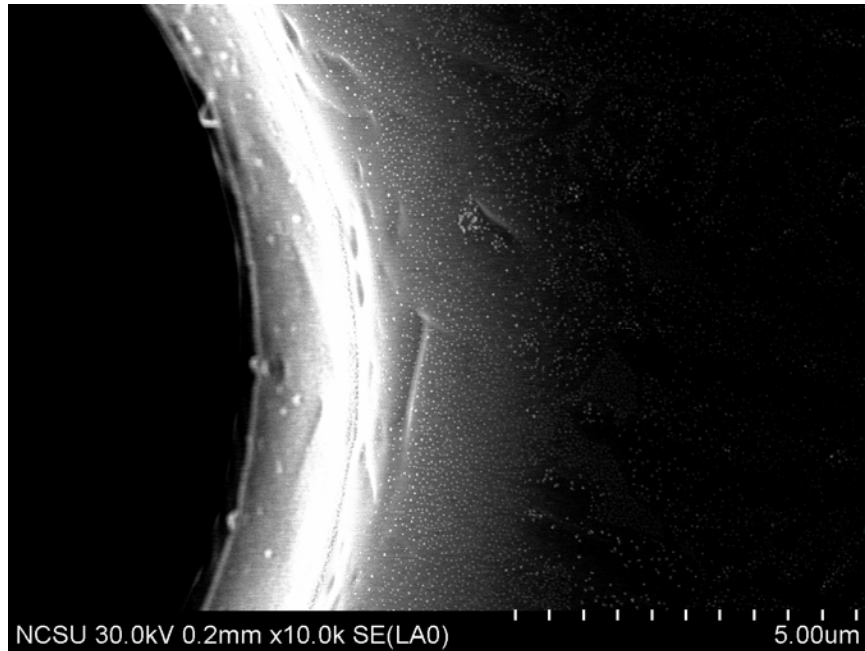


Figure 4.72. Secondary electron SEM image of perforation edge of an electropolished XY Cross Section Ti-6Al-4V 3mm disc TEM sample shown in Figure 4.71.

Figure 4.73 is an SEM micrograph of an a Horizontal Cylinder Face TEM sample in progress that has been mechanically polished on one side using the same sequence of SiC paper from 180 through 1200 grit with a final polish of 1.0 μm aluminum oxide slurry. The thickness of this sample is at least 0.3 mm. This sample is still mounted on the stainless steel stub that is used in the Gatan 623 Disc Grinder used for mechanical thinning and polishing. Silver paint has been applied to the edge of the sample to promote electrical conductivity of the electron beam of the SEM. Porosity is visible on the surface of this sample as indicated by the arrows in Figure 4.73 below.

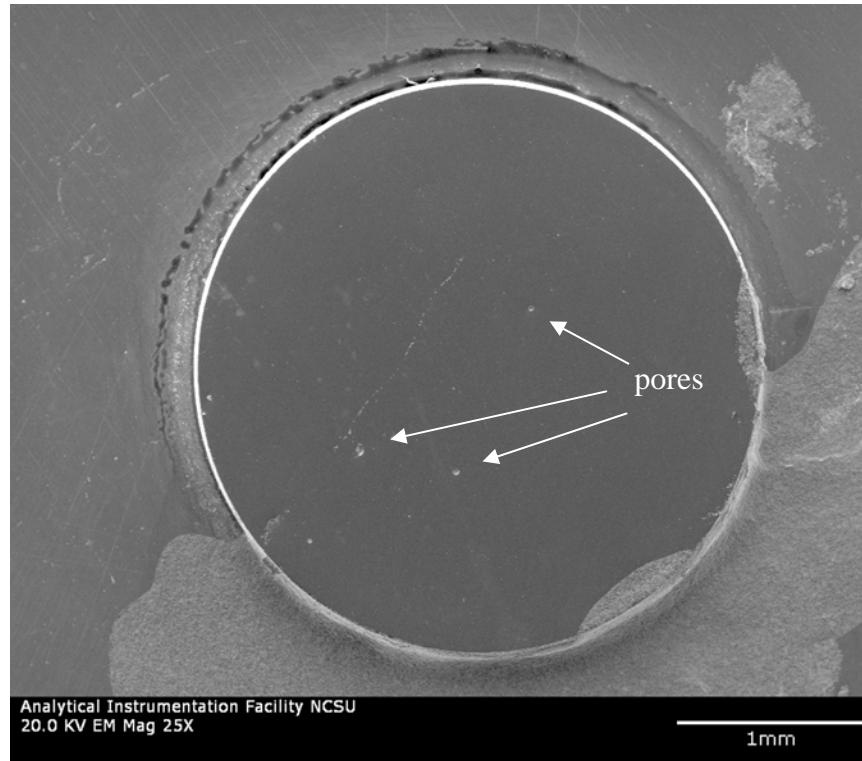


Figure 4.73. SEM micrograph of HC face Ti-6Al-4V TEM sample in progress.

Figure 4.74 is a higher magnification SEM micrograph of the pores mentioned in the Horizontal Cylinder Face sample featured in Figure 4.73. Aluminum oxide polishing media has collected in the pores and also along the interface of the layers of material that have been deposited during the Arcam EBM process, which are oriented diagonally in this image. The size of the larger pore in the upper left area of this image is 66 μm long and 32 μm across. The pore in the lower right corner is approximately 35 μm in diameter. These surface imperfections become areas that are attacked by the electropolishing action, leading to undesirable through-wall perforations.

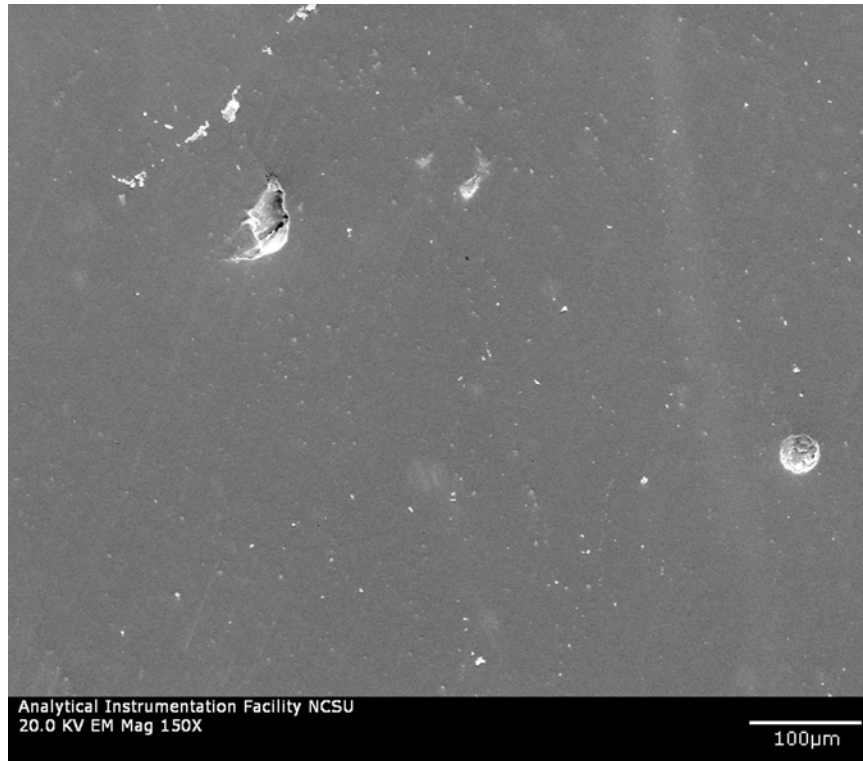


Figure 4.74. SEM micrograph of the surface of an HC face Ti-6Al-4V TEM sample exhibiting porosity.

Premature through-wall perforation occurs when twin-jet electropolishing Ti-6Al-4V samples from the Arcam EBM process when porosity is present within the sample. The initial hole expands rapidly and within seconds the material in the desired area to be examined will be etched away, leaving steep-angled material that is too thick to be imaged with TEM or STEM instead of a thin ledge of electron transparent material.

4.6.2. Solution to the Porosity Problem

The porosity problem preventing successful production of TEM samples was alleviated by adding an additional step to the electropolishing routine. The samples were removed from the electropolisher before perforation begins or immediately thereafter. After the samples are rinsed in methanol and dried, automotive acrylic lacquer paint was applied to the holes and any other locations that are being removed at a higher rate than the majority of the alloy exposed to the electrolytic solution using a single hair taken from an artist's paint brush under a stereo optical microscope. Reducing the lacquer up to 100% with an appropriate solvent such as lacquer thinner was necessary to allow the paint to flow into the desired areas and prevent the brush hair from adhering to the 3 mm disk. The lacquer paint acted as a mask and was not be affected by the electrolytic solution of methanol, butanol, and perchloric acid. After the paint is allowed to dry for several hours, the samples were returned to the electropolisher to properly complete the thinning process which produced large areas of electron transparency. The samples were thoroughly soaked in lacquer thinner to remove the lacquer and dried prior to examining with TEM.

4.6.3. Focused Ion Beam

Problems associated with producing samples by electropolishing due to excessive porosity led to the pursuit of other means to produce electron transparent samples.

Focused ion beam (FIB) was successfully used to prepare a sample from the XZ Face sample. Figures 4.75 and 4.77 show the XZ Face FIB sample which is affixed in the v-notch of a copper sample mount.

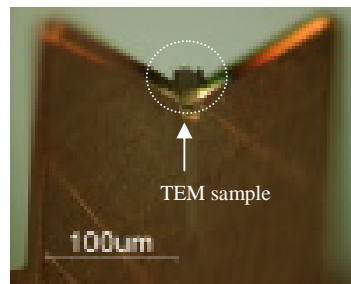


Figure 4.75 Low magnification optical image of XZ face FIB sample as affixed to TEM sample mount.

Figure 4.76 shows the XZ Face surface from which material is milled away by a focused gallium ion beam in order to isolate a region that will be further thinned to electron transparency by the ion beam. Surface finish of the bulk material is that of 1200 grit SiC paper prior to FIB. The center region between the two trenches is further thinned to below 100 nm, lifted out and attached to the TEM sample mount as shown in Figures 4.75 and 4.78. The sample is tilted, allowing a view of the sample prior to final thinning. The extra material between the trenches is a platinum / carbon alloy that has been deposited onto the T-6Al-4V

material to protect the material of interest from gallium ion beam damage during the FIB procedure.

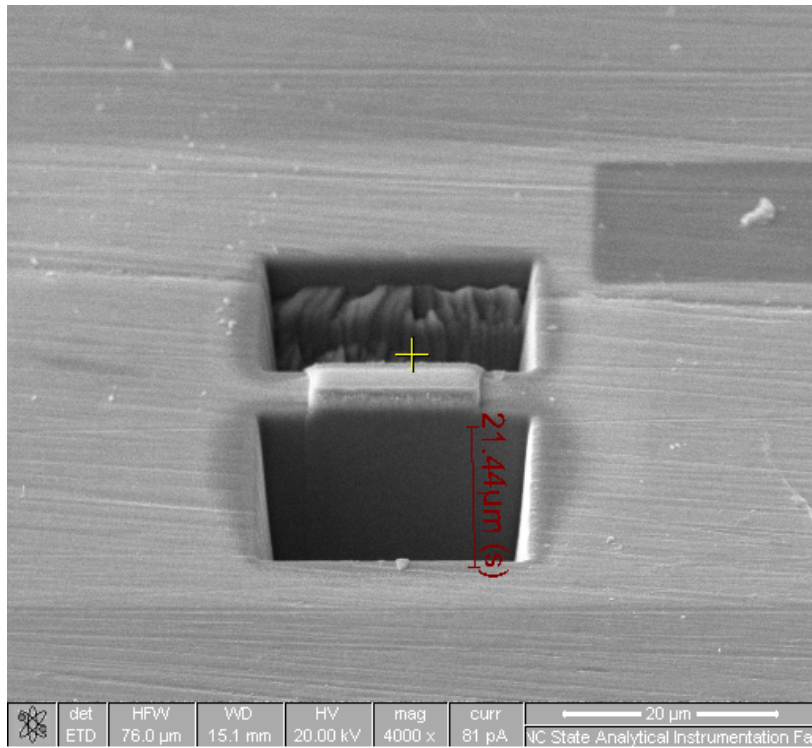


Figure 4.76 Image of XZ Face FIB sample (in progress).

Figure 4.77 shows the area of the XZ Face FIB sample after final thinning, just prior to being transferred to the TEM sample mount that will allow it to be imaged in a TEM. The incident electron beam of the FIB is normal to the XZ Face surface which provides an edge view of the sample.

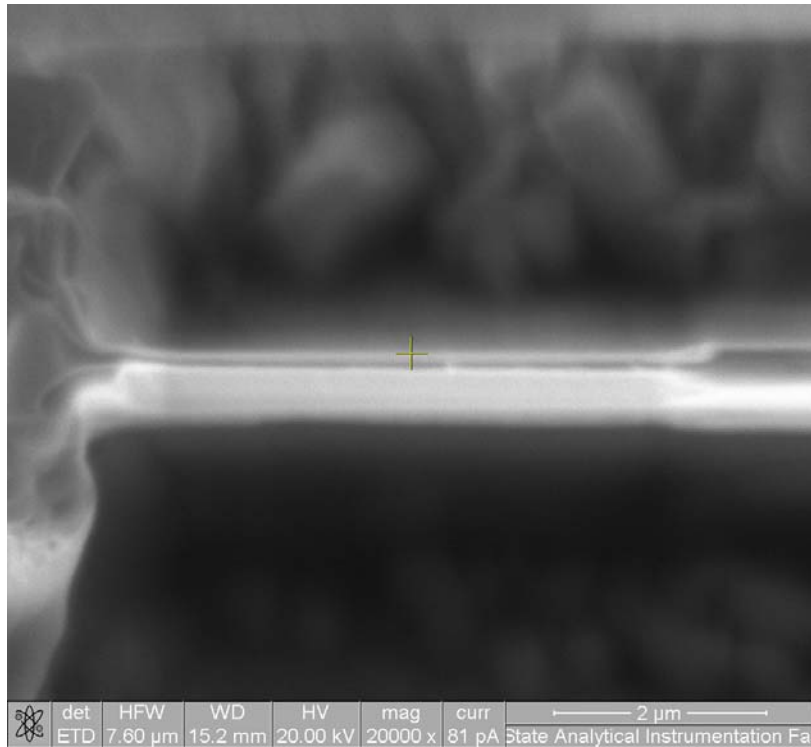


Figure 4.77. Image of XZ Face FIB sample after final thinning.

Effective area that is suitable for TEM and/or STEM imaging is the 5 μm by 9 μm rectangular area, located on the left side of the sample between the thicker posts, just left of the 10.86 μm length marker. The material above the rectangular area and the 10.86 μm marker is the Pt/C alloy protective layer.

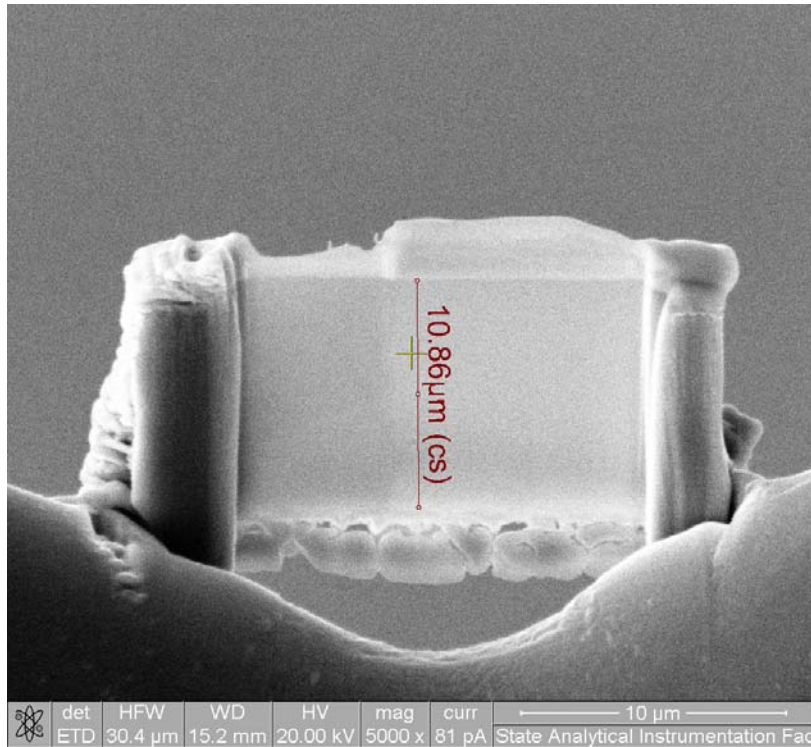


Figure 4.78. XZ face FIB sample as affixed to TEM sample mount. Bottom image shows sample after final thinning of left side which is approximately 50 nm in thickness.

The 5 by 9 μm portion of FIB sample that is observable in a TEM is extremely small compared to the amount of observable volume available in an electropolished sample which can be hundreds of square microns and therefore may not be representative of the bulk material. FIB samples are thicker than electropolished samples which is undesirable for imaging. The advantage of the FIB sample is the ability to revisit an area of interest when using multiple characterization techniques that may not be available on just one instrument. Another advantage includes the ability to retain orientation with respect to the bulk material.

5. CONCLUSIONS

Specimens produced by the Arcam S12 EBM and Arcam A2 EBM machines have a Widmanstätten microstructure consisting of fine acicular alpha laths with beta phase present between the alpha laths. From TEM data, discontinuous beta phase particles were found that may contain more complex microstructural features such as precipitates along the alpha/beta interfaces. The amount of retained beta phase was higher in the A2 produced sample compared to the S12 produced samples, but not significantly higher. A 10 % difference in the retained beta between XY and XZ sample from the Arcam S12 EBM machine was found.

In addition to possessing similar microstructures, grain sizes of prior beta grains of sample produced by the Arcam S12 and A2 EBM machines are not significantly different. Grain sizes are much larger than the grains that were found in the forged turbine blade. Columnar grain growth and alpha phase at prior beta grain boundaries microstructural features exist within Arcam S12 and A2 produced Ti-6Al-4V components which are undesirable microstructural features with regards to component acceptance via AMS 4999 standard.

Due to the limited number of samples (only 3 total) and without consideration of any further improvements on the structural integrity of components, the conclusions made within this study may not apply to components currently being produced. From the limited sample set used in this study, defects in the form of porosity are in fact an intrinsic microstructural feature in these early Arcam-produced components with the parameters used for their manufacture.

Porosity occurred at any given depth within these components. The size and shape of the defects found, most notable the long flat cavities that are hundreds of microns in length may fail prematurely from applied stress such as cyclic loading. The XZ sample seemed less prone to porosity from incomplete melting due to its geometry and cross sectional profile as it is grown, although the mechanical property data from Bass [6] does not suggest any advantage exists. The lack of porosity being reported as a major finding in other studies [1, 16] may be attributed to the fact that samples were also grown with similar geometry (i.e. tensile coupons with tensile axes parallel to the growth direction) in the XZ configuration. Porosity is influenced by the alloy powder feedstock. Agglomeration of PREP powder particles can contribute to undesirable packing of the particle powder bed prior to application of the electron beam. Hollow spheres have been observed which can potentially lead to porosity from entrapped cavities if incomplete melting occurs. Based on the finding of this study, the Arcam S12 and A2 EBM machines will not likely produce components that are free from imperfections and porosity detrimental to usage of the product as mandated by Section 3.7 AMS 4999 regarding quality unless other EBM operating parameters can be established experimentally or through successful HIP treatment.

Micrographs of the exterior morphology and complementary views of mounted samples near the edge of the solid objects perpendicular to the growth direction indicate that the build layers are larger than the 100 μm individual layer height reported by those responsible for component fabrication. Step increment (z-height of build table in the negative direction) may require calibration.

Based on the simple geometries used for this study, the Arcam S12 and A2 EBM machines sufficiently meet the 760 μm machining tolerance requirements for near-net shape performs as specified in AMS 4999.

FIB has proven to be a successful means of producing samples for examination by TEM and STEM in a porous alloy without causing excessive ion damage. Although FIB lift-out samples can only produce an extremely small area of view that may not be representative of the bulk material it has the advantage of lending itself to observing the same features of interest in various microscopes.

Successful TEM sample preparation of porous metals via electropolishing can be achieved by implementing a lacquer finish masking technique in a two-stage electropolishing process.

6. FUTURE WORK

6.1. Electron Backscatter Diffraction of Growth Plane Normal

Preferred crystallographic grain growth orientation can be established using electron backscatter diffraction (EBSD) data in the form of Kossel / Kikuchi patterns collected on an SEM outfitted with the appropriate detector [27]. Sample preparation for EBSD technique requires surface roughness be less than 50 nm and can be achieved through procedures described in Experimental Procedure, excluding the etching step and is improved with low-energy vacuum ion-sputtering or electropolishing [27]. The JEOL EM-09100IS Ion Slicer may also lend itself well to this application.

6.2. Hot Isostatic Pressing (HIP) of Arcam Components

AMS 4999, the standard which governs component acceptability criteria for laser and electron beam fabricated components for use in military aircraft reconstruction, states that such components must be hot isostatically pressed (HIP) per a prescribed schedule of time, temperature and pressure. Evaluation of the microstructure of Arcam-produced Ti-6Al-4V components should be repeated with controlled EBM parameters, such as fixed power level and scan speed, and HIP post processing. TEM sample preparation problems due to porosity are expected to decrease following HIP treatment; 50 ksi at 1550°F for 4 hours as prescribed in AMS 4999.

6.3. Temperature Measurement of Build Plane

Temperature measurement of the build plane in the Arcam S12 and A2 machines are not currently being monitored. Such temperature readings have been established for titanium and titanium alloys by Kusamichi, et al. [28] by an optical method utilizing a two-color pyrometer where two wavelengths of 500 and 580 nm and a visible light spectrometer from 400 to 800 nm. It was found that the measurements vary with EBM chamber pressure and the melt pool temperature can be calculated by using the visible light spectrum as a baseline. This may be used in conjunction with metallographic studies at various depths of an Arcam-produced sample to conclude upon a cooling rate [29].

6.4. Initial Densification of Alloy Powder bed

Since the pre-alloyed powder used for electron beam melting is simply spread and not packed in any way, increasing the packing efficiency of the loose powder bed through optimum particle size and distribution and perhaps the introduction of a vibration mechanism prior to melting with the electron beam may improve the initial as-built component densification.

6.5. Resistivity of Alloy Powder Bed

The resistivity of the loose powder bed may be established as a function of accelerating potential in an SEM using an ammeter as used to image or measure specimen current. Information from a measurement of electrical conductivity may be helpful in optimizing fabrication of objects from loose powder beds as well as predicting and

preventing electron charge build up of the powder bed from the incident electron beam used for melting.

6.6. Investigation of Microstructure at α/β Interface

The existence of a face-centered cubic (FCC) crystal structure of the α/β interfacial phase has been reported by Servant et al. [26]. Further investigation into the possibility of an FCC phase present at the α/β interface layer in Arcam-produced components may support the high ductility found in Arcam-produced components. Mechanical properties of the individual constituents could be measured by nanoindentation. Nanodiffraction techniques in TEM could be used to positively identify crystal structure of precipitates along the α/β interface.

6.7. Implementation of Digital Image Processing for Volume Fraction of Phases

Digital image process programs such as FOVEA Pro and Image J could be used to calculate phase volume fraction data [24], but an automatic thresholding procedure would be established in order to do so in an accurate and reproducible manner. Accuracy could be increased by removing the human component of visual analysis in addition to decreasing analysis time. Spherical PREP powder particle diameters could be measured more systematically with the use of erosion techniques [30] if feedstock size and distribution is to be correlated with microstructure and mechanical properties in further studies.

REFERENCES

1. Dinda, G.P., Song, L., Mazumder, J., "Fabrication of Ti-6Al-4V Scaffolds by Direct Metal Deposition", *Metallurgical and Materials Transactions A*, Vol 39A, 2914-2922, December (2008)
2. <http://www.arcam.com/Downloads/PDF/machinedata.pdf>
3. Thundal, S., "Rapid Manufacturing of Orthopaedic Implants", *Advanced Materials & Processes*, Vol 166, 60-62, October (2008).
4. Srivastava D., Chang, I.T.H., Loretto, M.H., "The Optimisation of Processing Parameters and Characterisation of Microstructure of Direct Laser fabricated TiAl Alloy Components", *Materials and Design* 21 425-433 (2000).
5. Mitchell, A., "The Electron Beam Melting and Refining of Titanium Alloys", *Materials Science and Engineering*, A263, 217-223, (1999).
6. Bass, B.S., Validating the Arcam EBM Process as an Alternative Fabrication Method for Titanium-6Al-4V Alloys. Thesis, North Carolina State University, 2007.
7. Baucio, M., ASM Metals Reference Book, 3rd edition, ASM International, OH, (1993).
8. <http://www.synergieering.com/images/EBM/diagram.jpg>
9. Goldstein, J., Newbury, D., Joy, D., Lyman, C., Echlin, P., Lifshin, E., Sawyer, L., Michael, J., Scanning Electron Microscopy and X-Ray Analysis, 3rd edition, Kluwer Academic/Plenum Publishers, NY, 33, 61-73 (2003).
10. Yule, A.J., Dunkley, J.J., Atomization of Melts For Powder Production and Spray Deposition, Clarendon Press, 207-208 Oxford (1994).
11. Lawley, A., Atomization: The Production of Metal Powders, Metal Powder Industries Federation, New Jersey, 30-33 (1992)
12. <http://www.gel.usherbrooke.ca/casino/>
13. Donachie, M.J., Titanium A Technical Guide, 2nd edition, ASM International, OH, (2000).
14. Joshi, V.A., Titanium Alloys An Atlas of Structures and Fracture Features, CRC Press, Taylor and Francis Group, (2006).

15. Ervin, J. K., Post Heat Treatment Effects of Ti-6Al-4V Produced via Solid Freeform Electron Beam Melting. Thesis, North Carolina State University, 2008.
16. Murr, L.E., Esquivel, E.V., Quinones, S.A., Gaytan, S.M., Lopez, M.I., Martinez, E.Y., Medina, F., Hernandez, D.H., Martinez, E., Martinez, J.L., Stafford, S.W., Brown, D.K., Hoppe, T., Meyers, W., Lindhe, U., Wicker, R.B., "Microstructures and Mechanical Properties of Electron Beam-Rapid Manufactured Ti-6Al-4V Biomedical Prototypes Compared to Wrought Ti-6Al-4V", *Materials Characterization*, vol 60, 96-105, (2009)
17. Possin, G.E., Parks, H.G., Chiang, S.W., Convection in Pulsed Laser Formed Melts, Laser and Electron-Beam Solid Interactions and Materials Processing, MRS Symposia Proceedings, Vol 1., Elsevier North Holland, Inc., Gibbs, Hess and Sigmon, eds., 73-80, (1981).
18. Kestel, B.J., "Polishing Methods for Metallic and Ceramic Transmission Electron Microscopy Specimens", Materials Science Division, Argonne National Laboratory (1986).
19. Williams, D.B., Carter, C.B., Transmission Electron Microscopy: A Materials Science Textbook, pp. 157-170. (2003)
20. Blackburn, M.J., Williams, J.C., "The Preparation of Thin Foils of Titanium Alloys", *Transactions of the Society of Petroleum Engineers of the American Institute of Mining, Metallurgical, and Petroleum Engineers, Inc.*, vol 239, 287-288 (1967).
21. Principe, E. L. "STEMs vs. TEMs", *Microscopy Today*, Vol. 9 #7, 34-35 September (2001).
22. Tracy, B., Alberi, K, Tabrez, S., "Adopting Low-Voltage STEM and Automated Sample Prep to Perform IC Failure Analysis", *Micro*, Vol 22 # 6, 87-94, July (2004).
23. Hitachi High Technologies America, Inc. Technical Notes
"Electron Microscopy of Compound Materials Using Low Voltage STEM Mode of the S-5200 Ultra-High Resolution SEM"
http://www.hitachi-hta.com/media/Hitachi_5200_STEM_mats.pdf
24. Tiley, J., Searles, T., Lee, E., Kar, S., Banarjee, R., Russ, J.C., Fraser, H.L., "Quantification of Microstructural Features in a/b Titanium Alloys", *Materials Science and Engineering A*, 372, 191-198 (2004).
25. Locci, I.E., Welsch, G.E., "TEM of Titanium Alloys Compacted at Very High Pressure and Low Temperature", Titanium Rapid Solidification Technology, The Metallurgical

Society, Inc. Froes, F.H., Eylon, D., eds., 291-295 (1994).

26. Servant, C., Quesne, C., Baudin, T., Penelle, R., "Contribution to the Analysis of the α/β Interface in Some Titanium Alloys", *J. Mater. Res.*, Vol. 6, No. 5, 987-998 May (1991).
27. Wynick, G.L., Boehlert, C.J., "Electron Backscattered Diffraction Characterization Technique for Analysis of a Ti_2AlNb Intermetallic Alloy", *Journal of Microscopy*, Vol. 219, Pt. 3, 115-121, September (2005).
28. Kusamichi, T., Kanayama, H., Onoye, T., "Temperature Measurement of Molten Metal Surface in Electron Beam Melting of Titanium Alloys", *ISIJ International*, vol. 32, No. 5, 593-599 (1992).
29. Ahmed, T., Rack, H.J., "Phase Transformations During Cooling in $\alpha + \beta$ Titanium Alloys", *Materials Science and Engineering A*, 243, 206-211 (1998).
30. Russ, J.C., The Image Processing Handbook, 5th edition, CRC Press Taylor & Francis Group, FL, (2007).